Cancer Gene Therapy
https://doi.org/10.1038/s41417-020-0196-5

ARTICLE

Anti-SSTR2 antibody-drug conjugate for neuroendocrine tumor therapy

Yingnan Si[1] · Seulhee Kim[1] · Jianfa Ou[1] · Yun Lu[1] · Patrick Ernst[1] · Kai Chen[1] · Jason Whitt[2] · Angela M. Carter[2] · James M. Markert[3,4] · James A. Bibb[2,4] · Herbert Chen[2,4] · Lufang Zhou[5] · Renata Jaskula-Sztul[2,4] · Xiaoguang "Margaret" Liu[1,4]

Received: 1 April 2020 / Revised: 18 June 2020 / Accepted: 24 June 2020

Abstract

Neuroendocrine (NE) tumors include a diverse spectrum of hormone-secreting neoplasms that arise from the endocrine and nervous systems. Current chemo- and radio-therapies have marginal curative benefits. The goal of this study was to develop an innovative antibody-drug conjugate (ADC) to effectively treat NE tumors (NETs). First, we confirmed that somatostatin receptor 2 (SSTR2) is an ideal cancer cell surface target by analyzing 38 patient-derived NET tissues, 33 normal organs, and three NET cell lines. Then, we developed a new monoclonal antibody (mAb, IgG1, and kappa) to target two extracellular domains of SSTR2, which showed strong and specific surface binding to NETs. The ADC was constructed by conjugating the anti-SSTR2 mAb and antimitotic monomethyl auristatin E. In vitro evaluations indicated that the ADC can effectively bind, internalize, release payload, and kill NET cells. Finally, the ADC was evaluated in vivo using a NET xenograft mouse model to assess cancer-specific targeting, tolerated dosage, pharmacokinetics, and antitumor efficacy. The anti-SSTR2 ADC exclusively targeted and killed NET cells with minimal toxicity and high stability in vivo. This study demonstrates that the anti-SSTR2 ADC has a high-therapeutic potential for NET therapy.

Introduction

Neuroendocrine (NE) tumors, such as carcinoids, pancreatic islet cell tumors, and medullary thyroid cancer (MTC), arise from cells within the neuroendocrine system that often harbor inherited or sporadic genetic mutations[1,2]. The prevalence of NE tumor (NET) patients in the United States is in excess of 100,000, with at least 16,000 new diagnoses each year and an estimate of 200,000-plus undiagnosed cases[3,4]. Patients living with untreatable NET liver metastases have a 5-year survival rate of 13–54%[5]. The fact that 40–95% of patients with NETs are metastatic at the time of initial diagnosis makes complete surgical resections nearly impossible[3,6–10]. Chemotherapies utilized for NET (e.g., the mTOR inhibitor "everolimus" and the multikinase inhibitor "sunitinib") have shown limited efficacy and can cause systemic toxicities[11–18]. Somatostatin receptor (SSTR)-targeting analogs (e.g., octreotide and lanreotide) or FDA-approved peptide receptor radionuclide therapy (Lutathera®) for gastroenteropancreatic NET treatment can extend patient' survival but have relatively poor impact on rapidly proliferating tumors[19,20]. Thus, it is imperative to develop new treatment strategies for this disease.

Supplementary information The online version of this article (https://doi.org/10.1038/s41417-020-0196-5) contains supplementary material, which is available to authorized users.

✉ Renata Jaskula-Sztul
rjsztul@uabmc.edu

✉ Xiaoguang "Margaret" Liu
mliu@uab.edu

[1] Department of Biomedical Engineering, University of Alabama at Birmingham (UAB), 1825 University Blvd, Birmingham, AL 35294, USA

[2] Department of Surgery, UAB, 1808 7th Avenue South, Birmingham, AL 35294, USA

[3] Department of Neurosurgery, UAB, 510 20th Street South, Birmingham, AL 35294, USA

[4] O'Neal Comprehensive Cancer Center, UAB, 1824 6th Avenue South, Birmingham, AL 35233, USA

[5] Department of Medicine, UAB, 703 19th Street South, Birmingham, AL 35294, USA

Published online: 20 July 2020

Five SSTR subtypes (SSTR1-5) belonging to the G-protein coupled receptor (GPCR) family are expressed in tumor or normal tissues[21]. NET patients overexpress SSTR2 and SSTR3 at a high density[22–25]. The membrane expression of SSTR2 in NET cells is ~20-fold higher than that of normal cells[22–24]. Moreover, our immunohistochemistry (IHC) analysis performed on a patient tissue microarray (TMA) demonstrated that over 70% of NET patients express SSTR2. Therefore, SSTR2 is a potential target for the development of a new therapeutic approach to treat NETs.

Targeted therapies, such as monoclonal antibodies (mAbs) and antibody-drug conjugates (ADCs) have been applied to treat cancers with minimal side effects on normal cells[26–29]. ADCs engender many of the advantages of mAbs including cancer-specific targeting to lower toxicity in normal tissues, low immunogenicity, long plasma half-life and high stability, with the high cytotoxicity of small molecule chemotherapeutics[30]. After receptor binding, ADC is internalized via receptor-mediated endocytosis. The cytotoxic drug is then released into the cytoplasm of cancer cells via either lysosomal degradation or linker cleavage[31,32]. As precedents, several antibodies carrying payloads, such as brentuximab vedotin (anti-CD30-MMAE), trastuzumab emtansine (anti-HER2-DM1), ^{131}I-Tositumomab (I-131 labelled anti-CD20 mAb), ^{90}Y-Ibritumomab tiuxetan (^{90}Y labelled anti-CD20 mAb), and traztuzumab deruxtecan (anti-HER2 mAb-topoisomerase I inhibitor), have been developed to treat relapsed Hodgkin lymphoma, systemic anaplastic large cell lymphoma, relapsed, chemotherapy refractory or advanced HER2-positive breast cancer, non-hodgkin's lymphoma (NHL), or NHL[33]. To our knowledge, neither mAb nor ADC has yet been developed for NET treatment. In addition to ADC, the SSTR2-targeted PEN-221 comprised a SSTR2 agonist [Tyr3, Cys8]octreotate amide linked to mertansine has been developed to treat small cell lung cancer[34]. The AN-238, a cytotoxic analogue of SST conjugated with peptide RC-121 and 2-pyrrolinodoxorubicin (2-pyrrolino-DOX), and two camptothecins (CPT)-potent somatostatin analog (SSA) conjugates, JF-10-71 and JF-10-81, have also been developed to treat choroidal neovascularization and lung cancer[34–36].

The objective of this study was to develop an innovative targeted therapy to treat SSTR2-overexpressing NETs. A surface receptor analysis of multiple patient tissues and normal organ tissues showed that SSTR2 is highly expressed in most of NET patients. A new anti-SSTR2 mAb was developed to efficiently target NET and deliver an FDA-approved potent cytotoxic payload, Monomethyl auristatin E (MMAE), which can effectively block microtubulin polymerization and inhibit NET cell growth. The specific targeting, tolerated dosage, pharmacokinetics, and antitumor efficacy of the anti-SSTR2 ADC were investigated using a NET xenograft mouse model. Our results demonstrate that the developed ADC was capable of specifically targeting and effectively reducing tumor growth, indicating promise for further development as a novel therapeutic for these tumors.

Materials and methods

The animal studies conform to the Guide for the Care and Use of Laboratory Animals published by the National Institutes of Health (NIH Publication No. 85-23) and have been approved by the Institutional Biosafety Committee at the University of Alabama at Birmingham under the animal project number of IACUC-21929. The investigators were not blinded to the group allocating during the experiment and assessing the outcome.

NET patient tissue microarray

The TMA was prepared by Research Pathology Core to analyze the SSTR2 surface expression in NET. The patient tissues were obtained from the University Surgical Oncology Tumor Bank through an Institutional Review Board (IRB) approved protocol. The NET microarray consisted of 38 patient tissue cores, which contained 1 high-grade (G3) and 37 low-grade (G1) and intermediate-grade (G2) samples (2A to 9D), and five normal tissue cores of liver, spleen, placenta, prostate, and tonsil (negative controls, 1A-1E). The TMA slides of 33 normal human organs were purchased from US Biomax (Rockville, MD) to confirm the binding specificity of our anti-SSTR2 mAb using IHC staining with NET tissues as positive controls. The normal organs that we tested included cerebrum, cerebellum, peripheral nerve, adrenal gland, thyroid gland, spleen, thymus, bone marrow, lymph node, tonsil, pancreas, liver, esophagus, stomach, small intestine, colon, lung, salivary, pharynx, kidney, bladder, testis, prostate, penis, ovary, uterine tube, breast, endometrium, cervix, cardiac muscle, skeletal muscle, mesothelium, and skin.

Cell lines and media

Multiple human NET cell lines, including pancreatic NET BON-1 (kindly provided by Dr. Mark Hellmich from University of Texas, Galveston, TX) and QGP-1 (ACCEGEN Biotechnology, Fairfield, NJ), BON-Luc carrying a firefly luciferase reporter gene (generated in our lab by overexpressing FLuc in BON-1 cells), were used for in vitro or in vivo studies. BON-1 and OGP-1 cells were maintained in DMEM/F12 medium supplemented with 10% fetal bovine serum (FBS) in T25 or T75 flasks. The non-neoplastic SSTR2-negative control cell lines, including pulmonary fibroblast WI-38 (ATCC, Manassas, VA) and foreskin fibroblast 917 (ATCC), were maintained in DMEM with

10% FBS, 1% non-essential amino acids, and 1% sodium pyruvate. Adherent mAb producing hybridoma cells were maintained in DMEM with 10% FBS in T flasks, while the adapted suspensive hybridoma was cultivated in Hybridoma-SFM with 4 mM L-glutamine and 1% anti-clumping agent (v/v) in shaker flasks with agitation of 130 rpm. All seed cultures were incubated at 37 °C and 5% CO_2 in a humidified incubator (Caron, Marietta, OH). The cell growth, i.e., viable cell density (VCD) and viability, was measured using a Countess II automated cell counter or trypan blue (Fisher Scientific, Waltham, MA). All basal media, supplements, and reagents used in this study were purchased from Fisher Scientific or Life Technologies (Part of Fisher) unless otherwise specified.

Anti-SSTR2 mAb development

Both human SSTR2 (UniProtKB P30874) and mouse SSTR2 (UniProtKB P30875) are integral membrane glycoproteins with the same topology, including four extracellular topological domains, seven helical transmembrane, and four cytoplasmic topological domains. Protein BLAST analysis showed that their four extracellular domains had similarity of 81%, 100%, 100%, and 90%, respectively. We developed an SSTR2 mAb to target the 1st extracellular domain (cQTEPYYDLTSNA, aa 33–44) and the 2nd extracellular domain (cALVHWPFGKAICRVV, aa 104–118) using hybridoma technology (PCT patent, US2019/0055145). The immune splenocytes with the best anti-SSTR2 antibody expression were fused with myeloma cells (Sp2/0) to obtain 100 hybridoma subclones. The top 4 clones were screened using peptides (the 1st and the 2nd extracellular domains)-based ELISA and were adapted to serum-free suspension cultures to produce mAbs[37]. The tumor cell surface binding of these four mAbs was evaluated using flow cytometry and confocal microscopy imaging. These methods were used to define the lead clone which had strong and specific binding to NET (BON-1) cells but low binding to noncancerous control cells. The isotype of the lead clone was determined using a mouse antibody isotyping kit (Sigma, St. Louis, MO).

Anti-SSTR2 mAb production and purification

The mAb production was performed in a 5-L stirred-tank bioreactor controlled at Temp 37 °C, pH 7.0, DO 50% and agitation 70 rpm. The bioreactor was seeded with VCD of $0.3–0.5 \times 10^6$ cells/mL in Hybridoma-SFM with 6 g/L glucose, 6 mM L-glutamine, 3.5 g/L Cell Boost #6, and 1% anti-clumping agent. The production cultures were sampled daily to monitor cell growth (i.e., VCD, viability, double time, and growth rate) using cell counter, glucose concentration using glucose analyser, and mAb production using NGC system (Bio-Rad, Hercules, CA). The anti-SSTR2 mAb was purified using our two-step antibody purification protocol by the NGC system (Bio-Rad, Hercules, CA) equipped with Protein A and ion exchange columns[38,39].

ADC construction

In this study, ADC was constructed following our published cysteine-based conjugation procedure[38,39]. Briefly, the rebridging linker was synthesized by reacting 3.91 mmol 6-aminohexanoic acid with 3.91 mmol 3,4-dibromofuran-2,5-dione in 20 mL acetic acid at room temperature (RT) for 10 min and purified with silica gel. Then the linker-MMAE payload was conjugated by mixing 33.85 µmol synthesized rebridging linker, 13.55 µmol N,N'-diisopropylcarbodiimide, 13.55 µmol N,N-diisopropylethylamine, and 13.55 µmol MMAE in 0.25 mL dichloromethane for 17 h and purified with HPLC. The 5 mg/mL anti-SSTR2 mAb was reduced with 1 mM dithiothreitol in 50 mM borate buffer at pH 8.0 at 37 °C for 1 h and purified with buffer exchange. Finally the ADC was conjugated by mixing the linker-MMAE payloads with the reduced mAb with payload:mAb molar ratio of 4.4 and incubated at 4 °C for 1 h. The generated ADC was purified with PD SpinTrap™ G25 column (GE Healthcare, Chicago, IL) or high-performance liquid chromatography (Waters, Milford, MA). The average drug-antibody ratio (DAR) was calculated as $\text{Ratio} = (\varepsilon_{Ab}{}^{248} - R\varepsilon_{Ab}{}^{280})/(R\varepsilon_{D}{}^{280} - \varepsilon_{D}{}^{248})$, where $R = A_{248}/A_{280} = \text{Absorbance ratio}$[38].

In vitro anticancer cytotoxicity (IC_{50})

BON cells were utilized to evaluate the anti-NET cytotoxicity of the anti-SSTR2 ADC and MMAE (control) in 96-well plate following our published protocol[38]. Briefly, the BON cells were seeded with viable cell density of 50,000 cells/mL in 75 µL of DMEM/F12 medium complete medium, and incubated at 37 °C for 24 h. Then the anticancer cytotoxicity assay was initiated by adding 75 µL of medium containing ADCs and free drug with final concentrations of 0.5, 1, 2, 10, and 25 nM with triplication. After 72 h incubation, the toxicity was measured through CellTiter-Glo Luminescent Cell Viability Assay (Promega, Madison, MI). The luminescent signal was proportional to the viable cell number and used to calculate the relative viability in all treatments. The IC_{50} value was calculated using ED50V10 Excel add-in.

SDS-PAGE and western blotting

The Mem-PER plus membrane protein extraction kit was used to extract membrane proteins for surface receptor evaluation. The protein concentration was determined by

the Pierce BCA assay. Non-reducing SDS-PAGE was run using NuPAGE™ 4–12% Bis-Tris protein gels. The primary rabbit anti-mouse antibody and HRP-conjugated secondary anti-rabbit antibody were purchased from Abcam (Cambridge, UK). The blotted membrane was treated with Luminata Forte Western HRP substrate (Millipore, Boston, MA), and imaged with MyECL imager with ImageJ software.

Flow cytometry

Flow cytometry was performed to quantify surface receptor binding of SSTR2 mAb using a BD LSRII flow cytometer (BD Biosciences, San Jose, CA). The mAb was labelled with an Alexa Fluor™ 647 labelling kit to generate AF647-mAb. The NET cell lines (BON and QGP-1) and negative control fibroblast cell line (917) were tested. Detailed methods are described elsewhere[38,39] Briefly 1×10^6 cells were mixed with 1 µg AF647-mAb in 100 µL PBS and incubated at room temperature for 30 min in dark. The labelled cells were washed with PBS for three times and resuspended in 500 µL buffer for flow cytometry analysis. The commercial anti-SSTR2 mAb (RD Systems, Minneapolis, MN, catalog# MAB4224) was used as control.

SSTR2 binding affinity and specificity analysis

The SSTR2 mAb-receptor binding affinity was measured following the previously reported procedure[40]. Specifically, 120 ng of somatostatin receptor 2 was coated on 96-well plates and incubated at 4 °C overnight. Plates were washed using PBS plus 0.05% Tween 20for 3 times and blocked with protein-free blocking buffer at 37 °C for 1 h. Our anti-SSTR2 mAb was added following concentration gradient of 0, 5, 10, 50, 100, 500, 1000, 10,000, 50,000, and 100,000 pM, incubated at 37 °C for 1 h, and plates were washed for 5 times. Goat anti-mouse IgG HRP was added to each well at a concentration of 50 ng/mL, followed by 30-min incubation at 37 °C and three times of washing. Then 100 µL of TMB substrate solution was added to each well and incubated at RT for 30 mins, and 100 µL of 1 M H_2SO_4 was added to stop color development. The absorbance was read using BioTek plate reader at a wavelength of 450 nm.

Confocal imaging

Confocal microscopy was used to observe the dynamic surface binding and internalization of mAb and ADC in NET cells following our established protocol[38,39]. Specifically, BacMam GFP Transduction Control was used to stain the cytoplasm and nucleus, and the AF647-mAb or AF647-ADC was used to target cells. The stained cells were observed using an Olympus 1X-81 confocal microscope with a laser scanning head (Olympus IX81, Center Valley, PA). The MitoSox images were recorded and analyzed offline via ImageJ software.

Tolerated dose (TD) and pharmacokinetics (PK) study

To investigate the tolerated dose and metabolic rate of ADC, five different doses (4, 8, 12, 16, and 20 mg/kg body weight [BW]) of ADC were administered intravenously (i.v.) to five groups of randomized 6-week-old nude (nu/nu) mice purchased from Jackson Labs (Bar Harbor, ME). The body weight was measured every two days for 23 days post-injection. Blood samples were collected from tails at 2, 5, 24, 48, 72, and 120 h post-injection (six time points in total for each mouse). Blood was centrifuged at $2000 \times g$ for 5 min to precipitate cells and the supernatant was collected for ELISA. The previously developed PK model was used in this study[41]. Briefly, clearance $(\mathrm{CL}) = \frac{\mathrm{DF}}{2\mathrm{aAUC}} = \frac{V_d}{k_e}$, volume of distribution $(\mathrm{V_d}) = \frac{\mathrm{CL}(t_2 - t_1)}{lnC_1 - lnC_2}$, half-life $\mathrm{t}_{1/2} = \frac{0.693 V_d}{\mathrm{CL}}$, recommended dose $(\mathrm{D}) = C_{\mathrm{max.desired}} k_e V_d T \frac{1 - e^{-k_e}}{1 - e^{k_e T}}$, and dosing interval $(\tau) = \frac{\ln C_{\mathrm{max.desired}} - lnC_{\mathrm{min.desired}}}{k_e} + T$. The calculated D and τ were used in the antitumor efficacy animal study.

In vivo anti-NET efficacy study

The Mycoplasma-free BON-Luc (3×0^6 cells) were injected subcutaneously onto the flank of 4–6-week-old nude (nu/nu) mice (Jackson Labs, Bar Harbor, ME). The NET xenograft mice with tumor volume of 50–60 mm^3 were randomized into three groups ($n = 6$): saline, anti-SSTR2 mAb, and mAb-MMAE conjugate. The mAb or ADC was administrated intravenously through tail vein following a dose of 8 mg/kg BW (empirically determined from PK study) in 50 or 100 µL of saline. The same volume of mAb or saline was injected in control groups. Mice developed palpable nodules within 14 days and tumor volume and mouse body weight were measured every two days. Both electronic caliper and bioluminescence via In Vivo Imaging system (IVIS) were used to monitor tumor size. Four injections were conducted with average injection interval of 4.5 days during the entire treatment period (total of 24 days, our standard 3-week ADC treatment). At the end of the experiment, mice were euthanized to collect tumors and other organs (e.g., brain) for further analysis.

Hematoxylin and eosin (H&E) staining

Tissue samples were dehydrated in ethanol, cleared in xylene, embedded in paraffin, and sectioned at 5 µm with Leica microtome and mounted on frosted microscope slides

(Fisher Scientific). Paraffin sectioned slides were dewaxed with xylene, and gradient hydrated with 100% ETOH, 95% ETOH, 70% ETOH, 50% ETOH, and dH_2O. Slides were immersed in hematoxylin solution for 5 min followed by tap water rinse for 2 mins, 1% HCl in 70% ETOH for 3 dips, 1% NH_4OH until color turned blue and eosin Y solution for 30 s. Finally, slides were dehydrated twice in absolute alcohols for 2 min and cleared in xylene.

Immunohistochemistry (IHC) staining

The 5-μm paraffin sections were used for IHC staining. Tissue microarray slides were rehydrated using xylene and ethanol, then immersed in citrate buffer (BioGenex, Fermont, CA) for a 10-min pressure cooker cycle to achieve antigen retrieval. Endogenous peroxidase activity was quenched by incubating slides in 3% hydrogen peroxide for 10 min. Blocking was performed for 1 h at RT using 3% goat serum in PBS. SSTR2 was detected with an overnight 4 °C incubation using 1.8 mg/mL of anti-SSTR2 mAb (RD Systems mAb in the IHC of TMA and our mAb in other IHC experiments) with final concentration of 10 μg/mL, followed by an anti-mouse biotin-labeled secondary antibody and HRP streptavidin. Slides were stained with DAB kit (Vector, SK-4100) and counter stained with hematoxylin. Before being cover slipped and imaged, slides were dehydrated and cleared using ethanol and xylene.

Scoring of IHC

ImageJ was used for IHC quantitative scoring to analyze the SSTR2 expression or anti-SSTR2 mAb binding. The positive staining (red color) and negative staining (blue color) intensity as quantified using RGB Measure function (Plugins-Analyze-RGB Measure). The SSTR2 expression score was calculated as SSTR2 score = [(red intensity/blue intensity)$_{\text{NET tissues}}$/average of (red intensity/blue intensity)$_{\text{nomal tissues}} - 1] \times 10$. The scoring criteria were defined as high expression (+++, 3): score >3.0, medium expression (++, 2): score of 1.5–2.0, and low expression (+, 1). The five normal tissues (liver, spleen, placenta, prostate, and tonsil) are our negative control samples with SSTR2 score of 0.

Statistical analysis

All the data were presented as mean ± standard error of the mean (SEM). Two-tailed Student's *t*-tests were used to determine the probability of significance between two groups. Comparison among multiple groups was performed using a one-way ANOVA followed by post-hoc (Dunnett's) analysis. The sample size of animal study followed the published ADC therapy study[42]. Statistical significance with ***P-value of <0.001 was considered for all tests.

Results

SSTR2 overexpression in NET

To assess SSTR2 expression, NET tissue microarray slides were first stained with H&E to confirm the presence and location of NET cells in each core (Fig. 1a), then was stained using SSTR2 mAb to evaluate the receptor surface expression. The IHC images were presented in Fig. 1b and the SSTR2 expression scores of each tissue were summarized in Supplemental Table 1. The IHC staining demonstrated that approximately 76% (29/38) of patient tissues cores (2A to 9D) had positive SSTR2 expression with strong cell membrane localization (Fig. 1b), while SSTR2 was not detectable in normal liver, spleen, placenta, prostate, and tonsil tissue cores (1A-1E). Of all the NET tissue samples, 50% (19/38) had very high SSTR2 expression (score: 3), 26% (10/38) showed intermediate expression (score: 2), and 24% (9/38) showed low expression (score: 1). All the SSTR2 scores of NET tissues were higher than the five normal tissues. The scores of 2 and 3 were defined as strong expression in this study. Moreover, the IHC staining of the 33 types of normal human tissues with our anti-SSTR2 mAb showed that there was no detectable SSTR2 surface expression in most of these normal organs except pancreas and skin, which had weak signal (Fig. 2a). The Human Atlas Project database reported a high level of SSTR2 mRNA in brain, lung, liver, skin, placenta, prostate, tonsil, and pancreas. However, the high-resolution images of these normal organs showed minimal or undetectable surface SSTR2 (Fig. 2b).

Development of anti-SSTR2 mAb to target NET

The hybridoma clones secreting anti-SSTR2 mAb were screened using ELISA to identify the top mAb clones with strong binding to the 1st, the 2nd or both extracellular domains of SSTR2 (Fig. 3a). In flow cytometry analysis, the surface binding capacity of these four mAbs to BON-1 cells was 50%, 80%, 90%, and 98%, respectively (Fig. 3b). Clone 4 was defined as the "lead clone", fully characterized, and used throughout the remainder of the study. An isotype analysis revealed that the lead clone is IgG1 kappa, and SDS-PAGE analysis confirmed its molecular weight of 150 kDa (Fig. 3c). Further evaluation showed that the anti-SSTR2 mAb had high surface binding to NET cell lines BON-1 and QGP-1 (>90%) and low binding to fibroblast cell lines 917 and WI-38 (<7.5%)

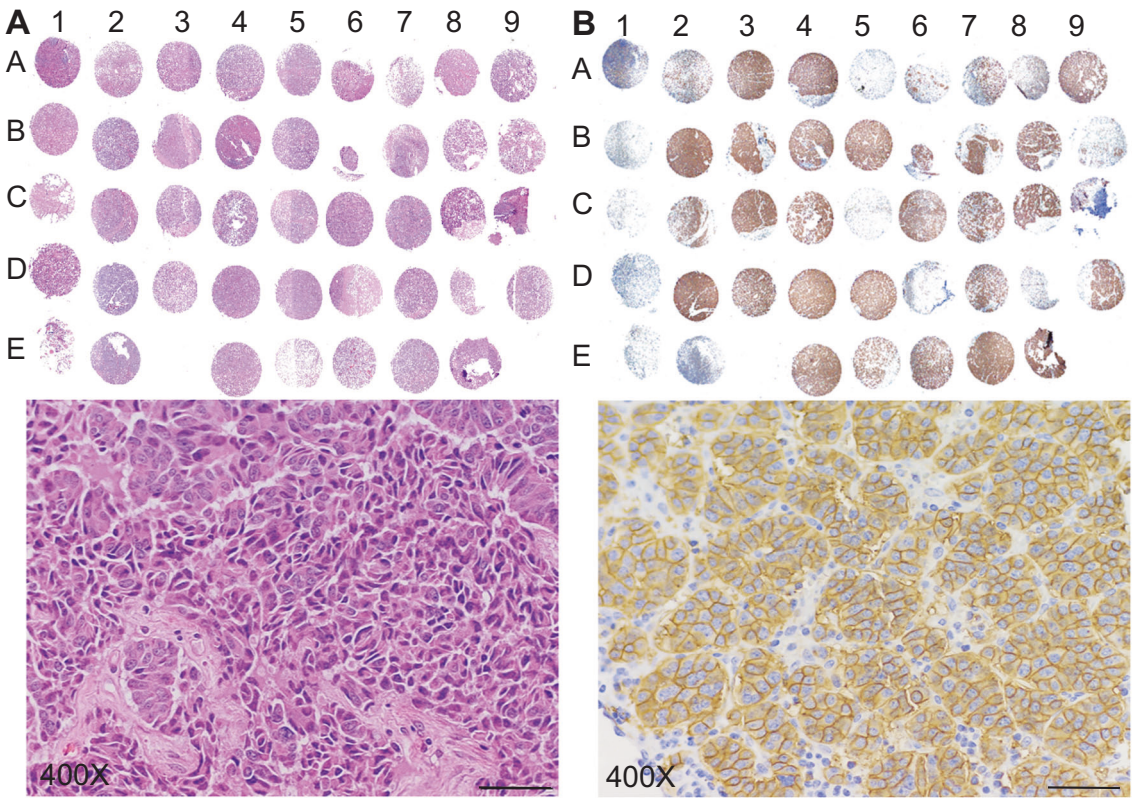

Fig. 1 Tissue microarray (TMA) to detect SSTR2 expression in patients. a H&E staining of the TMA including human pancreatic NET tissues (columns 2–9, $n = 38$) and normal tissues (control, column 1, $n = 5$). **b** IHC analysis of SSTR2 in the TMA. Scale bar equals 20 μm.

(Fig. 3d). Additionally, we cloned and sequenced the mAb, and confirmed the novelty of our anti-SSTR2 mAb (PCT patent TH Docket No. 222119-8030). To optimally produce mAb, we adapted the adherent hybridoma cells to suspension culture in stirred-tank bioreactors (Fig. 3e). The cultures in T-flask, spinner flask, and stirred-tank bioreactor generated 8.6, 39.8, and 53.3 mg/L of anti-SSTR2 mAb with a specific growth rate of 0.016, 0.024, and 0.035 h^{-1}, respectively.

High surface binding and high affinity to SSTR2

To assess the in vitro NET-specific targeting of our anti-SSTR2 mAb, we performed live-cell, dynamic CLSM imaging and flow cytometry analysis. The AF647-mAb accumulated on the BON-1 cell surface, displayed as a "red circle", within 20 min post incubation due to immunoaffinity (Fig. 4a). The mAb was then internalized through endocytosis and localized in cytoplasm (detected with BacMam GFP control) within 40 min. Also our anti-SSTR2 mAb exhibited much stronger surface binding to BON-1 cells than the commercial mAb (R&D Systems), 95 ± 3% vs. 38 ± 2% (Fig. 4b). The UniProtKB database shows that the extracellular domains of human SSTR2 targeted by our mAb have no similarity with those in human SSTR1, 3, 4, and 5 (Supplemental Table 2), indicating that the cross-reactivity among SSTRs is minimal. Moreover, human SSTR2 (UniProt P30874) and mouse SSTR2 (UniProt P30875) have the same topology, and the 1st and the 2nd extracellular domains of human SSTR2 that our mAb targets have 100% similarity with mouse SSTR2. Western blotting (Fig. 4c) confirmed that our anti-SSTR2 mAb can bind the SSTR2 present in human BON-1 xenografts, as consistent with our previous study, which showed our mAb can specifically target the BON-Luc xenograft in mouse model[43], and bind the mouse SSTR2 in isolated medullary thyroid carcinoma (MTC, type of neuroendocrine thyroid cancer) tissue from a spontaneous MTC mouse model[44,45]. Additionally, the antibody affinity experiment showed that our anti-SSTR2 mAb had equilibrium dissociation constant (K_D) of 6.7 nM and 6.6 nM to human SSTR2 and mouse SSTR2, respectively. All these data revealed that the SSTR2 mAb developed in this study can bind both human and mouse SSTR2.

Anti-SSTR2 ADC construction

Our previously established cysteine-based conjugation procedure was used to construct ADC, where a rebridging

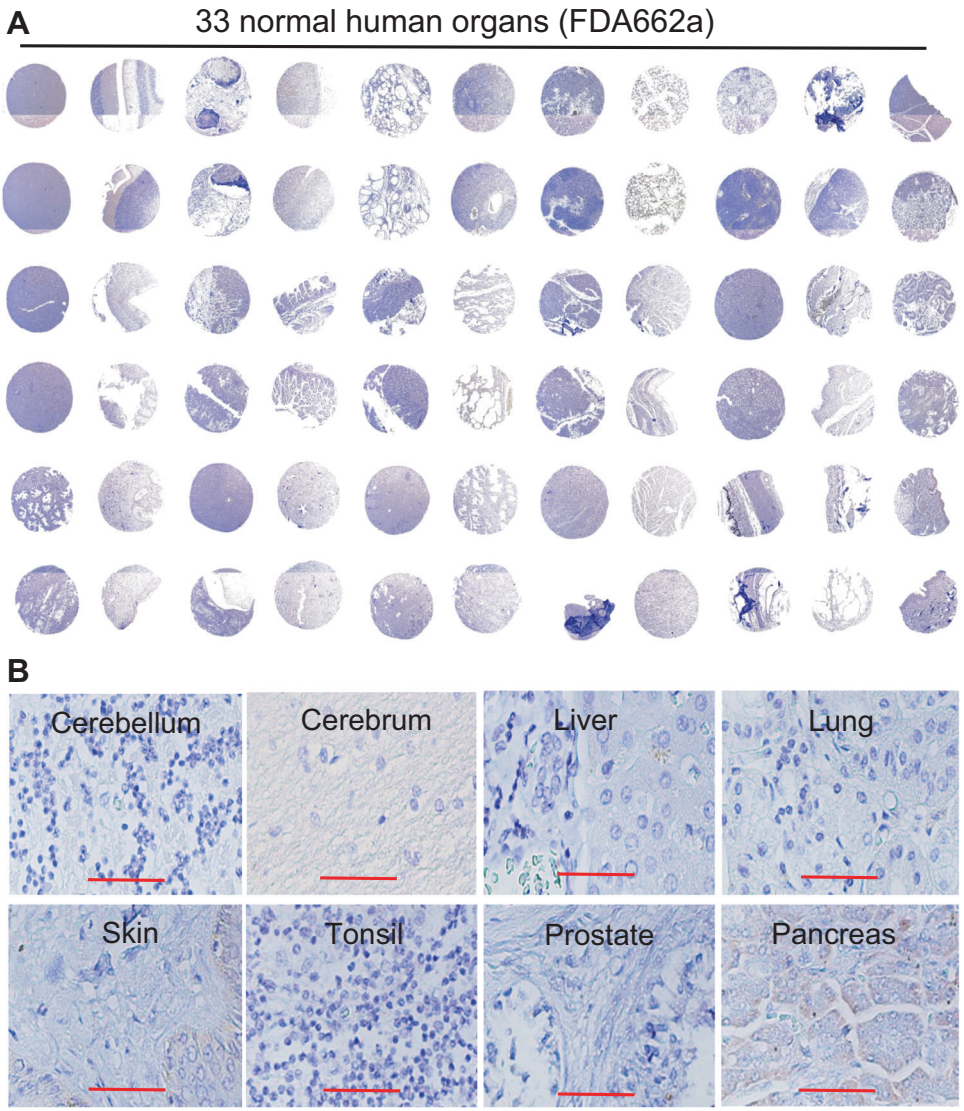

Fig. 2 Evaluation of the NET-specific targeting of our anti-SSTR2 antibody using IHC of normal human organs. a Surface SSTR2 staining in 33 normal human organs (US Biomax, FDA662a, $n = 2$), including cerebrum, cerebellum, peripheral nerve, adrenal gland, thyroid gland, spleen, thymus, bone marrow, lymph node, tonsil, pancreas, liver, esophagus, stomach, small intestine, colon, lung, salivary, pharynx, kidney, bladder, testis, prostate, penis, ovary, uterine tube, breast, endometrium, cervix, cardiac muscle, skeletal muscle, mesothelium, and skin. **b** Representative high-resolution IHC imaging of cerebellum, cerebrum, liver, lung, skin, tonsil, prostate, and pancreas. Scale bar equals 50 μm.

peptide-based linker was synthesized to maintain mAb integrity during the MMAE conjugation (Fig. 5a)[38]. The Agilent 6500 Q-TOF LC/MS confirmed the right structure of linker, and SDS-PAGE confirmed the high integrity of ADC structure (Fig. 5b). The drug-to-antibody ratio (DAR) of the constructed ADC was ~4.0.

In vitro ADC cytotoxicity

We evaluated the in vitro anticancer cytotoxicity of the ADC in BON-1 cells by comparing free drug (MMAE) and two ADCs constructed using the anti-SSTR2 mAb developed in this study or the R&D Systems mAb. MMAE is a highly potent cytotoxin that can block microtubulin polymerization[46–49]. The average final viabilities were 31.6%, 39.3%, and 19.8%, viable cell numbers were 15,800, 19,625, and 9900 cells/mL, and IC_{50} values were 2.00, 4.27, and 5.62 nM post a 3-day treatment with MMAE, ADC constructed using our mAb, and ADC constructed using commercial mAb, respectively (Fig. 5c). Thus, the mAb-MMAE ADC and free drug had similar cytotoxic potency for NET cells.

Tolerated dose

To investigate the tolerated dose, five different doses of anti-SSTR2 ADC were injected into nude (nu/nu) mice (nontumor bearing) via tail vein: 4, 8, 12, 16, and 20 mg/kg BW ($n = 2$). Mice were monitored twice daily for a total of 21 days and showed no overt changes in general health including water intake, breathing, and locomotion. ADC at a dose range of 4–20 mg/kg BW had no obvious effects on body weight or overall survival (Fig. 6a). At the end of the study, mice were sacrificed to collect major organs (brain, lung, heart, kidney, and liver) for further studies. Since The Human Atlas Project reported the highest level of SSTR2 mRNA brain, so we performed H&E staining of brain

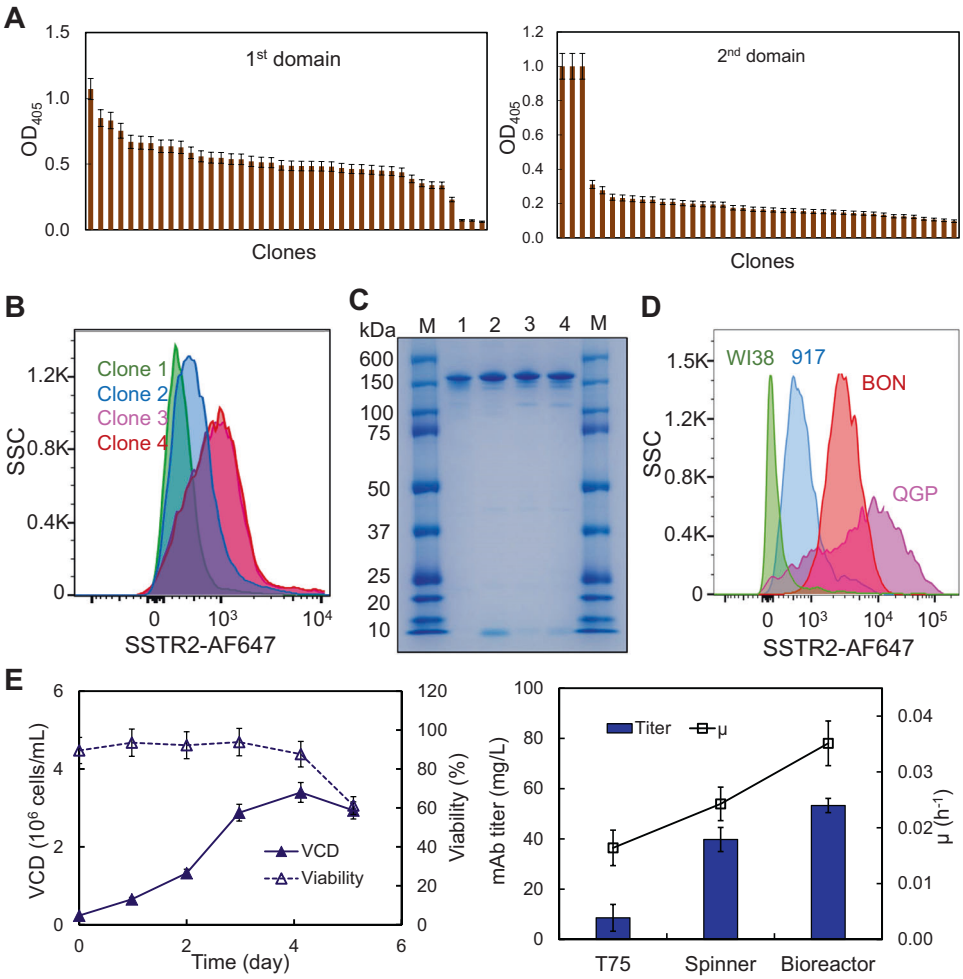

Fig. 3 Anti-SSTR2 mAb development and production. **a**, Rank of top anti-SSTR2 mAb clones based on the titer in ELISA screening (data represent mean ± SEM, $n = 3$). **b** Evaluation of top four clones using flow cytometry. **c** SDS-PAGE to confirm the integrity and purity of mAb (M: marker; 1–4: Clones 1–4). **d** Evaluation of SSTR2 binding of lead clone in control cell lines (WI-38 and 917) and NET cell lines (BON and QGP). **e** mAb production and hybridoma cell growth in fed-batch suspension cultures (data represent mean ± SEM, $n = 3$). Viable cell density (VCD): ▲, cell viability: △, specific growth rate (μ): □.

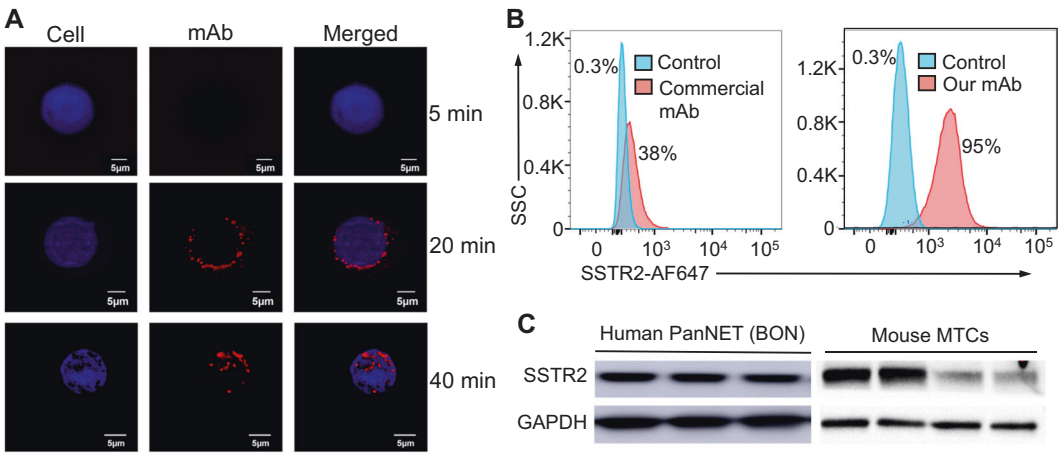

Fig. 4 Evaluation of surface binding by anti-SSTR2 mAb. **a** Live-cell CLSM dynamic imaging of anti-SSTR2 mAb. Two-color CLSM: whole cell labeled with GFP (displayed as blue) and SSTR2 mAb-MMAE labeled with AF647 (red). Scale bar equals 5 μm. **b**, Flow cytometry to analyze the surface binding of anti-SSTR2 mAb to NET cell (BON-1) and negative control cell (917). Stained with 1 μg of mAb-AF647/million cells on ice for 30 min. **c** Western blotting of human NET (BON) xenografted tissue and mouse MTC tissues ($n = 3$–4) using our mAb.

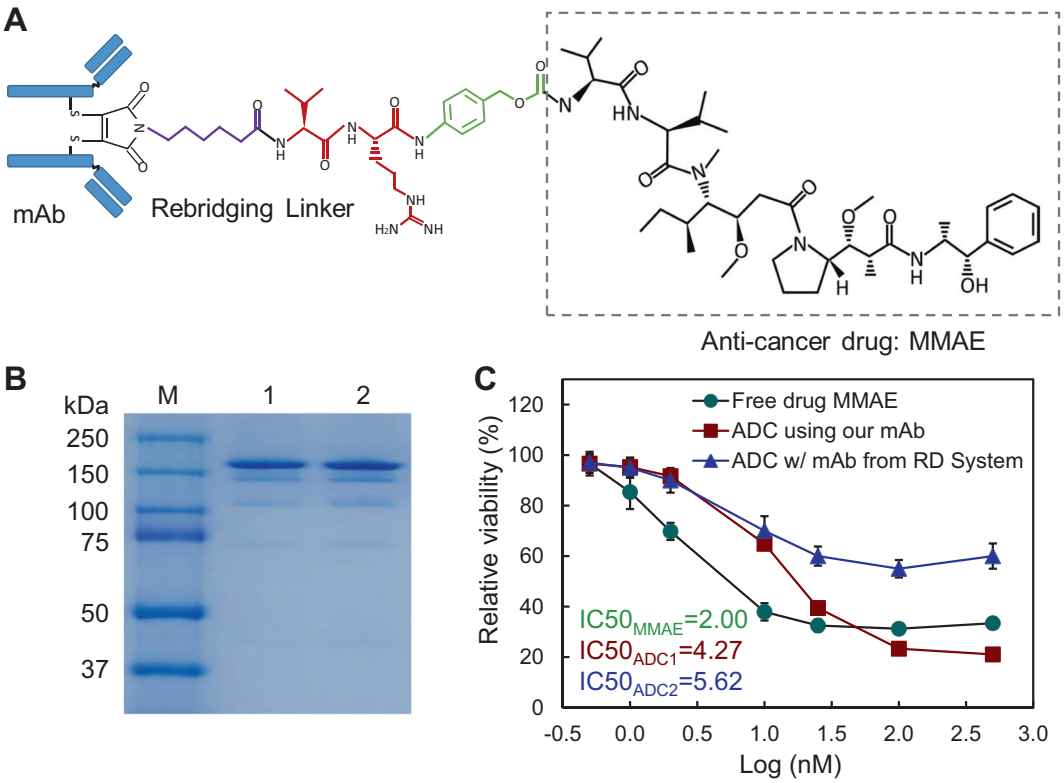

Fig. 5 ADC construction and in vitro characterization. a Molecule structure of anti-SSTR2 mAb-MMAE using rebridging linker. **b** SDS-PAGE to check the integrity of mAb-MMAE. **c** The IC_{50} anticancer toxicity of free drug (●), ADC constructed using commercial anti-SSTR2 mAb (R&D Systems, ▲), and ADC constructed using our anti-SSTR2 mAb (■) (data represent mean ± SEM, $n = 3$).

tissue. To detect if normal brain is affected or damaged by any possible off-target, we performed H&E staining. As shown in Fig. 6b, brain tissue had no obvious morphology change or necrosis after ADC treatment, indicating that our anti-SSTR2 ADC did not cause cytotoxicity in normal brain. These results indicated that the anti-SSTR2 ADC therapy had no evident off-target effects in vivo.

Pharmacokinetics (PK)

A PK study was conducted, where ADC intravenously injecting into nude mice at five doses of 4, 8, 12, 16, and 20 mg/kg. Plasma samples were collected (10–50 µL) from the tail at 0, 2, 8, and 16 h, and 1, 2, 3, 5, and 7 days post-ADC injection and titrated for ADC by ELISA (Fig. 6c). The PK modeling indicated that the serum half-life ($t_{1/2}$) = 1.38–2.33 days, Cmax = 72–196 µg/mL, recommended dose (D) = 3.78–14.30 mg/kg BW, and recommended dosing interval (τ) = 4.40–9.10 days. Therefore, based on the calculated D and τ, we selected a dose of 8 mg/kg with administration interval of 4–5 days for the remaining in vivo anti-NET study. Our standard ADC treatment period (3 weeks) was used to simulate the clinical ADC therapy. Moreover, we titrated the plasma samples that were collected from the anti-NET efficacy study using HPLC and detected no cleaved MMAE in plasma, indicating the high conjugation (linker) stability of ADC.

In vivo antitumor efficacy

The mice bearing BON-Luc xenografts were treated in a dosing interval of 4.5 days with either anti-SSTR2 ADC (8 mg/kg), anti-SSTR2 mAb (8 mg/kg, control), or saline (vehicle, control) in three groups ($n = 6$). Figure 7a showed that tumor growth was significantly attenuated with a tumor volume of 62–67% in the ADC treatment group compared to controls ($p \le 0.001$). The tumor fluorescence flux was measured with IVIS, showing 71–73% of signal in the treatment group compared to controls (Fig. 7b, $p \le 0.001$). Terminal tumor weight measurement further confirmed the significant treatment efficacy of ADC (Fig. 7c, d). In order to evaluate the toxicity of ADC, we continued measuring body weight in tumor-bearing mice. As expected, there was no obvious difference among the three groups in overall body weight change, further supporting that the toxicity of ADC was limited or well tolerated (Fig. 7e). The SSTR2 expression in NET tumors during treatment was confirmed in western blot analysis (Fig. 7f). The surface staining of SSTR2 in tumors

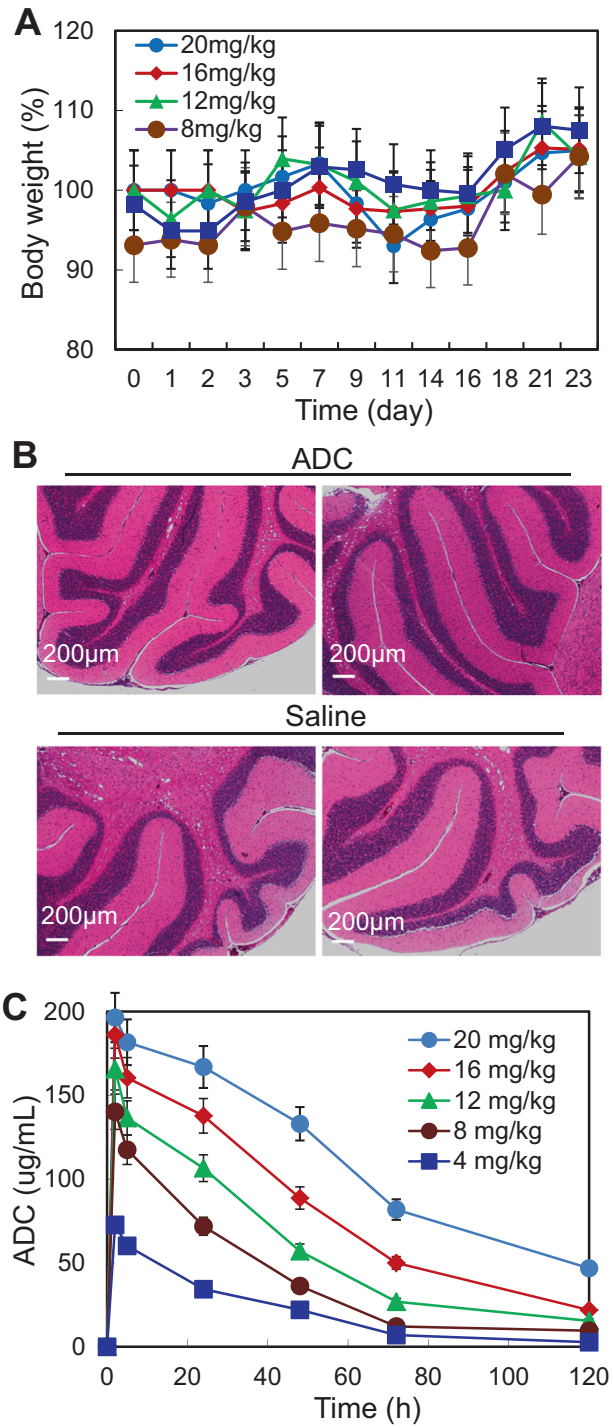

Fig. 6 TD and PK studies of ADC. a TD to test the effect of five ADC dosages including 4, 8, 12, 16, and 20 mg/kg BW. **b** H&E staining of brain tissues. Scale bar equals to 200 μm. **c** PK to evaluate the stability and kinetics parameters of ADC (data represent mean ± SEM).

from ADC treatment group appeared to be lower than the control group (Fig. 7g), likely due to the NET cell death caused by ADC which was confirmed through H&E staining (Fig. 7h). These findings support the hypothesis that our anti-SSTR2 ADC is an effective drug delivery vehicle with antitumor efficacy and a tolerable toxicity profile.

Discussion

To develop the effective and safe targeted cancer therapies, a unique biomarker that specifically defines the cancer cells from the noncancerous cells must be identified and thoroughly characterized. The Human Atlas Project reports high mRNA expression of SSTR2 in several normal human tissues (such as brain), but our study showed that the surface protein expression in these tissues (and other normal tissues) is low or undetectable. Our IHC staining of 33 normal human organs showed that spleen and tonsil had no detectable surface SSTR2 expression. The published autoradiography and IHC revealed that SSTRs were mainly located in the red pulp of the spleen, which contains diffusely distributed SSTRs[50–53]. The difference could be caused by the different spleen sections used in literature and our IHC staining (i.e., red pulp vs. white pulp) or different detection reagents (i.e., SST analog binding to various SSTR receptors in literature vs. high SSTR2-specific mAb in this study). Unlike our IHC staining of tonsil, the proteinatlas reported medium SSTR2 expression in squamous epithelial cells but no expression in germinal center cells and non-germinal center cells in tonsil. This difference could be caused by the section preparation or the detection reagent used in IHC staining. In future we need to further analyze the SSTR2 surface expression in squamous epithelial cells and compare our anti-SSTR2 mAb with other commercial staining reagents.

There are five SSTR subtypes (SSTR1-5) expressed in tumors and normal tissues. Leijon et al.'s previous IHC staining of 151 primary pheochromocytomas and paragangliomas. Their results showed that 74.8% NETs had strong or intermediate SSTR2 expression while tumors had variable individual SSTR3 profiles, and 71.4% metastasized NETs had strong expression of membrane SSTR2 but low expression of cytoplasmic and granular SSTR3[25]. In addition to overall expression, Fotouhi et al. reported that SSTR2 expression was downregulated when small intestinal NET cells progressed through the small intestinal layers[54]. These studies demonstrated that the SSTR2 expression in NETs is highly heterogenous. This study only investigated the overall SSTR2 expression in NET samples and the surface SSTR2 binding of our new mAb. In future we will analyze the SSTR2 expression heterogeneity in NET samples and also perform an in vivo biodistribution study using advanced positron emission tomography (PET).

Although several studies reported SSTR2 protein expression in central nervous system, gastrointestinal tract,

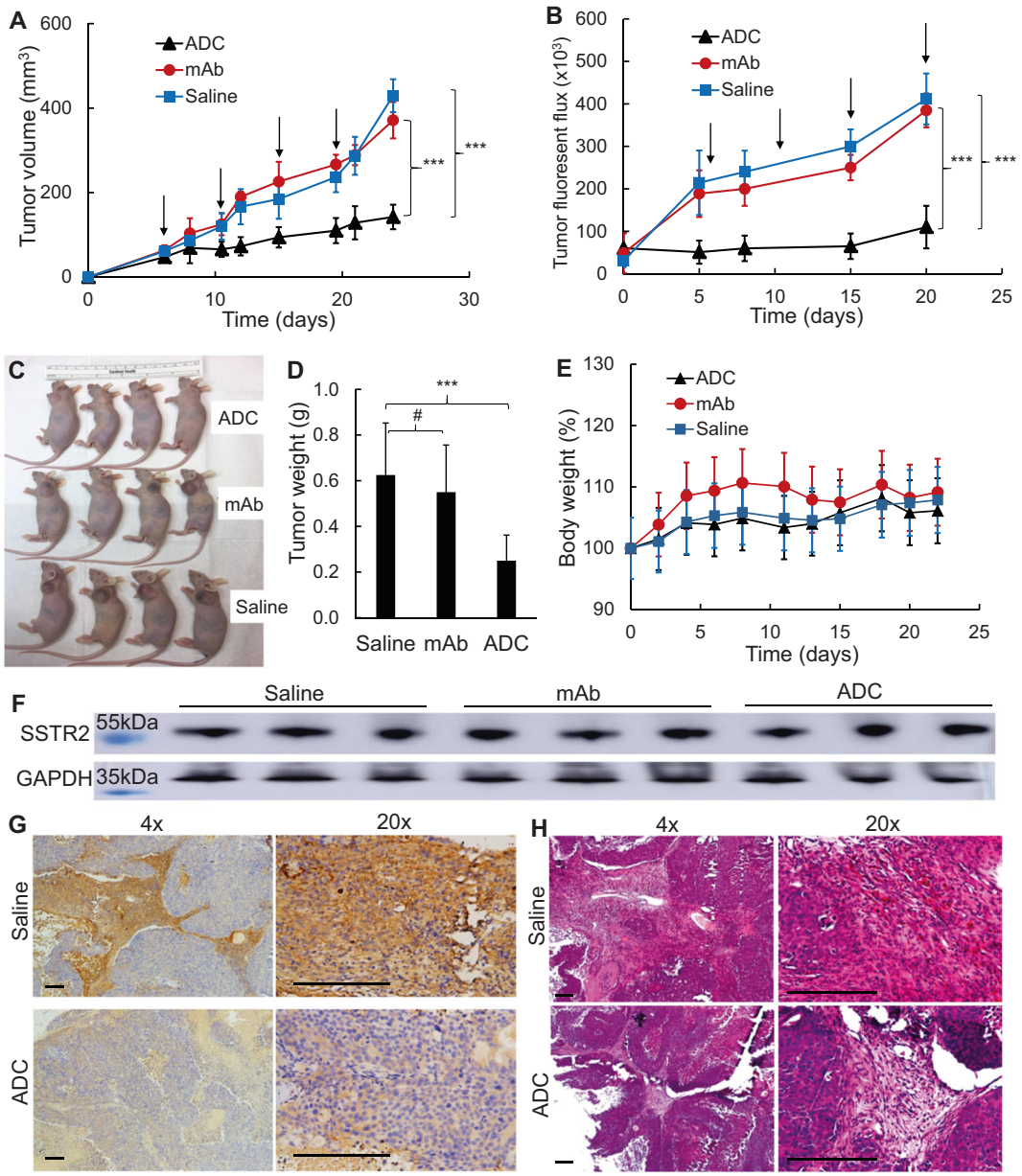

Fig. 7 Antitumor efficacy study of ADC in NET (BON-Luc) xenografted mouse model. a Tumor volume changes after BON-Luc cells injection and treatment (data represent mean ± SEM, $n = 6$). 3×10^6 mycoplasma-free BON-Luc cells were subcutaneously injected into nude mice. Saline, ADC, or mAb were administrated on Day 6, 10.5, 15, 19.5. Tumor size was measured with calipers and volume was calculated as ellipsoid. Tumor volumes between three groups were analyzed with mixed design ANOVA and multiple comparison. $***p < 0.001$. Black arrow indicating ADC (8 mg/kg BW) treatment date. **b** Tumor fluorescence flux measurement with IVIS image system (data represent mean ± SEM, $n = 6$). **c** Tumor-bearing mice harvested. **d** Wet weight of the tumors excised from harvested mice. Statistical analysis was done with one-way ANOVA, and multiple comparison. #, nonsignificant. $***p \le 0.001$. **e** Body weight changes of three treatment groups. ▲: treatment group injected with ADC, ●: control group injected with mAb, and ■: control group injected with saline. **f** Western blotting of tumors from represented mice ($n = 3$). **g** Representative images of IHC of SSTR2 with tumor tissues in saline and ADC groups ($n = 3$). Scale bar equals to 50 μm. **h** Representative images of H&E staining with tumor tissues in saline and ADC groups ($n = 3$). Scale bar equals 50 μm.

and pancreas[55], the surface expression of SSTR2 in NET tissues was confirmed >20-fold higher than that in normal tissues. Considering that ADC is a dose-dependent targeted therapy, the drastically high expression in NETs allows safe targeting of the SSTR2 with therapeutic drugs. Moreover, our study and other studies[22–24] demonstrate that more than 70% of NET patients abundantly express SSTR2. All the results collected from patient tumor tissues, normal organs, and cell lines demonstrate that SSTR2 is an ideal receptor for targeted cancer therapy.

Supporting our findings, not all patients with NETs overexpress SSTR2[56,57]. For example, only 45–66% of pulmonary NET patients and 80–95% gastroenteropancreatic NET patients overexpress SSTR2[56]. To benefit the SSTR2-negative patients, we performed a comparative membrane proteomics study and found that the carcinoembryonic antigen-related cell adhesion molecule 1 (CEACAM1) has high expression in pancreatic NET cells (BON-1 and QGP-1) but not in non-NET cancerous pancreatic adenocarcinoma cells (PANC-1 and MiAPaCa-1) and noncancerous fibroblast cell (WI-38). High CEACAM1 expression has been suggested in various cancers, including medullary thyroid cancer which represents a type of NET[58,59]. Although further evaluation is needed, CEACAM1 might be an alternative receptor for ADC therapy in NET patients with minimal SSTR2 density.

In this study, we developed, characterized and confirmed a novel monoclonal antibody to target the identified SSTR2 receptor for NET therapy. Unlike a commercially available mAb developed using the whole SSTR2 membrane protein as immunogen, our anti-SSTR2 mAb was designed to selectively target two extracellular domains of SSTR2. As a result, our mAb showed a higher and more specific surface binding to NET cells than the commercial mAb. The new mAb was also designed to exhibit strong cross-reactivity to both human and mouse SSTR2, allowing the results presented here to be more translatable to test and use in human patients. Importantly, the maximum tolerated dose study we performed did not detect any adverse body weight or behavior changes at dose of up to 20 mg ADC/kg. For example, no histopathology was detected in murine brain tissue where the highest SSTR2 mRNA expression occurs. Furthermore, the constructed anti-SSTR2 monoclonal antibody-drug significantly reduced the tumor growth in s.c. xenograft mice. Taken together, the developed anti-SSTR2 mAb can specifically target the SSTR2-overexpressing NET cell lines, patient-derived tissues and xenografts, and the targeting delivered potent small molecule via ADC has high cytotoxicity to NET with minimal side effects.

Lutathera that combines the endoradiotherapy ([^{177}Lu]Lu-DOTA-TATE) with its diagnostic partner [^{68}Ga]Ga-DOTA-TATE or [^{68}Ga]Ga-DOTA-TOC (DOTA-(D-Phe1, Tyr3)-octreotide has been approved to treat SSTR positive gastroenteropancreatic NET[19,20]. The mechanism is to target SSTRs positive lesions using SST analogue and kill cells via the DNA damage provoked by ^{177}Lu. The disadvantages of this therapy are: the radiopharmaceutical shelf life is short (i.e., 72 h from the time point of calibration at the end of production); the active concentration changes over time due to the decay of ^{177}Lu; and the therapeutic impact on rapidly proliferating NETs is relatively poor. Moreover, the FDA-approved SST analogue (e.g., octreotide LAR) with long-term stability has been used for diagnosis and imaging. Clinical trials show that octreotide effectively improves NET symptoms such as diarrhea, flushing, bronchoconstriction, and carcinoid cardiac disease but does not demonstrate obviously improvement of the overall survival[60,61]. As compared to Lutathera, our new anti-SSTR2 mAb-based ADC has the advantages of longer shelf life, higher cytotoxicity to treat NET, and potential to improve survival of patients. As compared to octreotide, our anti-SSTR2 mAb has higher specificity to target the membrane SSTR2, which can be used as diagnosis reagent and SSTR2-targeted delivery vehicle. We will evaluate and compare our ADC with Lutathera and octreotide in future.

Previous studies have reported that SSTR2 involves in apoptosis, regulation of cyclin-dependent kinase inhibitors, and inhibition of proliferation signaling[62,63]. These findings indicated that the anti-SSTR2 mAb could regulate NET cell growth *via* SSTR2-mediated signaling cascades, but it needs a full investigation in future study. Moreover, the possible synergism of mAb and ADC-delivered cytotoxic payload, the optimal ADC dosage and treatment strategy, and a full MTD study will be performed in vivo. Also it is imperative to further evaluate the potential side effects, particular with regards to the patients demonstrating low-level SSTR2 expression.

In conclusion, our anti-SSTR2 ADC has a great potential to treat NET due to its capability or potential to target SSTR2 positive NET, reduce undesirable side effects, and effectively reduce NET growth.

Acknowledgements We would like to thank Dr. J. Bart Rose and Ms. Rachael Guenter and the Tissue-Based Translational Research Lab in the Department of Pathology at University of Alabama at Birmingham (UAB) for the design and construction of the tissue microarray.

Funding This work was supported by SDHB Pheo Para Coalition (J.A.B.), National Institute of Health (NIH) R21HL 127599A1 (L.Z.), NIH R21CA226491-01A1 (R.J. and X.M.L.), NIH 1R01CA238273-01A1 (X.M.L.), and North American Neuroendocrine Tumor Society (NANETS) Basic/Translational Science Investigator award (R.J.).

Conflict of interest The authors declare that they have no conflict of interest.

References

1. Yao JC, Hassan M, Phan A, Dagohoy C, Leary C, Mares JE, et al. One hundred years after "carcinoid": epidemiology of and prognostic factors for neuroendocrine tumors in 35,825 cases in the United States. J Clin Oncol. 2008;26:3063–72.
2. Kulke MH, Benson AB,3rd, Bergsland E, Berlin JD, Blaszkowsky LS, Choti MA, et al. Neuroendocrine tumors. J Natl Compr Canc Netw. 2012;10:724–64.
3. Chen H, Hardacre JM, Uzar A, Cameron JL, Choti MA. Isolated liver metastases from neuroendocrine tumors: does resection prolong survival. J Am Coll Surg. 1998;187:88–92.

4. Norton JA. Endocrine tumours of the gastrointestinal tract. Surgical treatment of neuroendocrine metastases. Best Pr Res Clin Gastroenterol. 2005;19:577–83.
5. Mayo SC, de Jong MC, Pulitano C, Clary BM, Reddy SK, Gamblin TC, et al. Surgical management of hepatic neuroendocrine tumor metastasis: results from an international multi-institutional analysis. Ann Surg Oncol. 2010;17:3129–36.
6. Adler JT, Meyer-Rochow GY, Chen H, Benn DE, Robinson BG, Sippel RS, et al. Pheochromocytoma: current approaches and future directions. Oncologist. 2008;13:779–93.
7. Pinchot SN, Pitt SC, Sippel RS, Kunnimalaiyaan M, Chen H. Novel targets for the treatment and palliation of gastrointestinal neuroendocrine tumors. Curr Opin Investig Drugs. 2008;9:576–82.
8. Chen H, Pruitt A, Nicol TL, Gorgulu S, Choti MA. Complete hepatic resection of metastases from leiomyosarcoma prolongs survival. J Gastrointest Surg. 1998;2:151–5.
9. Chen H. Therapeutic options for patients with metastatic gastrointestinal carcinoid. J Surg Oncol. 2008;97:203–4.
10. Shiba S, Morizane C, Hiraoka N, Sasaki M, Koga F, Sakamoto Y, et al. Pancreatic neuroendocrine tumors: a single-center 20-year experience with 100 patients. Pancreatology. 2016;16:99–105.
11. Brown KT, Koh BY, Brody LA, Getrajdman GI, Susman J, Fong Y, et al. Particle embolization of hepatic neuroendocrine metastases for control of pain and hormonal symptoms. J Vasc Inter Radiol. 1999;10:397–403.
12. Isozaki T, Kiba T, Numata K, Saito S, Shimamura T, Kitamura T, et al. Medullary thyroid carcinoma with multiple hepatic metastases: treatment with transcatheter arterial embolization and percutaneous ethanol injection. Intern Med. 1999;38:17–21.
13. Lal A, Chen H. Treatment of advanced carcinoid tumors. Curr Opin Oncol. 2006;18:9–15.
14. Lehnert T. Liver transplantation for metastatic neuroendocrine carcinoma: an analysis of 103 patients. Transplantation. 1998;66: 1307–12.
15. Zhang R, Straus FH, DeGroot LJ. Effective genetic therapy of established medullary thyroid carcinomas with murine interleukin-2: dissemination and cytotoxicity studies in a rat tumor model. Endocrinology. 1999;140:2152–8.
16. Boudreaux JP, Putty B, Frey DJ, Woltering E, Anthony L, Daly I, et al. Surgical treatment of advanced-stage carcinoid tumors: lessons learned. Ann Surg. 2005;241:839–45.
17. Nguyen C, Faraggi M, Giraudet AL, de Labriolle-Vaylet C, Aparicio T, Rouzet F, et al. Long-term efficacy of radionuclide therapy in patients with disseminated neuroendocrine tumors uncontrolled by conventional therapy. J Nucl Med. 2004;45: 1660–8.
18. Fiorentini G, Rossi S, Bonechi F, Vaira M, De Simone M, Dentico P, et al. Intra-arterial hepatic chemoembolization in liver metastases from neuroendocrine tumors: a phase II study. J Chemother. 2004;16:293–7.
19. Oberg K, Kvols L, Caplin M, Delle Fave G, de Herder W, Rindi G, et al. Consensus report on the use of somatostatin analogs for the management of neuroendocrine tumors of the gastroenteropancreatic system. Ann Oncol. 2004;15:966–73.
20. Hennrich U, Kopka K, Lutathera R. The first FDA- and EMA-approved radiopharmaceutical for peptide receptor radionuclide therapy. Pharmaceuticals (Basel). 2019;12:114–21.
21. Ferguson SS. Evolving concepts in G protein-coupled receptor endocytosis: the role in receptor desensitization and signaling. Pharm Rev. 2001;53:1–24.
22. Pinchot SN, Holen K, Sippel RS, Chen H. Carcinoid tumors. Oncologist. 2008;13:1255–69.
23. Zatelli MC, Tagliati F, Taylor JE, Rossi R, Culler MD, degli Uberti EC, et al. Somatostatin receptor subtypes 2 and 5 differentially affect proliferation in vitro of the human medullary thyroid carcinoma cell line tt. J Clin Endocrinol Metab. 2001; 86:2161–9.
24. Sun LC, Coy DH. Somatostatin receptor-targeted anti-cancer therapy. Curr Drug Deliv. 2011;8:2–10.
25. Leijon H, Remes S, Hagstrom J, Louhimo J, Maenpaa H, Schalin-Jantti C, et al. Variable somatostatin receptor subtype expression in 151 primary pheochromocytomas and paragangliomas. Hum Pathol. 2019;86:66–75.
26. Zhou L, Xu N, Sun Y, Liu XM. Targeted biopharmaceuticals for cancer treatment. Cancer Lett. 2014;352:145–51.
27. Almasbak H, Aarvak T, Vemuri MC. CAR T cell therapy: a game changer in cancer treatment. J Immunol Res. 2016;2016:5474602.
28. Dai H, Wang Y, Lu X, Han W. Chimeric antigen receptors modified T-cells for cancer therapy. J Natl Cancer Inst. 2016;108:439–52.
29. Zhang BL, Qin DY, Mo ZM, Li Y, Wei W, Wang YS, et al. Hurdles of CAR-T cell-based cancer immunotherapy directed against solid tumors. Sci China Life Sci. 2016;59:340–8.
30. Little M, Kipriyanov SM, Le Gall F, Moldenhauer G. Of mice and men: hybridoma and recombinant antibodies. Immunol Today. 2000;21:364–70.
31. Stump B., Steinmann J. Conjugation process development and scale-up. Methods Mol Biol. 2013;1045:235–48.
32. Saunders LR, Bankovich AJ, Anderson WC, Aujay MA, Bheddah S, Black K, et al. A DLL3-targeted antibody-drug conjugate eradicates high-grade pulmonary neuroendocrine tumor-initiating cells in vivo. Sci Transl Med. 2015;7:302ra136.
33. Pereira DS, Guevara CI, Jin L, Mbong N, Verlinsky A, Hsu SJ, et al. AGS67E, an anti-CD37 monomethyl auristatin E antibody-drug conjugate as a potential therapeutic for B/T-cell malignancies and AML: a new role for CD37 in AML. Mol Cancer Ther. 2015;14:1650–60.
34. Whalen KA, White BH, Quinn JM, Kriksciukaite K, Alargova R, Au Yeung TP, et al. Targeting the somatostatin receptor 2 with the miniaturized drug conjugate, PEN-221: a potent and novel therapeutic for the treatment of small cell lung cancer. Mol Cancer Ther. 2019;18:1926–36.
35. Kiaris H, Schally AV, Nagy A, Szepeshazi K, Hebert F, Halmos G, et al. A targeted cytotoxic somatostatin (SST) analogue, AN-238, inhibits the growth of H-69 small-cell lung carcinoma (SCLC) and H-157 non-SCLC in nude mice. Eur J Cancer. 2001;37:620–8.
36. Sun L, Fuselier JA, Coy DH. Effects of camptothecin conjugated to a somatostatin analog vector on growth of tumor cell lines in culture and related tumors in rodents. Drug Deliv. 2004;11:231–8.
37. Xu N, Ou J, Gilani A-K, Zhou L, Liu M. High-level expression of recombinant IgG1 by CHO K1 platform. Front Chem Sci Eng. 2015;9:376–80.
38. Ou J, Si Y, Goh K, Yasui N, Guo Y, Song J, et al. Bioprocess development of antibody-drug conjugate production for cancer treatment. PLoS ONE. 2018;13:e0206246.
39. Xu N, Ou J, Si Y, Goh KY, Flanigan DD, Han X, et al. Proteomics insight into the production of monoclonal antibody. Biochemical Eng J. 2019;145:177–85.
40. Hasegawa K, Kudoh S, Ito T. Somatostatin receptor staining in FFPE sections using a ligand derivative dye as an alternative to immunostaining. PLoS ONE. 2017;12:e0172030.
41. Xu N., Liu M., Liu M. Pharmacology, Pharmacokinetics, and Pharmacodynamics of Antibodies. Biosimilairs of Monoclonal Antibodies. John Wiley & Sons, Inc. New Jersey, USA, 2016.
42. Sherbenou DW, Aftab BT, Su Y, Behrens CR, Wiita A, Logan AC, et al. Antibody-drug conjugate targeting CD46 eliminates multiple myeloma cells. J Clin Invest. 2016;126:4640–53.
43. Si Y, Kim S, Zhang E, Tang Y, Jaskula-Sztul R, Markert JM, et al. Targeted exosomes for drug delivery: biomanufacturing, surface tagging, and validation. Biotechnol J. 2020;15:1900163–74.

44. Pozo K, Castro-Rivera E, Tan C, Plattner F, Schwach G, Siegl V, et al. The role of Cdk5 in neuroendocrine thyroid cancer. Cancer Cell. 2013;24:499–511.
45. Pozo K, Hillmann A, Augustyn A, Plattner F, Hai T, Singh T, et al. Differential expression of cell cycle regulators in CDK5-dependent medullary thyroid carcinoma tumorigenesis. Oncotarget. 2015;6:12080–93.
46. Francisco JA, Cerveny CG, Meyer DL, Mixan BJ, Klussman K, Chace DF, et al. cAC10-vcMMAE, an anti-CD30-monomethyl auristatin E conjugate with potent and selective antitumor activity. Blood. 2003;102:1458–65.
47. Yao H, Jiang F, Lu A., Zhang G. Methods to design and synthesize antibody-drug conjugates (ADCs). Int J Mol Sci. 2016;17:194–209.
48. Cunningham D, Parajuli KR, Zhang C, Wang G, Mei J, Zhang Q, et al. Monomethyl auristatin E phosphate inhibits human prostate cancer growth. Prostate. 2016;76:1420–30.
49. Li H, Yu C, Jiang J, Huang C, Yao X, Xu Q, et al. An anti-HER2 antibody conjugated with monomethyl auristatin E is highly effective in HER2-positive human gastric cancer. Cancer Biol Ther. 2016;17:346–54.
50. Sarikaya I, Sarikaya A, Alnafisi N, Alenezi S. Significance of splenic uptake on somatostatin receptor imaging studies. Nucl Med Rev Cent East Eur. 2018;21:66–70.
51. Melis M, Kaemmerer D, de Swart J, Kulkarni HR, Lupp A, Sanger J, et al. Localization of radiolabeled somatostatin analogs in the spleen. Clin Nucl Med. 2016;41:e111–4.
52. Reubi JC, Waser B, Horisberger U, Krenning E, Lamberts SW, Gebbers J-O, et al. In vitro autoradiographic and in vivo scintigraphic localization of somatostatin receptors in human lymphatic tissue. Blood. 1993;82:2143–51.
53. Reubi JC, Ursula H, Kappeler A, Laissue JA. Localization of receptors for vasoactive intestinal peptide, somatostatin, and substance P in distinct compartments of human lymphoid organs. Blood. 1998;92:191–7.
54. Fotouhi O, Zedenius J, Hoog A, Juhlin CC. Regional differences in somatostatin receptor 2 (SSTR2) immunoreactivity is coupled to level of bowel invasion in small intestinal neuroendocrine tumors. Neuroendocrinol Lett. 2018;39:305–9.
55. Cakir M, Dworakowska D, Grossman A. Somatostatin receptor biology in neuroendocrine and pituitary tumours: part 1–molecular pathways. J Cell Mol Med. 2010;14:2570–84.
56. Righi L, Volante M, Tavaglione V, Bille A, Daniele L, Angusti T, et al. Somatostatin receptor tissue distribution in lung neuroendocrine tumours: a clinicopathologic and immunohistochemical study of 218 'clinically aggressive' cases. Ann Oncol. 2010;21:548–55.
57. Sherman SK, Maxwell JE, Carr JC, Wang D, O'Dorisio MS, O'Dorisio TM, et al. GIPR expression in gastric and duodenal neuroendocrine tumors. J Surg Res. 2014;190:587–93.
58. Thies A, Moll I, Berger J, Wagener C, Brummer J, Schulze HJ, et al. CEACAM1 expression in cutaneous malignant melanoma predicts the development of metastatic disease. J Clin Oncol. 2002;20:2530–6.
59. Tilki D, Irmak S, Oliveira-Ferrer L, Hauschild J, Miethe K, Atakaya H, et al. CEA-related cell adhesion molecule-1 is involved in angiogenic switch in prostate cancer. Oncogene. 2006;25:4965–74.
60. Hejna M, Schmidinger M, Raderer M. The clinical role of somatostatin analogues as antineoplastic agents: much ado about nothing? Ann Oncol. 2002;13:653–68.
61. Yau H, Kinaan M, Quinn SL, Moraitis AG. Octreotide long-acting repeatable in the treatment of neuroendocrine tumors: patient selection and perspectives. Biologics. 2017;11:115–22.
62. Guillermet J, Saint-Laurent N, Rochaix P, Cuvillier O, Levade T, Schally AV, et al. Somatostatin receptor subtype 2 sensitizes human pancreatic cancer cells to death ligand-induced apoptosis. Proc Natl Acad Sci USA. 2003;100:155–60.
63. Lahlou H, Guillermet J, Hortala M, Vernejoul F, Pyronnet S, Bousquet C, et al. Molecular signaling of somatostatin receptors. Ann N. Y Acad Sci. 2004;1014:121–31.

Surgery 167 (2020) 189–196

Contents lists available at ScienceDirect

Surgery

journal homepage: www.elsevier.com/locate/surg

Overexpression of somatostatin receptor type 2 in neuroendocrine tumors for improved Ga68-DOTATATE imaging and treatment

Rachael Guenter, BS[a], Tolulope Aweda, PhD[b], Danilea M. Carmona Matos, BS, MS[a,c], Samuel Jang, MD[a], Jason Whitt, PhD[a], Yi-Qiang Cheng, PhD[d], X. Margaret Liu, PhD[e], Herbert Chen, MD, FACS[a], Suzanne E. Lapi, PhD[b], Renata Jaskula-Sztul, PhD[a,*]

[a] Department of Surgery, University of Alabama at Birmingham School of Medicine, Birmingham, AL
[b] Department of Radiology, University of Alabama at Birmingham, Birmingham, AL
[c] San Juan Bautista School of Medicine, Caguas, PR
[d] Department of Pharmaceutical Sciences, University of North Texas Health Science Center, Fort Worth, TX
[e] Department of Biomedical Engineering, University of Alabama at Birmingham, Birmingham, AL

ARTICLE INFO

Article history:
Accepted 29 May 2019
Available online 16 October 2019

ABSTRACT

Background: Neuroendocrine tumors are found throughout the body, including the pancreas. These tumors are phenotypically and genetically heterogeneous and can be difficult to accurately image using current imaging standards. However, positron emission tomography/computed tomography with radiolabeled somatostatin analogs has shown clinical success because many neuroendocrine tumors overexpress somatostatin receptor subtype 2. Unfortunately, patients with poorly differentiated neuroendocrine tumors often have a diminished level of somatostatin receptor subtype 2. We found that histone deacetylase inhibitors can upregulate the functional expression of somatostatin receptor subtype 2.

Methods: We evaluated the effect of histone deacetylase inhibitors on somatostatin receptor subtype 2 expression at the mRNA and protein level in neuroendocrine tumor cell lines. The effect of histone deacetylase inhibitors on surface somatostatin receptor subtype 2 was also investigated by fluorescence-activated cell sorting analysis. Changes in somatostatin receptor subtype 2 expression in neuroendocrine tumor xenografts after treatment were imaged using Ga68-DOTATATE positron emission tomography/computed tomography.

Results: The functional increase of somatostatin receptor subtype 2 in neuroendocrine tumors after histone deacetylase inhibitor treatment was confirmed through in vitro experiments and small animal Ga68-DOTATATE positron emission tomography/computed tomography imaging. Histone deacetylase inhibitors increased somatostatin receptor subtype 2 transcription and protein expression in neuroendocrine tumor cell lines. Small animal Ga68-DOTATATE positron emission tomography/computed tomography imaging confirmed the enhancement of radiopeptide uptake after histone deacetylase inhibitor administration.

Conclusion: This study demonstrates a new method to potentially improve imaging and treatments that target somatostatin receptor subtype 2 in neuroendocrine tumors.

Introduction

Neuroendocrine tumors encompass a group of hormone-secreting neoplasms found in various sites throughout the body. Although rare, poorly differentiated neuroendocrine tumors (NETs) are particularly lethal with ineffective treatment options. Pancreatic neuroendocrine tumors (pNETs) are a subtype of neuroendocrine tumors that originate from endocrine cells of the pancreas and can present as well-differentiated tumors, poorly differentiated tumors, functional hormone-secreting tumors, or

Presented at the American Association of Endocrine Surgeons 40th Annual Meeting Los Angeles, CA.

* Reprint requests: Renata Jaskula-Sztul, PhD, Assistant Professor, Department of Surgery, University of Alabama at Birmingham School of Medicine, 1824 6th Avenue South, Wallace Tumor Institute Suite 310H, Birmingham, AL 35233.
E-mail address: sztul@uab.edu (R. Jaskula-Sztul).

https://doi.org/10.1016/j.surg.2019.05.092
0039-6060/

nonfunctional asymptomatic tumors.[1,2] Globally, the incidence of NETs is steadily increasing, with a 5-fold increase in the United States over the past 30 years, potentially owing to improved cancer screening.[2,3] Unfortunately, there has been no improvement in the 5-year overall survival of patients with unresectable disease.[3,4]

Across all subtypes of neuroendocrine cancer, imaging is a critical component in tumor evaluation, detection, and staging. Computed tomography (CT) and positron emission tomography (PET) using various tracers are available to pNET patients, but with limitations arising from the functional differences between well-differentiated and poorly differentiated tumors. Two commonly used tracers for NET PET imaging include either F-18-fluorodeoxyglucose (F18-FDG) or somatostatin receptor (SST) analogs radiolabeled with Ga-68, such as Ga68-DOTATATE, Ga68-DOTATOC, or Ga68-DOTANOC.[5] F18-FDG has shown higher uptake in poorly differentiated NETs compared to well-differentiated NETs, but remains insufficient for detection and staging.[5] Grade 1 and grade 2 NETs are often slow growing with low metabolic activity; therefore, F18-FDG is not highly concentrated.[5] Aside from F18-FDG, Ga68-DOTATATE is an increasingly used tracer for NET evaluation based on the high expression of SSTs in these tumors, with DOTATATE binding with the greatest affinity to somatostatin receptor type 2 (SSTR2). SSTR2 is expressed in 50% to100% of pNETs, with higher levels seen in well-differentiated cases versus poorly differentiated cases.[6] Consequently, the utilization of Ga68-DOTATATE in NETs has proven superior, as exemplified by a study with 25 patients showing that Ga68-DOTATATE had 96% sensitivity for NETs.[5] Although the sensitivity and specificity of SSTR2-specific Ga68-DOTATATE PET/CT imaging has shown to be superior over other imaging modalities, its clinical utility is hampered by variable SSTR2 expression among patients. Patients with low SSTR2 expression are not eligible for SSTR2-based imaging modalities or SSTR2-based peptide receptor radionuclide therapy (PRRT).[7,8] It has been cited that, as tumors dedifferentiate, they can no longer concentrate somatostatin analogs, likely because they lose SST expression.[5,9] Therefore, the ability to reintroduce a high level of functional SSTR2 across all NET patients would allow for improved imaging and assessment of tumor burden and SSTR2-targeting therapies.

Recently, several studies have reported an association between the administration of histone deacetylase (HDAC) inhibitors and increased SSTR2 expression in various cancer cell lines, including pancreatic neuroendocrine cancer cells.[1,10,11] HDACs play a significant role in the transcriptional regulation of genes and the post-translational modification of proteins.[12] HDAC inhibitors are compounds capable of suppressing the activity of HDACs by binding to their catalytic cores, which leads to chromatin relaxation and thus allowing DNA to be bound by transcription factors.[12,13] Currently in the United States, the Food and Drug Administration (FDA) has approved four HDAC inhibitors in the context of cancer therapy: vorinostat, romidepsin, belinostat, and panobinostat. Another HDAC inhibitor, valproic acid (VPA), is in cancer clinical trials and is FDA approved for neurological applications.[12]

In this study, we tested the hypothesis that HDAC inhibitors can upregulate SSTR2 in pNETs through in vitro experiments and small animal PET/CT imaging using Ga68-DOTATATE. The success of this study introduces a potentially new method for increasing the presence of SSTR2 in NET patients with low expression to enable both imaging and potential therapies that target SSTR2.

Materials and methods

All studies described were reviewed and approved by the Institutional Review Board of the University of Alabama at Birmingham.

Cell culture

This study used human pancreatic NET cell lines: BON-1, provided by Dr. Mark Hellmich (University of Texas Medical Branch at Galveston), and QGP-1, obtained from the Japanese Collection of Research Bioresources Cell Bank. BON-1 cells were derived from a peripancreatic lymph node in a patient with metastatic pancreatic cancer and established by Evers et al.[14–15] BON-1 cells were maintained in glutamine (+) DMEM:F-12 medium (Invitrogen Life Technologies, Carlsbad, CA) supplemented with 10% fetal bovine serum, 100 IU/mL penicillin, and 100 μg/mL streptomycin. QGP-1 cells were derived from a primary pancreatic tumor and established by Kaku et al.[16] QGP-1 cells were maintained in glutamine (+) RPMI-1640 medium (Invitrogen Life Technologies, Carlsbad, CA) with 10% fetal bovine serum, 100 IU/mL penicillin, and 100 μg/mL streptomycin. The MIA PaCa-2 and PANC1 cell lines, both derived from pancreatic ductal adenocarcinomas, were obtained from American Tissue Culture Collection (Manassas, VA) and were maintained as described by Gradiz et al.[17] The human embryonic kidney cell line HEK293, obtained from American Tissue Culture Collection (Manassas, VA), was grown in DMEM medium (Invitrogen Life Technologies, Carlsbad, CA) supplemented with 10% fetal bovine serum, 100 IU/mL penicillin, and 100 μg/mL streptomycin. All cell lines were grown at 37°C and in the presence of humidity and 5% CO_2.

Compounds

The HDAC inhibitors romidepsin (FK228), suberoylanilide hydroxamic acid (SAHA), and VPA were purchased from Sigma-Aldrich (St. Louis, MO). The Cheng laboratory provided thailandepsin-A (TDP-A), an analog of FK228, and the Tang laboratory provided AB3.[18,19] All compounds were dissolved in dimethyl sulfoxide (DMSO) (Sigma-Aldrich, St. Louis, MO) and stored at −20°C. The varying concentrations of each HDAC inhibitor used throughout this study are based on previously published data.[19]

Real time quantitative PCR

To isolate RNA, the RNeasy Plus Mini kit (Qiagen, Hilden, Germany) was used. The concentrations of RNA were determined by NanoDrop 1000 spectrophotometer (Thermo Fisher Scientific, Inc, Waltham, MA). Complementary DNA was synthesized from 2μg of total RNA using iScript cDNA Synthesis Kit (Bio-Rad, Hercules, CA). Real-time quantitative PCR was performed in triplicate on CFX Connect Real-Time PCR Detection System (Bio-Rad, Hercules, CA). The sequences of the PCR primers used in this experiment are as follows: SSTR2 forward primer: 5'GAG AAG AAG GTC ACC CGA ATG G 3'; SSTR2 reverse primer: 5' TTG TCC TGC TTA CTG TCA CTC CGC 3'; GAPDH forward primer: 5' ACC TGC CAA ATA TGA TGA C 3'; and GAPDH reverse primer: 5'ACC TGG TGC TCA GTG TAG 3'. Target gene expression was normalized to GAPDH, and the ΔΔCt method was used to calculate relative gene expression. Error bars show the standard error of the mean (SEM).

Western blot analysis

The basal expression of SSTR2 was assessed in the cell lines BON-1, QGP-1, MiPaCa, Panc1, and HEK293T. Cells were treated with DMSO as a control or with a HDAC inhibitor. Whole cell lysates were quantified by BCA Protein Assay Kit (Thermo Fisher Scientific, Waltham, MA). The protein samples were denatured and then resolved by a 4% to 15% Criterion TGX gradient gel (Bio-Rad, Hercules, CA) electrophoresis, transferred onto nitrocellulose membranes (Bio-Rad, Hercules, CA), blocked in milk (1 x PBS, 5% dry skim milk, and 0.05% Tween-20) for 1 hour at room temperature, and incubated in 5% BSA, 1 x PBS with anti-SSTR2 primary antibody (SSTR2 Antibody [A-8]: sc-365502) (Santa Cruz Biotechnology, Dallas, TX) at a 1:500 dilution overnight at 4°C. Secondary antibody (anti-mouse HRP linked antibody 1:1000) (Cell Signaling Technology, Danvers, MA) was applied for 2 hours at room temperature. The protein bands were detected by Luminata Crescendo Western HRP Substrate (Millipore, Burlington, MA). GAPDH expression was used as a loading control.

Flow cytometry

For the fluorescence-activated cell sorting (FACS) analysis, both BON-1 and HEK293 cell lines were treated with either DMSO as a control or 6nM of the HDAC inhibitor FK228 a total of 48 continuous hours. After treatment, a concentration of 1 x 10^6 cells per replicate were stained for 30 minutes at 37°C with 1μg of an anti-SSTR2 antibody (Novus Biologicals, Centennial, CO) labeled with Cy5.5 fluorophore (Lumiprobe Corp, Hunt Valley, MD). Cells were then resuspended in flow buffer (0.5% BSA in sterile PBS) and analyzed using LSR II (BD Biosciences, San Jose, CA) to detect the presence of Cy5.5 signal via Alexa Fluor 700 laser. Data was analyzed using FlowJo V5.0 (Tree Star, Inc, Ashland, OR).

Immunohistochemistry

The tissue microarray was prepared by the University of Alabama at Birmingham (UAB) Research Pathology Core. Biological specimens were obtained from the UAB Surgical Oncology Tumor Bank through an institutional review board–approved protocol. Slides were rehydrated using xylene and ethanol. Antigen retrieval was performed by immersing slides in citrate buffer and placing slides in a pressure cooker for 10 minutes. SSTR2 was detected using an anti-somatostatin receptor 2 antibody (UMB1) - C-terminal (Abcam ab134152) at a 1:200 dilution overnight at 4°C. The next day, an anti-rabbit biotin labeled secondary antibody (Pierce goat anti-rabbit IgG, #31820) was applied to slides for 1 hour at room temperature, followed by 30 minutes of HRP streptavidin incubation. Slides were then stained with DAB Chromogen (Dako Liquid DAB+ substrate K3468) and counter stained with hematoxylin.

Small animal Ga68-DOTATATE PET/CT imaging

Immunocompromised male Nu/Nu mice (Jackson Laboratories, Bar Harbor, ME) were subcutaneously injected with BON-1 cells and xenografts developed to a palpable size in 3 weeks. Two groups of mice were imaged before (basal images) and after injection of either the vehicle control or the HDAC inhibitor FK228. MicroPET images were acquired by tail vein injection of 120to 140 μCi (4.4–5.2 MBq) of Ga68-DOTATATE, which was injected per mouse before and after intra-tumoral injection of FK228. Static scans were collected at 30 minutes and 90 minutes post-injection. A dose of 12.5mg/kg FK228 was administered to the mice receiving the HDAC inhibitor treatment, whereas nontreated mice received an equal volume of the dissolution vehicle (10% ethanol, 60% PEG, 30% PBS) after the basal microPET images were acquired. Then, the mice were imaged again 24 hours after vehicle or FK228 injection. PET and CT images were acquired on a SOFIE GNEXT PET/CT scanner (SOFIE, Culver City, CA). The CT images were reconstructed using a modified Feldkamp algorithm. The PET images were reconstructed using a 3D-ordered subset expectation maximization algorithm (24 subsets and 3 iterations), with random, attenuation, and decay correction. Regions of interest were drawn, and the mean and maximum standard uptake values (SUVs) for tumors were determined using the following formula: SUV = ([MBq/mL] × [animal wt. (g)]/injected dose [MBq]).

Statistical analysis

All statistical analyses were performed using SPSS Statistics for Windows v 25.0 (IBM Corp, Armonk, NY). Differences between treatments for qPCR were determined through 1-way ANOVA followed by a Tukey post-hoc test, and flow cytometry experiments were analyzed using independent *t*-tests. Data was normally distributed. Error bars show the SEM.

Results

Variations in patient SSTR2 expression limit utility of Ga68-DOTATATE PET/CT

To better understand variations in SSTR2 expression in clinical cases, a tissue microarray (TMA) consisting of tissues from 38 different patients with pNETs was stained for SSTR2 expression. An immunohistochemical analysis revealed that 27 of 38 (71%) patients with pNETs had detectable SSTR2 expression. Four representative tissues from patients with pNETs are shown in Fig 1. Both Patient 1 and 2 have grade 2 pNETs with obvious SSTR2 expression, as seen by the brown staining in the cytoplasm and on the cell surface. Patient 3 also has a grade 2 pNET but shows no SSTR2 expression. Patient 4, with a grade 3 pNET, shows minimal cytoplasmic SSTR2 expression. Therefore, this analysis shows that patients with grade 2 or grade 3 pNETs can vary in SSTR2 expression.

Changes in SSTR2 gene expression after HDAC inhibitor treatment

A continuous 24-hour treatment with each of the HDAC inhibitors (FK228, AB3, SAHA, or VPA) had a significant effect on SSTR2 mRNA expression, as determined by a 1-way ANOVA, in both the QGP-1 ($F[10] = 283.998$, $P < .001$) and BON-1 ($F[8] = 162.586$, $P < .001$) pNET cell lines (Fig 2). QGP-1 cells treated with 6nM FK228 (mean ± SEM, 8.89 ± 0.09, $P < .001$), 3μM AB3 (mean ± SEM, 3.89 ± 0.10, $P < .001$), 3μM SAHA (mean ± SEM, 2.50 ± 0.08, $P < .001$), and 4mM VPA (mean ± SEM, 6.05 ± 0.48, $P < .001$) had a significantly higher relative fold expression of SSTR2 mRNA when compared with the DMSO (control) treatment (mean ± SEM, 1.00 ± 0.01). BON-1 cells treated with 6nM FK228 (mean ± SEM, 6.10 ± 0.31, $P < .001$), 3μM AB3 (mean ± SEM, 4.86 ± 0.26, $P < .001$), 3μM SAHA (mean ± SEM, 5.43 ± 0.15, $P < .001$), and 4mM VPA (mean ± SEM, 3.37 ± 0.03, $P < .001$) had a significantly higher relative fold expression of SSTR2 mRNA when compared with the DMSO (control) treatment (mean ± standard deviation [SD], 1.00 ± 0.03). GAPDH was used as a housekeeping gene. Tukey post hoc tests were performed for treatment comparisons. Graphs show mean ± SEM.

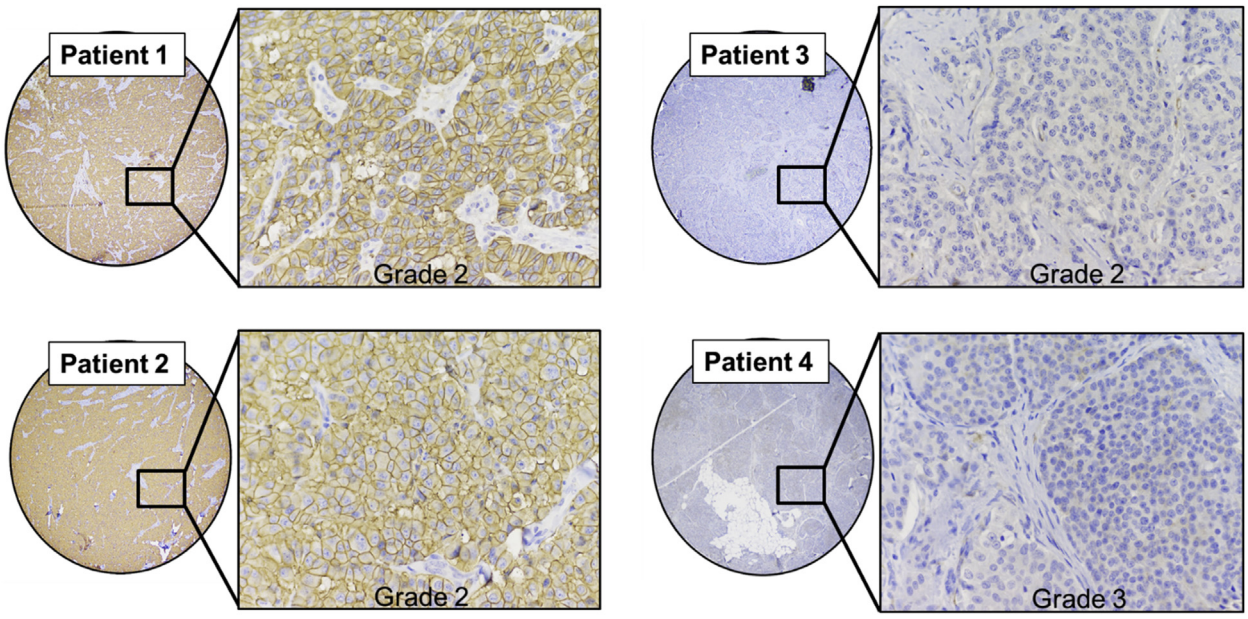

Fig. 1. Tissue microarray of pancreatic neuroendocrine tumors. Variations in SSTR2 expression in 4 representative samples of pNET tissue from patients. Patients 1 and 2 show evident SSTR2 staining present in the cytoplasm and cell membrane. Patients 3 and 4 show weak cytoplasmic or nonexistent SSTR2 staining. (Color version of Fig 1 is available online.)

HDAC inhibitor treatment increases SSTR2 protein expression

The basal level of SSTR2 protein expression was compared between 2 pNET cell lines (QGP-1 and BON-1), 2 pancreatic adenocarcinoma cell lines (MiaPaCa2 and PANC1), and a noncancerous cell line (HEK293T) by Western blot analysis (Fig 3, *A*). The pNET cell line (QGP-1) had higher basal SSTR2 expression than BON-1; therefore, QGP-1 could represent a patient with a high level SSTR2 expression, and BON-1 could be a patient with medium to low SSTR2 expression. Changes in the amount of SSTR2 protein expression in both QGP-1 and BON-1 cells were assessed using Western blotting after a continuous 48-hour treatment with 2 different doses of the following HDAC inhibitors: TDP-A, FK228, AB3, SAHA, or VPA. There was no evident increase in SSTR2 protein expression after treatment with any of the tested HDAC inhibitors in QGP-1 cells (Fig 3, *B*). However, there was an evident increase of SSTR2 expression in BON-1 cells after treatment with all HDAC inhibitors (Fig 3, *C*). These results suggest that HDAC inhibitors could likely induce SSTR2 expression in cells that have low or medium SSTR2 expression (BON-1) and may not have a substantial

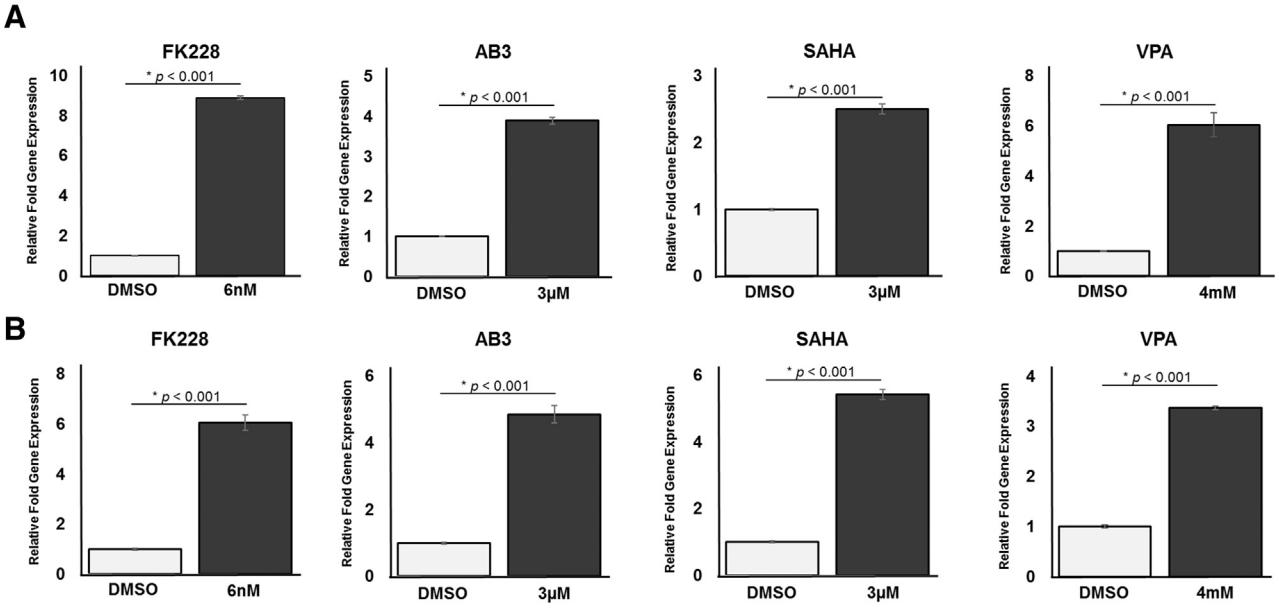

Fig. 2. Upregulation in SSTR2 mRNA expression. (*A*) QGP-1 cells treated with 4 different HDAC inhibitors (FK228, AB3, SAHA, or VPA) showed statistically significant increases in SSTR2 mRNA expression as measured by RT-qPCR. (*B*) BON-1 cells treated with 4 different HDAC inhibitors (FK228, AB3, SAHA, or VPA) also showed statistically significant increases in SSTR2 mRNA expression.

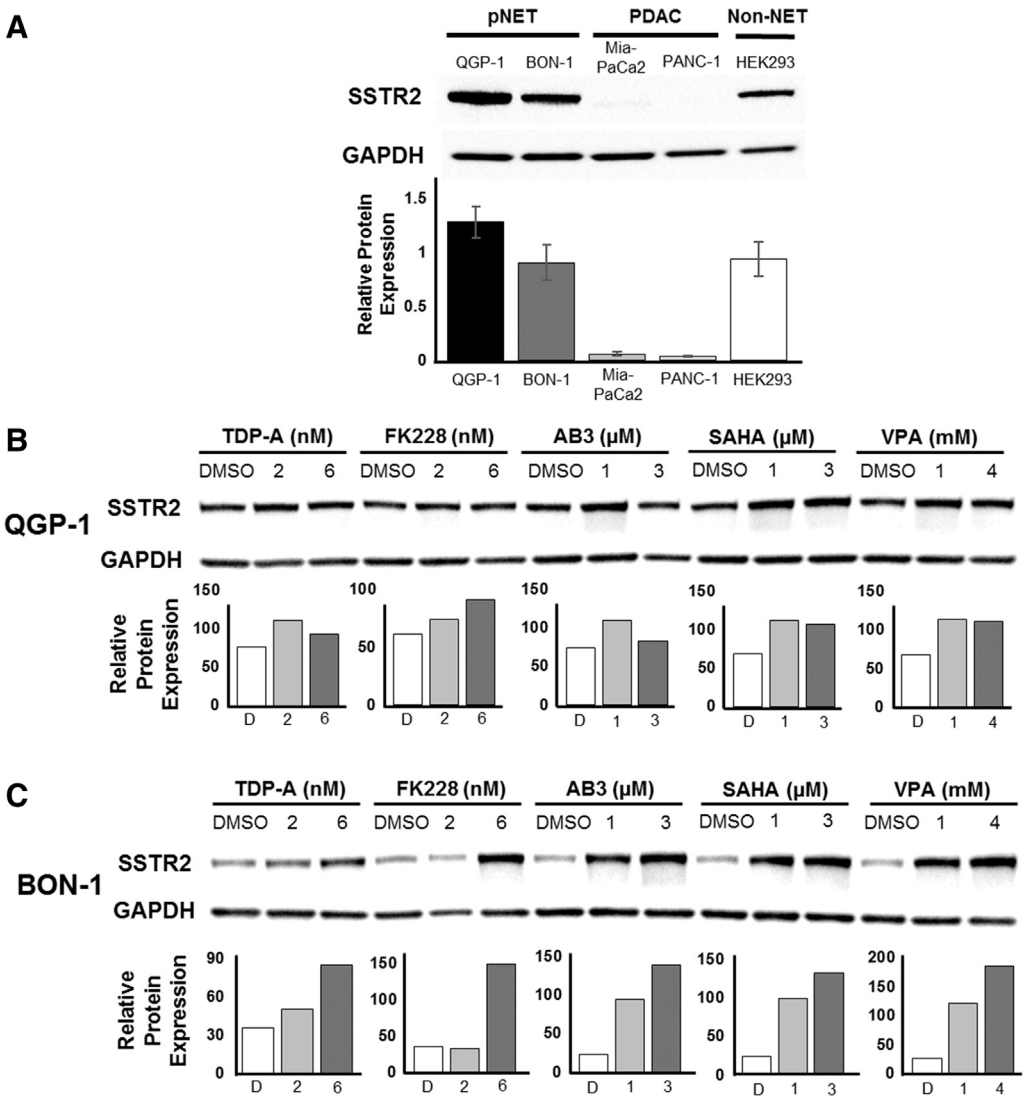

Fig. 3. Changes in SSTR2 protein expression in vitro. (*A*) The average basal expression level of SSTR2 in QGP-1 is higher than BON-1. The average basal SSTR2 expression in the pancreatic adenocarcinoma cell lines (MiaPaCa2 and PANC-1) is lower than both pancreatic neuroendocrine tumor cell lines (QGP-1 and BON-1). The non-cancerous cell line HEK293 was run as a positive control. (*B*) Expression of SSTR2 in QGP-1 (high basal SSTR2 expression) had a 1.7-fold maximum increase of SSTR2 expression with 1mM VPA, whereas (*C*) BON-1 (low basal SSTR2 expression) had 7.2-fold maximum increase in SSTR2 expression with 4mM VPA.

effect on cells with an existing high basal expression of SSTR2 (QGP-1).

Detection of a higher density of SSTR2 on cell surfaces

To determine if the observed increased in SSTR2 expression after treatment with various HDAC inhibitors applied to the detectable, cell surface expression of SSTR2, FACS using a fluorescently labeled anti-SSTR2 antibody was performed on BON-1 cells. In addition, HEK293 were also analyzed as a noncancerous control cell line (Fig 4). Both cell lines were treated continuously for 48 hours with either 6nM of the HDAC inhibitor FK228 or with DMSO as a control. In BON-1 cells, there was a significant increase in the percent of cells that expressed detectable SSTR2 on the cell surface after treatment with 6nM FK228 (mean ± SEM, 33.7 ± 0.20, t = −52.788, $P < .001$), as compared to the DMSO (control) treatment (mean ± SEM, 17.1 ± 0.24) (Fig 4, *A*). Although the HEK293 cell line showed a significant increase in the percent of cells expressing detectable SSTR2 on the cell surface after treatment with 6nM FK228 (mean ± SEM, 6.35 ± 0.17, t = −22.725, $P < .001$) when compared to the DMSO (control) treatment (mean ± SEM, 3.98 ± 0.07), the overall number of positive cells was 2- to 3-fold lower than the BON-1 cell line (Fig 4, *B*). In summary, these results demonstrate that treatment with HDAC inhibitors could increase the functional density of SSTR2 on the surface of NET cells, indicating the potential for improved binding of Ga68-DOTATATE with PET/CT imaging.

Ga68-DOTATATE PET/CT small animal imaging of NET xenografts

Mice bearing BON-1 xenografts demonstrated improved Ga68-DOTATATE binding after HDAC inhibitor administration when imaged using PET/CT (Fig 5). Mice given the vehicle control treatment showed a marginal increase in Ga68-DOTATATE uptake (Fig 5, *A, C*). However, mice treated with the HDAC inhibitor FK228 displayed a significant increase in Ga68-DOTATATE binding (Fig 5, *B, D*). The mice that received HDAC inhibitor administration had an average increase in the SUV of 2.97 ± 0.68 at 30 minutes after Ga68-DOTATATE injection, which was determined to be

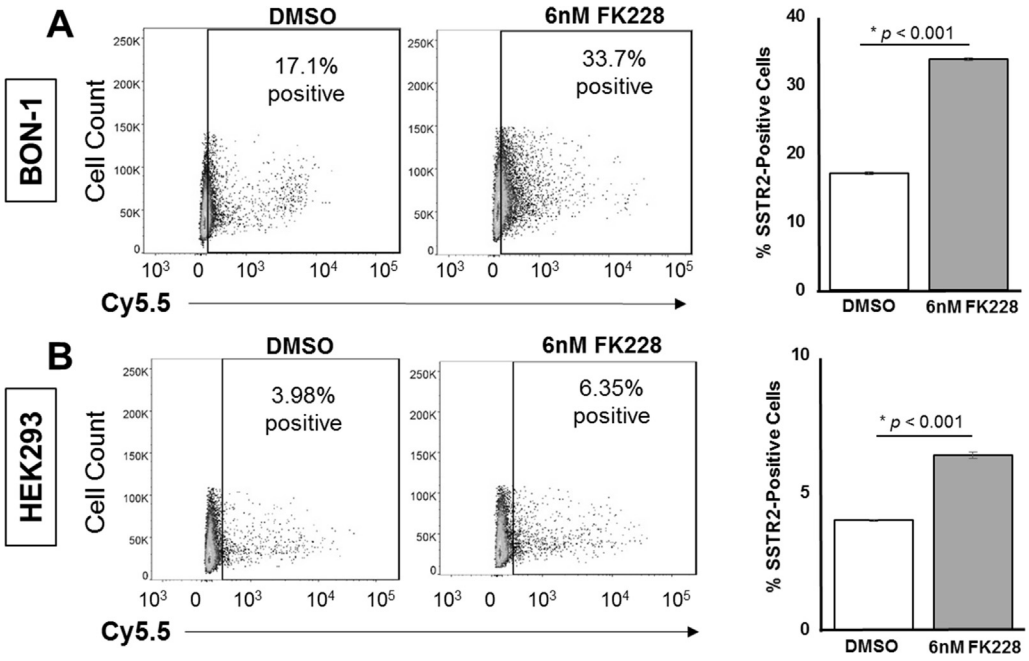

Fig. 4. Increase in surface SSTR2 expression determined by FACS. Treatment with 6nM FK228 showed a significant increase in surface SSTR2 expression in (*A*) BON-1 cells and (*B*) HEK293 cells.

statistically significant. The increase in SUV was 1.43 ± 0.06 (mean ± SD) 90 minutes after Ga68-DOTATATE injection, which was not determined to be statistically significant. The group of mice treated with the vehicle control had average SUV increases of only 0.72 ± 0.10 (mean ± SD) 30 minutes after Ga68-DOTATATE injection and 1.33 ± 0.14 (mean ± SD) 90 minutes after Ga68-DOTATATE injection, indicating improved detection of BON-1 subcutaneous xenografts.

Discussion

NETs are a heterogeneous group of neoplasms that can arise throughout the body from neuroendocrine cells, with 7% cases being classified as pNETs.[8,20] Imaging pNETs is critical because it provides essential information for medical management decisions. PET/CT imaging that utilizes the radiotracer Ga68-DOTATATE is highly specific for pNET detection and has therefore improved

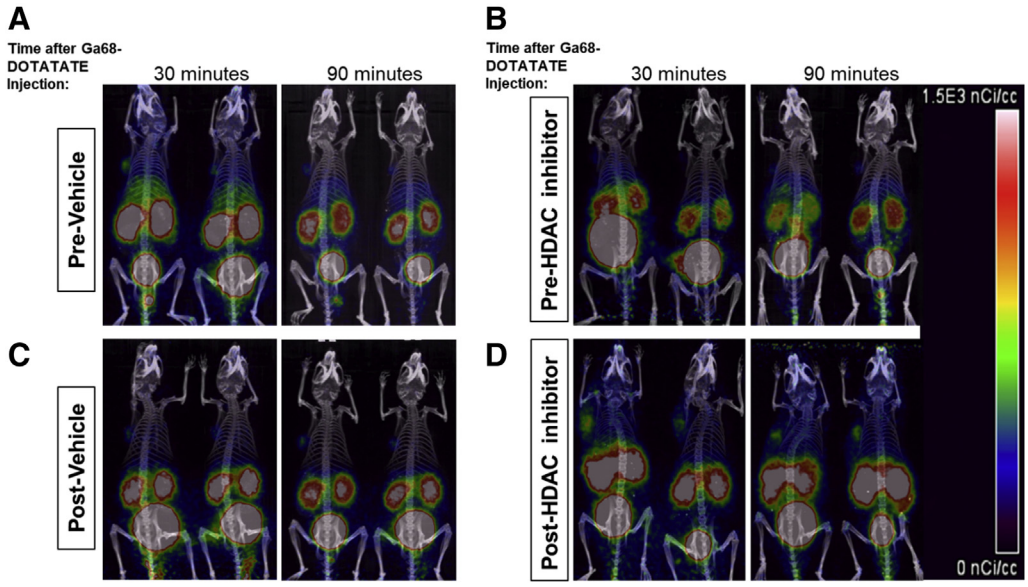

Fig. 5. BON-1 xenografts showed increased Ga68-DOTATATE uptake after HDAC inhibitor (FK228) treatment. Ga68-DOTATATE uptake was assessed before and after vehicle and HDAC inhibitor treatment. Prior to treatment, all mice, pre-vehicle (*A*) and pre-HDAC inhibitor (*B*), were imaged 30 minutes and 90 minutes after Ga68-DOTATATE administration. Then, the mice were treated with either the vehicle or treated with the HDAC inhibitor (FK228). After 24 hours, post-vehicle (*C*) and post-HDAC inhibitor (*D*) treated mice were administered Ga68-DOTATATE and imaged at 30 minutes and 90 minutes, respectively. A significant increase in the SUV of Ga68-DOTATATE uptake was observed after 30 minutes of Ga68-DOTATATE administration to HDAC inhibitor treated mice. There was also a nonsignificant increase in uptake after 90 minutes of Ga68-DOTATATE. (Color version of Fig 5 is available online.)

disease burden assessments and patient management.[8] The success of this technique can be attributed to the specificity of DOTATATE towards SSTR2, a protein overexpressed on most well-differentiated pNET cell membranes. However, patients with pNETs that have little to no SSTR2 expression cannot benefit from this technique. Therefore, in this study we aimed to develop a method of increasing, or re-expressing, SSTR2 in this patient population. In agreement with other studies, we have confirmed that HDAC inhibitors can increase SSTR2 expression in pNET cell lines.[1,10–11] Our results demonstrate that 5 different HDAC inhibitors (TDP-A, FK228, AB3, SAHA, and VPA) increase SSTR2 expression in pNET cell lines at the transcriptional and translational level. The potential mechanism of induction has been speculated to involve the activation of Notch1 in the Notch pathway.[10,11] The functional modulation of SSTR2 on the surface of pNETs was further confirmed by our octreotide affinity study and in vivo PET/CT imaging using Ga68-DOTATATE. The substantial improvement in Ga68-DOTATATE binding by PET/CT after HDAC inhibitor treatment in vivo creates evidence that our method could be translatable to the clinic.

It has been previously reported that the expression of SSTR2 correlates with a positive clinical outcome for patients diagnosed with pNETs.[21,22] In addition to enabling the use of Ga68-DOTATATE PET/CT imaging, patients with increased SSTR2 expression could also become eligible for treatment with PRRT. The upregulation, or re-expression, of SSTR2 in pNETs by HDAC inhibitors has the potential to broaden not only imaging, but also the treatment options for patients.

Consistent with previously published data, the TMA analysis included in this study shows that 29% of pNET patients did not have detectable SSTR2. However, only 1 patient sample on the TMA represented a poorly differentiated pNET, because this type of tumor is not commonly resected and, therefore, tissue is not available to be included on a TMA. The patient tissue from the poorly differentiated pNET did not show SSTR2 expression, which may be attributed the lack of cellular differentiation. Furthermore, our in vitro studies only used 2 available pNET cell lines (QGP-1 and BON-1), in which both had detectable basal SSTR2 expression, as reported in existing literature.[23–25] A pNET cell line representing a patient with undetectable SSTR2 expression is not available to the authors' knowledge. Further studies should be done to expand both in vitro and in vivo studies to better recapitulate the broad spectrum of SSTR2 expression in patients with pNETs.

In conclusion, the results of this study demonstrate a substantial increase in SSTR2 expression in pNET cell lines after the administration of various HDAC inhibitors. This finding suggests that the epigenetic upregulation of the surface marker SSTR2 could improve precision medicine by potentially enabling the use of Ga68-DOTATATE PET/CT imaging for more patients who have been diagnosed with pNETs, in addition to creating a targetable tumor profile for PRRT.

Funding/Support

Research reported in this publication was supported by the National Center for Advancing Translational Sciences of the National Institutes of Health (NCATS NIH) under award number UL1TR001417. The content is the sole responsibility of the authors and does not represent the official views of the National Institutes of Health.

Conflict of interest/Disclosure

The authors declare no conflict of interest.

Acknowledgments

The authors would like to thank Dr. J. Bart Rose, Wayne Howse, Angela Carter, the UAB Flow Cytometry Core, and the Tissue-Based Translational Research Lab in the Department of Pathology at UAB.

References

1. Wanek J, Gaisberger M, Beyreis M, et al. Pharmacological inhibition of class IIa HDACs by LMK-235 pancreatic neuroendocrine tumor cells. *Int J Mol Sci*. 2018;19:3128.
2. Ro C, Chai W, Yu VE, Yu R. Pancreatic neuroendocrine tumors: biology, diagnosis, and treatment. *Chin J Cancer*. 2013;32:312–324.
3. Kawasaki K, Fujii M, Sato T. Gastroenteropancreatic neuroendocrine neoplasms: genes, therapies and models. *Dis Model Mech*. 2018;11:dmm029595.
4. Ilett EE, Langer SW, Olsen IH, Federspiel B, Kjær A, Knigge U. Neuroendocrine carcinomas of the gastroenteropancreatic system: A comprehensive review. *Diagnostics*. 2015;5:119–176.
5. Ambrosini V, Campana D, Tomassetti P, Fanti S. ^{68}Ga-labelled peptides for diagnosis of gastroenteropancreatic NET. *Eur J Nucl Med Mol Imaging*. 2012;39(Suppl 1):S52–S60.
6. Öberg KE, Reubi JC, Kwekkeboom DJ, Krenning EP. Role of somatostatins in gastroenteropancreatic neuroendocrine tumor development and therapy. *Gastroenterology*. 2010;139:742–753.
7. Bodei L, Ambrosini V, Herrmann K, Modlin I. Current concepts in 68Ga-DOTATATE imaging of neuroendocrine neoplasms: interpretation, biodistribution, dosimetry, and molecular strategies. *J Nucl Med*. 2017;58:1718–1726.
8. Tirosh A, Kebebew E. The utility of 68Ga-DOTATATE positron-emission tomography/computed tomography in the diagnosis, management, follow-up and prognosis of neuroendocrine tumors. *Future Oncol*. 2018;14:111–122.
9. Hennigs JK, Müller J, Adam M, et al. Loss of somatostatin receptor subtype 2 in prostate cancer is linked to an aggressive cancer phenotype, high tumor cell proliferation and predicts early metastatic and biochemical relapse. *PLoS One*. 2014;9:e100469.
10. Sun L, He Q, Tsai C, et al. HDAC inhibitors suppressed small cell lung cancer cell growth and enhanced the suppressive effects of receptor-targeting cytotoxins via upregulating somatostatin receptor II. *Am J Transl Res*. 2018;10:545–553.
11. Sun L, Qian Q, Sun G, et al. Valproic acid induces NET cell growth arrest and enhances tumor suppression of the receptor-targeted peptide-drug conjugate via activating somatostatin receptor type II. *J Drug Target*. 2016;24:169–177.
12. Yoon S, Eom GH. HDAC and HDAC inhibitor: from cancer to cardiovascular diseases. *Chonnam Med J*. 2016;52:1–11.
13. Eckschlager T, Plch J, Stiborova M, Hrabeta J. Histone deacetylase inhibitors as anticancer drugs. *Int J Mol Sci*. 2017;18:1414.
14. Evers BM, Ishizuka J, Townsend Jr CM, Thompson JC. The human carcinoid cell line, Bon. A model system for the study of carcinoid tumors. *Ann N Y Acad Sci*. 1994;733:393–406.
15. Evers BM, Townsend Jr CM, Upp JR, et al. Establishment and characterization of a human carcinoid in nude mice and effect of various agents on tumor growth. *Gastroenterology*. 1991;101:303–311.
16. Kaku M, Nishiyama T, Yagawa K, Abe M. Establishment of a carcinoembryonic antigen-producing cell line from human pancreatic carcinoma. *Gan*. 1980;71:596–601.
17. Gradiz R, Silva HC, Carvalho L, Botelho MF, Mota-Pinto A. MIA PaCa-2 and PANC-1 – pancreas ductal adenocarcinoma cell lines with neuroendocrine differentiation and somatostatin receptors. *Sci Rep*. 2016;6:21648.
18. Wang C, Henkes LM, Doughty LB, et al. Thailandepsins: bacterial products with potent histone deacetylase inhibitory activities and broad-spectrum antiproliferative activities. *J Nat Prod*. 2011;74:2031–2038.
19. Jaskula-Sztul R, Chen G, Dammalapati A, et al. AB3-loaded and tumor-targeted unimolecular micelles for medullary thyroid cancer. *J Mater Chem B*. 2017;5:151–159.
20. Lawrence B, Gustafsson BI, Chan A, Svejda B, Kidd M, Modlin IM. The epidemiology of gastroenteropancreatic neuroendocrine tumors. *Endocrinol Metab Clin North Am*. 2011;40:1–18.
21. Song KB, Kim SC, Kim JH, et al. Prognostic value of somatostatin receptor subtypes in pancreatic neuroendocrine tumors. *Pancreas*. 2016;45:187–192.
22. Qian ZR, Li T, Ter-Minassian M, et al. Association between somatostatin receptor expression and clinical outcomes in neuroendocrine tumors. *Pancreas*. 2016;45:1386–1393.
23. Brunner P, Jörg AC, Glatz K, et al. The prognostic and predictive value of sstr2-immunohistochemistry and sstr2-targeted imaging in neuroendocrine tumors. *Eur J Nucl Med Mol Imaging*. 2017;44:468–475.
24. Exner S, Prasad V, Wiedenmann B, Grötzinger C. Octreotide does not inhibit proliferation in five neuroendocrine tumor cell lines. *Front Endocrinol (Lausanne)*. 2018;9:146.
25. Nölting S, Rentsch J, Freitag H, et al. The selective PI3Kα inhibitor BYL719 as a novel therapeutic option for neuroendocrine tumors: Results from multiple cell line models. *PLoS One*. 2017;12:e0182852.

Discussion

Dr Jennifer Rosen (Washington, DC): Thank you for a very useful presentation. I just saw a MEN1 patient and their family who presented with nonfunctional metastatic neuroendocrine tumors. We are trying to figure out what to do for best imaging.

HDAC inhibitors were already approved for use in humans. Why not think about using HDAC inhibitors in patients who are known to have neuroendocrine malignancies in whom who you could do a needle biopsy of the liver as you are thinking about staging and management? I would encourage you to think about early translation since HDAC inhibitors are already approved.

Rachael Guenter: Thank you. I believe romidepsin is FDA approved, and we have also looked at Valproic Acid that is FDA approved. I am not sure it is FDA approved in the context of cancer, but I believe it is for different diseases. Thank you for the excellent suggestion.

Dr Jennifer Rosen (Washington, DC): When it's available for use, I am happy to enroll my patient and their family.

Dr James Howe (Iowa City, IA): This could be very useful clinically. But these high-grade tumors will often show up better on imaging with FDG-PET. If the endpoint is improved imaging, you might choose a different imaging method. I think what you are trying to do is make these cells more susceptible to Lutathera or somatostatin analogues, and that's really the endpoint you are looking for. Is that correct?

Rachael Guenter: Yes, exactly. With FDG PET scans, you can't expand on that. Although that can be more beneficial for the more poorly differentiated neuroendocrine tumors, due to their metabolic activity, it may not be as effective as Ga-DOTATATE imaging. When that does work, it works great. If we can open that up to more patients to benefit from more accurate, more sensitive, more specific imaging and even take that to the next level, as we know there could be SSTR2-based therapies out there, those patients could in turn potentially benefit from that as well.

Dr James Howe (Iowa City, IA): Did you look at any other poorly expressing somatostatin receptor lines like bronchial carcinoids or small cell lung cancer?

Rachael Guenter: Yes, we have looked at other cell lines as well, including the pulmonary carcinoid cell line H727. We plan to expand the studies to various types of the neuroendocrine tumor cell lines.

Surgery 167 (2020) 197–203

Contents lists available at ScienceDirect

Surgery

journal homepage: www.elsevier.com/locate/surg

A growth model of neuroendocrine tumor surrogates and the efficacy of a novel somatostatin-receptor–guided antibody-drug conjugate: Perspectives on clinical response?

Brendon Herring, BS[a], Jason Whitt, PhD[b], Tolulope Aweda, PhD[c], Jianfa Ou, PhD[d], Rachael Guenter, BS[a], Suzanne Lapi, PhD[c], Joel Berry, PhD[d], Herbert Chen, MD, FACS[b], Xiaoguang Liu, PhD[d], J. Bart Rose, MD, MAS[b], Renata Jaskula-Sztul, PhD[b,*]

[a] University of Alabama at Birmingham School of Medicine, AL
[b] Department of Surgery, University of Alabama at Birmingham School of Medicine, AL
[c] Department of Radiology, University of Alabama at Birmingham School of Medicine, AL
[d] Department of Biomedical Engineering, University of Alabama at Birmingham School of Medicine, AL

ARTICLE INFO

Article history:
Accepted 20 April 2019
Available online 19 September 2019

ABSTRACT

Background: As patient-derived xenografts and other preclinical models of neuroendocrine tumors for testing personalized therapeutics are lacking, we have developed a perfused, 3D bioreactor model to culture tumor surrogates from patient-derived neuroendocrine tumors. This work evaluates the duration of surrogate culture and surrogate response to a novel antibody-drug conjugate.
Methods: Twenty-seven patient-derived neuroendocrine tumors were cultured. Histologic sections of a pancreatic neuroendocrine tumor xenograft (BON-1) tumor were assessed for SSTR2 expression before tumor implantation into 2 bioreactors. One surrogate was treated with an antibody-drug conjugate composed of an anti-mitotic Monomethyl auristatin-E linked to a somatostatin receptor 2 antibody. Viability and therapeutic response were assessed by pre-imaging incubation with IR-783 and the RealTime-Glo AnnexinV Apoptosis and Necrosis Assay (Promega Corporation, Madison, WI) over 6 days. A primary human pancreatic neuroendocrine tumor was evaluated similarly.
Results: Mean surrogate growth duration was 34.8 days. Treated BON-1 surrogates exhibited less proliferation (1.2 vs 1.9-fold) and greater apoptosis (1.5 vs 1.1-fold) than controls, whereas treated patient-derived neuroendocrine tumor bioreactors exhibited greater degrees of apoptosis (13- vs 9-fold) and necrosis (2.5- vs 1.6-fold).
Conclusion: Patient-derived neuroendocrine tumor surrogates can be cultured reliably within the bioreactor. This model can be used to evaluate the efficacy of antibody-guided chemotherapy ex vivo and may be useful for predicting clinical responses.

Published by Elsevier Inc.

Introduction

Gastroenteropancreatic neuroendocrine tumors (GEP-NETs) are a heterogeneous group of neoplasms that originate in a diverse array of anatomic locations and have widely variable clinical presentations. With their incidence and prevalence increasing steadily, possibly due to increased accuracy and availability of crosssectional imaging, GEP-NETs are the second most prevalent gastrointestinal malignancy, second only to colorectal cancer.[1] Although a small number of systemic therapies exist relative to other malignancies, including everolimus (an mTOR inhibitor), sunitinib (a tyrosine kinase inhibitor), and traditional chemotherapeutics, these interventions have widely variable response rates and can have debilitating side effects.[2–6]

Over recent years, efforts to improve the efficacy and tolerability of systemic therapies for NETs have led to the development of NET-targeted therapeutic agents. Because many well-differentiated NETs have been shown to overexpress somatostatin receptors (SSTRs), particularly SSTR2 and SSTR5, a number of advances in NET treatment and detection have targeted the SSTRs. Somatostatin (SST) analogues, such as octreotide, have become the first-line

* Reprint requests: Renata Jaskula-Sztul, PhD, University of Alabama at Birmingham School of Medicine, 1824 6th Avenue South, Wallace Tumor Institute Suite 310H, Birmingham, AL 35233.
E-mail address: sztul@uab.edu (R. Jaskula-Sztul).

https://doi.org/10.1016/j.surg.2019.04.073
0039-6060/Published by Elsevier Inc.

therapy for well-differentiated GEP-NETs, whereas peptide-receptor radionuclide therapy (PRRT), such as ^{177}Lutetium DOTATATE therapy, and SSTR scintigraphy (^{68}Gallium-DOTATOC and ^{68}Gallium-DOTATATE), have proven to have valuable theranostic applications.[7] The success of these tumor-targeted modalities indicates a promising area for the development of antibody-drug conjugates (ADCs), which allow pharmacologic agents to be delivered specifically to neoplasms expressing the target epitopes. Hence, ADCs permit lesser minimum effective doses of otherwise unacceptably cytotoxic compounds to be administered, improving their therapeutic indices while minimizing side effects.[8]

A further challenge to improving NET therapy exists in the relative dearth of preclinical models for predicting the clinical responses of individual patients to these systemic therapies. As cultivating primary cultures has proven nearly impossible for NETs, few human-derived NET cell lines exist, and establishing patient-derived xenograft (PDX) models for NETs has proven difficult.[9,10] This study proposes the use of a previously characterized 3D, flow-perfusion bioreactor system as an ex vivo model for evaluating the response of human NETs to potential therapeutics, allowing therapy to be personalized to the individual patient (precision therapy).[11] To illustrate the utility of this system, an ADC comprised of a proprietary antibody to SSTR2 covalently linked to Monomethyl auristatin E (MMAE), a highly cytotoxic tubulin polymerization inhibitor derived from the mollusk *Dolabella auricularia*, was evaluated for the treatment of human NETs.

Materials and methods

Surrogate preparation and culture

Primary human NETs were obtained after approval by the Institutional Review Board for Human Use of the University of Alabama at Birmingham (UAB) and in accordance with all institutional review board and institutional protocols. After resection, sterile tumor specimens were stored in 1× phosphate buffered saline and placed on ice for transport to the UAB Surgical Pathology Department. After confirmation, first by a surgical pathologist that specimen margins were free of tumor and that sufficient tissue was available for all clinical purposes, tumor specimens were transported on ice to the lab for processing. Human pancreatic NET (pNET) xenografts (BON-1) were obtained by injecting BON-1 cells subcutaneously into Nu/Nu mice and allowing them to grow for 5 weeks before excision. Xenografts and primary human pancreatic NET tissues were passed through a tissue dissociation sieve of 280 μM pore size (Sigma Aldrich, St. Louis, MO) and the cellular components admixed with Bovine Type 1 collagen (Advanced Biomatrix), growth factor reduced Matrigel (Corning, Corning, NY), 10× Dubelco's Modified Eagle Medium (DMEM, Corning), and $NaHCO_3$. This mixture was then injected into a polydimethylsiloxane bioreactor perforated by 2 Teflon-coated wires located within an upstream wire-guide to facilitate the formation of perfusion channels. After polymerization of the tumor surrogate volume, the wires were removed, generating 2 patent channels through the surrogate matrix. The bioreactors were then connected to a micro-peristaltic pump and a media reservoir via peroxide-cured silicone tubing (Cole-Parmer, Vernon Hills, IL) and perfused continuously with 15 mL of growth medium comprised of Phenol Red-Free DMEM/F12 (Corning), 10% FBS (Atlas Biologicals, Ft. Collins, CO), penicillin/streptomycin (Life Technologies, Rockville, MD), and 3% dextran (Sigma Aldrich) during incubation (37°C, 5% CO2), with medium changed every 3 days unless otherwise stated. Surrogate endpoints were defined by physical/mechanical compromise or the absence of detectable cellular activity as determined by fluorophore uptake and retention.

Positron emission tomography (PET)/computed tomography (CT) mice imaging

Immunocompromised male Nu/Nu mice (Jackson Laboratories, Bar Harbor, ME) were injected subcutaneously with BON-1 cells and xenografts developed to a palpable size in 3 weeks. Mice were injected intravenously with 100 μL of 150 to 160 μCi of ^{68}Gallium-DOTATATE and images were collected 1 hour and 2 hours after injection. CT images were collected for 100s after the PET images. The images were reconstructed using commercially available algorithms.

Proliferation, apoptosis, and necrosis assays

Cell viability and proliferation were evaluated using IR-783 as described previously.[11] Apoptosis and necrosis were evaluated using the Realtime-Glo Annexin V Apoptosis and Necrosis Assay. A 20 μM solution of IR-783 was prepared by dilution in phenol red-free DMEM/F12, and the Realtime-Glo Annexin V Apoptosis and Necrosis reagents added to this mixture to 1× concentration per the manufacturer's protocol.[12] This mixture was injected into the perfusion channels and incubated statically for 15 min (37°C, 5% CO2). After incubation, surrogates were perfused for 60 min before imaging in an In Vivo Imaging System (IVIS Lumina; Perkin Elmer, Waltham, MA). Optimized excitation lamp and filter cube settings were used to detect IR-783 (Ex: 780/Em: 845) and the Realtime-Glo Annexin V Necrosis reagent (Ex: 480/Em: 520). Surrogates were incubated as described[11] before each imaging session over the duration of bioreactor growth. Regions of interest were drawn around surrogates to measure radiant efficiency (fluorescence) and photon emission (bioluminescence).

Histologic analysis

Specimens were embedded in paraffin, sectioned, and processed for immunohistochemical staining by the UAB Research Pathology Core. Slides were rehydrated using xylene and ethanol. Antigen retrieval was accomplished by immersing slides in citrate buffer and placing them in a pressure cooker for 10 min. Slides purposed for assessing the retention of NETs in the bioreactors were stained with hematoxylin and eosin. SSTR2 was detected using an anti-SSTR2 antibody (Santa Cruz SSTR2 Antibody (A-8): sc-365502; Santa Cruz Biotechnology, Dallas, TX) at a 1:200 dilution overnight at 4°C and an anti-rabbit biotin labeled secondary antibody (Pierce goat anti-rabbit IgG, #31820). Slides were then stained with DAB chromogen (Dako Liquid DAB+ substrate K3468) and counter stained with hematoxylin.

Statistical analyses

Statistical analyses were performed using IBM SPSS statistics v 25 (IBM Corp, Armonk, NY). Descriptive statistics were summarized using percentages and frequencies for categorical data and means ± standard deviations for continuous data. Data were normally distributed unless otherwise noted. Sample means for growth duration were compared via either a two-way independent-samples *t*-test or a one-way ANOVA where appropriate. Equality of variance was evaluated using Levene's test. Pearson's correlations were used to evaluate the relationship of growth to age and preoperative chromogranin A levels.

Table I
Characteristics of patients and tumor specimens

Age ($N = 27$)*	Percent (frequency)	Mean Growth Duration (d)
53.2 ± 15.5		
Sex ($N = 27$)		
F	37.0 (10)	34.3
M		35.1
Ethnicity ($N = 27$)		
African American	25.9 (7)	36.8
Asian	7.4 (2)	48
Hispanic	3.7 (1)	30
White	63.0 (17)	32.7
Diagnostic pathology ($N = 27$)		
GEP-NET	77.8 (21)	34.3
Paraganglioma	7.4 (2)	18.5
Pulmonary NET	3.7 (1)	31
Medullary thyroid cancer	7.4 (2)	48
Hürthle cell carcinoma	3.7 (1)	55
Site of sample acquisition ($N = 27$)		
GI metastasis	14.8 (4)	34.3
GI/pancreatic	59.3 (16)	35.3
Lung	3.7(1)	31
Retroperitoneum	11.1 (3)	24
Thyroid	11.1 (3)	50.3
Tumor grade ($n = 20$)		
1	33.3 (9)	31.1
2	37 (10)	37.1
3	3.7 (1)	50
SSTR-based imaging ($N = 27$)		
+	37 (10)	34.1
None	63 (17)	35.2
Ki-67 index ($n = 18$)		
<3%	38.9 (7)	35.3
3–20%	38.9 (7)	32.9
>20%	22.2 (4)	44.5
Serum chromogranin A ($n = 15$)*		
112.4 ± 101.5 ng/mL (normal ≤15)		

GI, gastrointestinal.
* Continuous values are summarized as mean ± SD

Results

Growth of human NET surrogates

Twenty-seven human tumor specimens were cultivated as tumor surrogates, including 20 GEP-NETs, 2 medullary thyroid carcinomas, 1 pulmonary carcinoid tumor, 1 thyroid follicular Hürthle cell carcinoma, and 2 paragangliomas (Table I). Of these specimens, 31% were derived from metastatic tissue. As determined by IR-783 fluorescence on IVIS imaging, the mean duration of growth of all specimens was 35 ± 18 days (Fig 1). The mean duration of GEP-NET growth was 35 ± 19 days ($n = 21$), whereas the mean durations of paraganglioma ($n = 2$) and medullary thyroid carcinomas ($n = 2$) growth were 19 and 48, respectively. The durations of growth of the pulmonary NET ($n = 1$) and Hürthle cell carcinoma were 31 days and 55 days, respectively. Of the 10 patients who underwent preoperative SSTR scintigraphy, all were read as positive in the location from which the specimen was resected. There was no difference in the duration of growth of surrogates by tumor grade ($P = .41$), sex ($P = .64$), ethnicity ($P = .86$), Ki-67 index ($P = .85$), or the metastatic nature of the specimen ($P = .92$), nor did growth correlate with patient age. Notably, the distribution of preoperative serum chromogranin A values was positively skewed, hence a valid correlation to growth duration could not be performed.

Treatment of a human cell line xenograft surrogate

A mouse xenograft comprised of BON-1 cells (a human pNET cell line derived from a lymph node metastasis) was processed and cultivated as 2 separate tumor surrogates (Fig 2). To confirm expression of SSTR2 in subcutaneous BON-1 xenografts, scintigraphy with ^{68}Gallium-DOTATATE and PET/CT was performed (Fig 2, *A*). Surrogates originating from these xenografts were treated with 15 ug of ADC or DMSO as control. Compared to control at 72 hours post-treatment, the surrogate treated with ADC exhibited no effect on proliferation as determined by IR-783 (1.6-fold, 1.7-fold increase) but a much greater relative degree of apoptosis (2.1-fold, 0.6-fold), respectively.

Treatment of primary human GEP-NET surrogates

A primary human pNET was resected, and a 350 mg portion of the specimen (Fig 3, *A*) was processed as described in the methods and implanted into 2 separate bioreactors. Expression of SSTR2 was confirmed via immunohistological staining of the original specimen (Fig 3, *B*). After 12 days of growth, each surrogate was propagated into 2 separate bioreactors for a total of 4 tumor surrogates. Baseline measurements of proliferation (Fig 3, *C*), apoptosis (Fig 3, *D*), and necrosis (Fig 3, *E*) were obtained. Two surrogates were then treated with 15 ug of ADC, and 2 with DMSO as control. On day 3, growth media was changed, and surrogates re-treated after imaging. Measurements were acquired at 24-hour intervals over the course of 5 days and compared to measurements acquired at baseline to determine the relative degrees of change in each parameter by surrogate. Compared to controls, surrogates treated with ADC exhibited greater degrees of apoptosis (13.3-fold vs 9.3-fold) and necrosis (2.5-fold vs 1.6-fold). Interestingly, treated

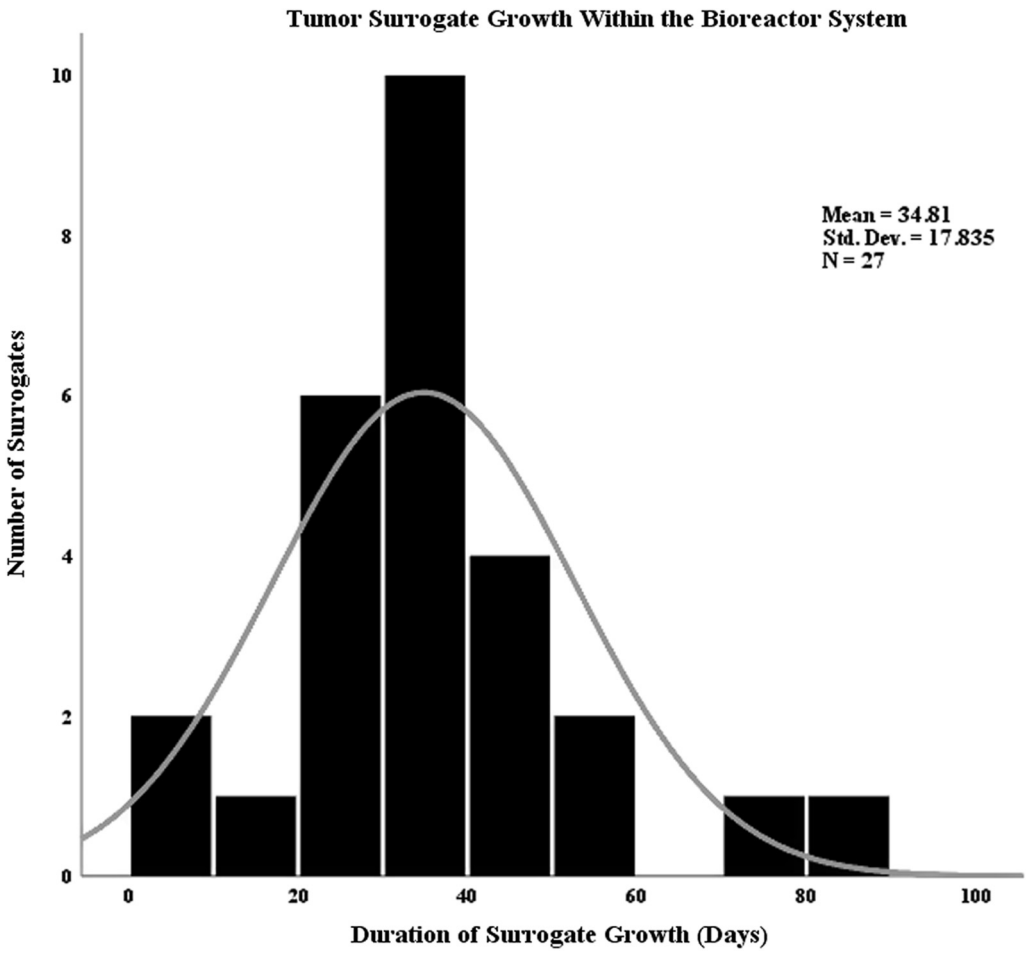

Fig 1. Distribution curve depicting the duration of human tumor surrogate growth within the bioreactor system.

surrogates exhibited similar degrees of proliferation to controls (3-fold vs 2.7-fold; $P = .207$).

Assessment of NET retention in the bioreactor system

A primary human pNET was resected, and a 350 mg portion of the specimen (Fig 4**)** was processed as described in the methods and implanted into 3 separate bioreactors. A portion of the original tumor and 1 surrogate were fixed immediately and embedded in paraffin. The 2 remaining tumor surrogates were cultured for 3 and 9 days, respectively, before being fixed and embedded in paraffin. All paraffin specimens were sectioned and stained with hematoxylin and eosin before imaging of representative sections. These sections illustrated the maintenance of pNET cells within the bioreactor system, as well as similar morphologic qualities to the original tumor.

Discussion

Herein, we have described the ability to cultivate a widely variable array of primary human NET cells, including GEP-NETs, in an ex vivo model for as many as 83 days. Further, we illustrated that an expected cytotoxic response to an SSTR2-targeted, anti-mitotic agent predicated on SSTR2 expression in both human cell line xenograft tissue and primary human NET tissue can be produced using tumor surrogates within this model. This approach introduces the possibility that tumor surrogates in flow-perfusion bioreactor models can be employed to evaluate NETs for a clinical response to targeted therapeutics ex vivo using primary human NET tissue.

The promising utility of targeted therapeutics for NETs has been illustrated by the early successes in their use.[13,14] Specifically, targeting tumor-specific epitopes with ADCs has proven to be a powerful therapeutic strategy.[15,16] ADCs integrate the advantages of monoclonal antibodies capable of specifically binding tumor associated surface receptors with the high cytotoxic potential of small molecule chemotherapeutics. In this study, we used the previously described tubulin polymerization inhibitor MMAE[17,18] as a potent cytotoxic payload conjugated with anti-SSTR2 antibody to kill pNET cells.

Although tumor surrogates grown in this model allow for greater success in cultivating primary human NETs than traditional cell culture or establishing patient-derived xenograft models, they possess a number of distinct advantages and disadvantages. Because NETs are characteristically slow growing, an important utility of the bioreactor system is the ability to detect cytotoxic changes within it. Tumor subtypes with the slowest proliferation rates in vivo may also proliferate slowly in the bioreactor, but the capability of culturing tumor surrogates to ~30 days permits ample time to conduct therapeutic trials similar to those performed herein. Their relatively low throughput does not allow for studies with high statistical power to be conducted on specimens derived from a single patient owing to the amount of tissue required. This disadvantage is as opposed to greater throughput models such as

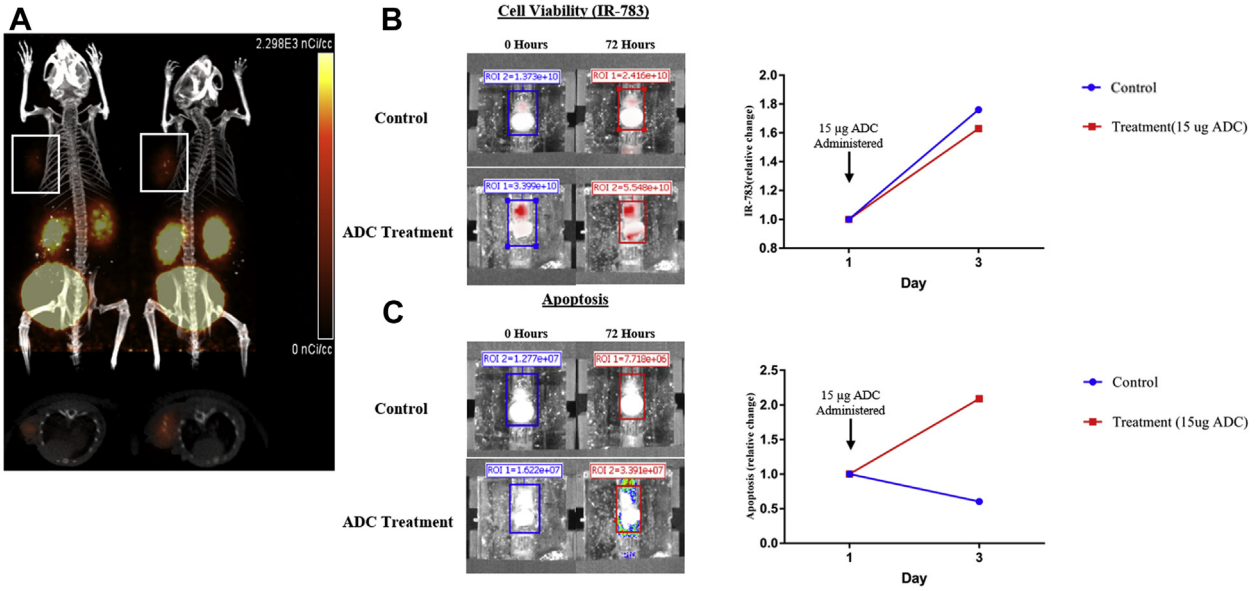

Fig 2. Pancreatic NET (BON-1) cells were injected subcutaneously into Nu/Nu mice and grown for 5 weeks. (*A*) PET/CT images of mice were acquired 1 and 2 hours after injection with [^{68}Ga]-DOTATATE to confirm the expression of SSTR2 in subcutaneous BON-1 mouse xenografts (white boxes). These xenografts were then excised, processed, and implanted into 2 separate bioreactors. The tumor surrogates were imaged at baseline and after 72 hours of culture after incubation with (*B*) 20 uM IR-783 and (*C*) the Promega Realtime-Glo Annexin V Apoptosis reagent. The treatment bioreactor was exposed to 15 µg of ADC after imaging on day 0. (Color version of figure is available online.)

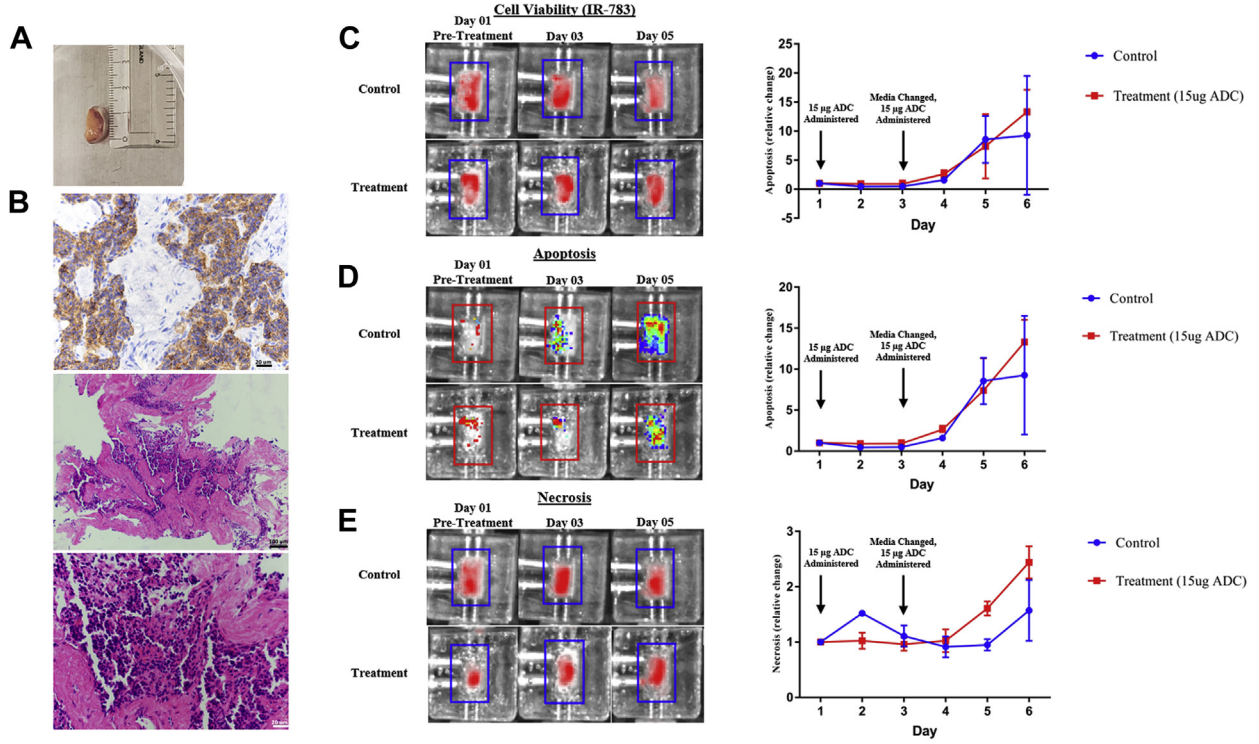

Fig 3. A resected primary human pNET (*A*) was processed and implanted into bioreactors. Sections of this specimen stained positively for SSTR2 on histopathologic examination (*B*). After 12 days of growth, surrogates were propagated to yield 4 separate tumor surrogates. Two surrogates were used as controls, while 2 surrogates were treated with 15 µg of ADC (1 bioreactor from each group is pictured). Images of the surrogates were acquired at baseline and at 24-h intervals for 5 days in an IVIS after daily incubation with 20 µM IR-783 (*B*), and the Promega Realtime-Glo Annexin V Apoptosis (*C*) and Necrosis (*D*) reagent.

organoids, which, if viable for NETs, would allow for more high-powered screening on a broader scale of therapeutics.[19,20] In contrast, an advantage of the bioreactor model lies in the comparatively high rate of success with which primary human NETs can be cultured and the heterogeneity of the cell populations that comprise the surrogates. Whereas current organoid models for NETs lack important components of the tumor stroma, the absence of a cell-sorting process during implantation allows NET cells, endothelia, fibroblasts, immune cells, and other stroma that contribute to the tumor microenvironment to be implanted into the

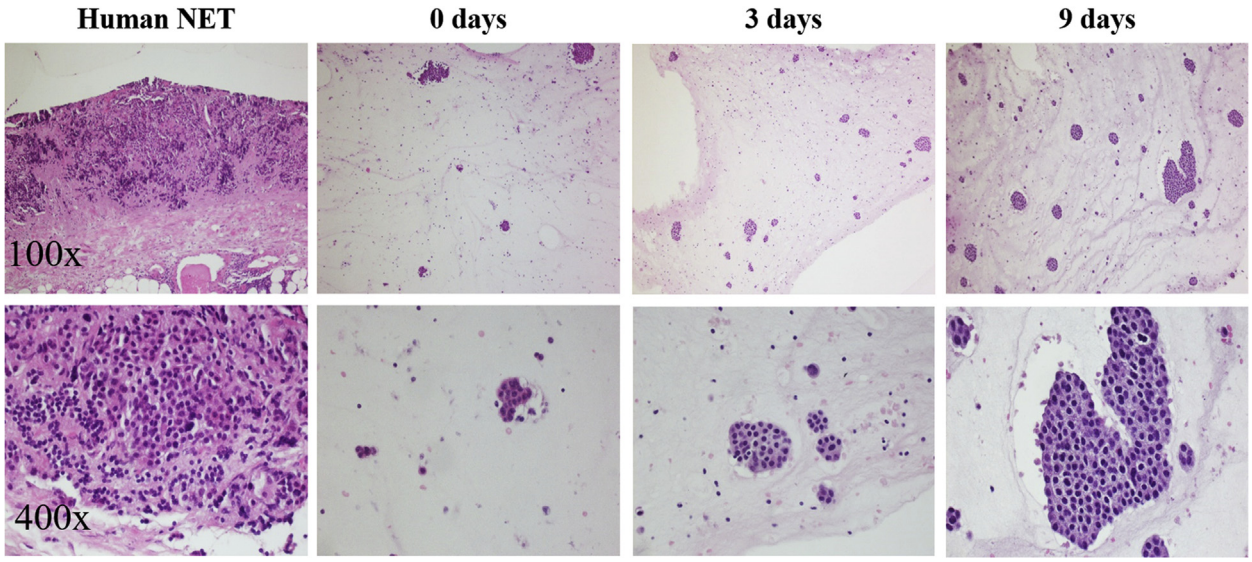

Fig 4. Assessment of NET retention. Histologic sections of surrogates derived from a primary human pNET show characteristic epithelial clustering morphology of pNETs and increasing pNET cell density from 0 to 9 days.

surrogate and arranged into a perfused 3D architecture.[21,22] Previous work with this model and unpublished observations support the retention of this diverse cell population, potentially conferring a phenotype more similar to that expressed by the tumors in vivo than other culture methods, theoretically allowing them to respond to candidate therapeutics in a more physiologically relevant manner.[11]

A key limitation of this study is the low throughput of tumor surrogates on which the ADC was tested and the performance of only the human pNET experiment in duplicate. A further limitation lies in the unclear accuracy of IR-783 uptake as a measurement of tumor viability and proliferation in the context of drug therapy. Although it is normally internalized into cells by members of the organic anion transporter (OAT) superfamily of proteins, unpublished observations suggest that increased membrane permeabilization owing to cellular necrosis during cytotoxic drug therapy may confound the results of these measurements, thereby limiting their utility to studies performed in the absence of therapeutic agents. For example, while administration of the ADC resulted in increased apoptosis and necrosis at day 6 in the human tumor depicted in Fig 2, the proliferation measure of the treated bioreactors increased during the trial. We hypothesize that the high rate of necrosis in the treated bioreactors and resultant increase in membrane permeability allowed the infrared dye used to assess proliferation (IR-783) to enter the cells through means other than the OAT. At the time of necrotic death, the cells would no longer be capable of excreting the dye through OAT and other efflux pumps for lack of ATP. In contrast, there was not a high baseline rate of apoptosis in the bioreactors containing BON-1 xenograft cells. This highlights a key issue in studying NETs; the currently available cell lines harbor a number of mutations absent in primary tumors that have facilitated their adaptation to growing in vitro. A number of these mutations have been identified by Vandamme et al and Hofving et al[23,24] in GEP-NET cell lines. For example, the BON-1 cell line isolated by Evers et al has been in culture for over 20 years and possesses a homozygous loss of CDKN2A and CDKN2B, which are not characteristic mutations in NETs.[25] TP53 encoding a tumor suppressor and key regulator of DNA repair and apoptosis is usually unaffected in GEP-NETs; however, it was found to be bi-allelically inactivated in BON-1 and in QGP-1, another pNET cell line. The genome of BON-1 contains a homozygous stop-loss mutation, whereas the genome of QGP-1 has undergone a frameshift deletion of the gene. Alternatively, these cell lines lack mutations in DAXX or MEN1, which are common in NETs. These uncharacteristic genomic changes may contribute to lesser levels of baseline apoptosis in culture when observing cell line xenografts as compared to primary human tumors. They may also contribute to the difficulty in culturing these primary tumors ex vivo. Hence, although this model allows human tumors to be cultured ex vivo for a greater duration than is observed with traditional culture methods, naturally occurring degrees of apoptosis and necrosis will likely be present within the system in the absence of investigator manipulation.

In conclusion, although these tumor surrogates cannot replace clinical trials for determining pharmacodynamics, pharmacokinetics, or side effects, this model is ideal for the evaluation of targeted therapeutics or the efficacy of FDA-approved pharmacologic agents. Further, they represent a tool that can be used to inform and appropriately alter clinical decision-making during a patient's treatment course to make it optimally effective.

Funding/Support

Research reported in this publication was supported by the UAB Center for Clinical and Translational Sciences TL1 Pre-Doctoral Training Grant under award number TL1TR001418 and North American Neuroendocrine Tumor Society (NANETS) Basic/Translational Science Investigator (BTSI) award.

Conflict of interest/Disclosure

The authors declare no conflict of interest.

Acknowledgements

The authors thank Dr. Kayla Goliwas for her invaluable assistance during the study.

References

1. Dasari A, Shen C, Halperin D, et al. Trends in the incidence, prevalence, and survival outcomes in patients with neuroendocrine tumors in the United States. *JAMA Oncol*. 2017;3:1335–1342.
2. Lee L, Ito T, Jensen RT. Everolimus in the treatment of neuroendocrine tumors: efficacy, side-effects, resistance, and factors affecting its place in the treatment sequence. *Expert Opin Pharmacother*. 2018;19:909–928.
3. Wiedmann MW, Mössner J. Safety and efficacy of sunitinib in patients with unresectable pancreatic neuroendocrine tumors. *Clin Med Insights Oncol*. 2012;6:381–393.
4. Pavel ME, Hainsworth JD, Baudin E, et al. Everolimus plus octreotide long-acting repeatable for the treatment of advanced neuroendocrine tumours associated with carcinoid syndrome (RADIANT-2): a randomised, placebo-controlled, phase 3 study. *The Lancet*. 2011;378:2005–2012.
5. Pavel M, O'Toole D, Costa F, et al. and the Vienna Consensus Conference participants. ENETS consensus guidelines update for the management of distant metastatic disease of intestinal, pancreatic, bronchial neuroendocrine neoplasms (NEN) and NEN of unknown primary site. *Neuroendocrinology*. 2016;103:172–185.
6. Foster DS, Jensen R, Norton JA. Management of liver neuroendocrine tumors in 2018. *JAMA Oncol*. 2018;4:1605–1606.
7. Öberg KE, Reubi JC, Kwekkeboom DJ, Krenning EP. Role of somatostatins in gastroenteropancreatic neuroendocrine tumor development and therapy. *Gastroenterology*. 2010;139:742–753, 753.e1.
8. Beck A, Goetsch L, Dumontet C, Corvaïa N. Strategies and challenges for the next generation of antibody–drug conjugates. *Nat Rev Drug Discov*. 2017;16:315–337.
9. Yang Z, Zhang L, Serra S, et al. Establishment and characterization of a human neuroendocrine tumor xenograft. *Endocr Pathol*. 2016;27:97–103.
10. Grozinsky-Glasberg S, Shimon I, Rubinfeld H. The role of cell lines in the study of neuroendocrine tumors. *Neuroendocrinology*. 2012;96:173–187.
11. Goliwas KF, Richter JR, Pruitt HC, et al. Methods to evaluate cell growth, viability, and response to treatment in a tissue engineered breast cancer model. *Sci Rep*. 2017;7:14167.
12. Kupcho K, Shultz J, Hurst R, et al. A real-time, bioluminescent annexin V assay for the assessment of apoptosis. *Apoptosis*. 2019;24:184–197.
13. Strosberg J, El-Haddad G, Wolin E, et al. and the NETTER-1 Trial Investigators. Phase 3 Trial of ^{177}Lu-Dotatate for midgut neuroendocrine tumors. *N Eng J Med*. 2017;376:125–135.
14. Saunders LR, Bankovich AJ, Anderson WC, et al. A DLL3-targeted antibody-drug conjugate eradicates high-grade pulmonary neuroendocrine tumor-initiating cells in vivo. *Sci Transl Med*. 2015;7:302ra136.
15. Li Z, Wang M, Yao X, et al. Development of a novel EGFR-targeting antibody-drug cfor pancreatic cancer therapy. *Target Oncol*. 2019;14:93–105.
16. D'Amico L, Menzel U, Prummer M, et al. A novel anti-HER2 anthracycline-based antibody-drug conjugate induces adaptive anti-tumor immunity and potentiates PD-1 blockade in breast cancer. *J Immunother Cancer*. 2019;7:16.
17. Yao Y, Wang Y, Zhou S, et al. Preparation and anti-cancer evaluation of promiximab-MMAE, an anti-CD56 antibody drug conjugate, in small cell lung cancer cell line xenograft models. *J Drug Target*. 2018;26:905–912.
18. Cunningham D, Parajuli KR, Zhang C, et al. Monomethyl auristatin e phosphate inhibits human prostate cancer growth. *Prostate*. 2016;76:1420–1430.
19. Crespo M, Vilar E, Tsai S-Y, et al. Colonic organoids derived from human induced pluripotent stem cells for modeling colorectal cancer and drug testing. *Nat Med*. 2017;23:878–884.
20. Broutier L, Mastrogiovanni G, Verstegen MM, et al. Human primary liver cancer-derived organoid cultures for disease modeling and drug screening. *Nat Med*. 2017;23:1424–1435.
21. Kawasaki K, Fujii M, Sato T. Gastroenteropancreatic neuroendocrine neoplasms: genes, therapies and models. *Dis Model Mech*. 2018;11. dmm029595.
22. Pickup MW, Mouw JK, Weaver VM. The extracellular matrix modulates the hallmarks of cancer. *EMBO Rep*. 2014;15:1243–1253.
23. Vandamme T, Beyens M, Peeters M, Van Camp G, de Beeck KO. Next generation exome sequencing of pancreatic neuroendocrine tumor cell lines BON-1 and QGP-1 reveals different lineages. *Cancer Genet*. 2015;208:523.
24. Hofving T, Arvidsson Y, Almobarak B, et al. The neuroendocrine phenotype, genomic profile and therapeutic sensitivity of GEPNET cell lines. *Endocr Relat Cancer*. 2018;25:367–380.
25. Vijayvergia N, Boland PM, Handorf E, et al. Molecular profiling of neuroendocrine malignancies to identify prognostic and therapeutic markers: a Fox Chase Cancer Center Pilot Study. *Br J Cancer*. 2016;115:564–570.

Discussion

Dr James Howe (Iowa City, IA): This is a real advance because, as you mentioned, there are only a couple of cell lines that we can study, and they are 20 to 30 years old. They dedifferentiate, they grow quickly, and they are high grade. So they are not really indicative of most of the tumors that we treat.

One question I have for you is, why the bioreactor chamber? Why is that better than just typical cell culture with Matrigel?

The second question is whether you have tested these things that have grown longer to see if they retain neuroendocrine markers like chromogranin, synaptophysin, and somatostatin?

Dr Brendon Herring: To answer your first question, I think with the flow perfusion, that we are actually pumping and redistributing nutrients constantly within the bioreactor. It is helping them to stay alive and proliferate during the course of culture. We also do know that the 3D architecture and the presence of the tumor stroma that we get in this system (where we are not sorting and selecting for just the cancer cells themselves) helps to establish or convey proliferative signals to the cancer cells themselves. That's why I think they are growing better in this system as opposed to traditional culture.

cancers

MDPI

Article

Pulmonary Carcinoid Surface Receptor Modulation Using Histone Deacetylase Inhibitors

Rachael E. Guenter [1], Tolulope Aweda [2], Danilea M. Carmona Matos [1,3], Jason Whitt [1], Alexander W. Chang [1], Eric Y. Cheng [4], X. Margaret Liu [5], Herbert Chen [1], Suzanne E. Lapi [2] and Renata Jaskula-Sztul [1,*]

1 Department of Surgery, School of Medicine, University of Alabama at Birmingham, Birmingham, AL 35233, USA; rguenter@uab.edu (R.E.G.); danileacm@sanjuanbautista.edu (D.M.C.M.); jwhitt@uabmc.edu (J.W.); awchang@uab.edu (A.W.C.); hchen@uabmc.edu (H.C.)
2 Department of Radiology, University of Alabama at Birmingham, Birmingham, AL 35233, USA; taweda1@uabmc.edu (T.A.); lapi@uab.edu (S.E.L.)
3 San Juan Bautista School of Medicine, Caguas, PR 00726, USA
4 College of Pharmacy, University of North Texas Health Science Center, Fort Worth, TX 76107, USA; eric.cheng@unthsc.edu
5 Department of Biomedical Engineering, University of Alabama at Birmingham, Birmingham, AL 35233, USA; mliu@uab.edu
* Correspondence: rjsztul@uabmc.edu; Tel.: +1-205-975-3507

Received: 1 February 2019; Accepted: 8 May 2019; Published: 3 June 2019

Abstract: Pulmonary carcinoids are a type of neuroendocrine tumor (NET) accounting for 1–2% of lung cancer cases. Currently, Positron Emission Tomography (PET)/CT based on the radiolabeled sugar analogue [^{18}F]-FDG is used to diagnose and stage pulmonary carcinoids, but is suboptimal due to low metabolic activity in these tumors. A new technique for pulmonary carcinoid imaging, using PET/CT with radiolabeled somatostatin analogs that specifically target somatostatin receptor subtype 2 (SSTR2), is becoming more standard, as many tumors overexpress SSTR2. However, pulmonary carcinoid patients with diminished SSTR2 expression are not eligible for this imaging or any type of SSTR2-specific treatment. We have found that histone deacetylase (HDAC) inhibitors can upregulate the expression of SSTR2 in pulmonary carcinoid cell lines. In this study, we used a non-cytotoxic dose of HDAC inhibitors to induce pulmonary carcinoid SSTR2 expression in which we confirmed in vitro and in vivo. A non-cytotoxic dose of the HDAC inhibitors: thailandepsin A (TDP-A), romidepsin (FK228), suberoylanilide hydroxamic acid (SAHA), AB3, and valproic acid (VPA) were administered to promote SSTR2 expression in pulmonary carcinoid cell lines and xenografts. This SSTR2 upregulation technique using HDAC inhibitors could enhance radiolabeled somatostatin analog-based imaging and the development of potential targeted treatments for pulmonary carcinoid patients with marginal or diminished SSTR2 expression.

Keywords: somatostatin receptor; histone deacetylase inhibitor; neuroendocrine cancer; pulmonary carcinoid

1. Introduction

The leading cause of cancer-related deaths worldwide is currently attributed to lung cancer, with pulmonary carcinoids accounting for 1–2% of all cases [1]. Pulmonary carcinoids are a type of neuroendocrine tumor (NET) with a five-year survival rate ranging from 40–90% [2]. Classification includes low-grade typical carcinoids (TC), intermediate grade atypical carcinoids (AC), and a rare pre-invasive carcinoid lesion known as diffuse idiopathic NE cell hyperplasia (DIPNECH) [1]. Positron Emission Tomography (PET)/CT using the radiolabeled sugar analogue [^{18}F]FDG is used to diagnose

and stage high grade, poorly-differentiated carcinoids such as ACs, but is suboptimal due to low metabolic activity in these tumors [3].

More recently, NET imaging using PET/CT with radiolabeled somatostatin analogs that specifically target somatostatin receptor subtype 2 (SSTR2) is becoming more standard as many NETs overexpress SSTR2 [4–7]. Indigenously, somatostatin is an anti-cancer neuropeptide, which is associated with the prevention of hormone and growth factor secretions that contribute to tumor growth, inhibition of tumor cell proliferation, and the induction of apoptosis mediated by the five different SST receptor subtypes (SSTR1-5) [8,9]. Clinically used somatostatin analogs have high affinities towards SSTR2, in addition to weaker affinities to SSTR3 and SSTR5 [10]. Most prominently, [^{68}Ga]DOTATATE binds to SSTR2 with an order of magnitude higher in affinity than other [^{68}Ga]-DOTA-peptides [10–12]. This suggests that a higher incidence and density of SSTR2 would be beneficial for imaging and treating patients [8]. However, only 34% TC, 71% of metastatic TC and 51% of AC showed a strong membrane presence of SSTR2. As the majority of pulmonary carcinoid patients have low or undetectable SSTR2 expression, the targeting might be inconsistent and peptide receptor radiotherapy (PRRT) can be limited only to patients with high level of SSTR2 [13]. Ultimately, well-differentiated, typical carcinoids (TC) can be imaged using PET/CT with radiotracers that target SSTR2, but poorly-differentiated, atypical carcinoids (AC) are only eligible for PET/CT using [^{18}F]FDG, a technique shown to be insufficient for detection [14–16].

We have found that histone deacetylase (HDAC) inhibitors can increase the expression of SSTR2 in pulmonary carcinoid cell lines. Specifically, we have tested the FDA approved drugs: romidepsin (FK228), suberoylanilide hydroxamic acid (SAHA), valproic acid (VPA), in addition to a non-FDA approved analog of SAHA named AB3 and thailandepsin A (TDP-A), a naturally derived HDAC inhibitor isolated from the bacteria *Burkholderia thailandensis* E264 found in Thai rice fields [17,18]. Previous studies show that TDP-A has an anti-proliferative effect in various cancer cell lines at nanomolar concentrations and more specifically this compound may be a therapeutic agent against NETs by activating the Notch pathway [19–22].

This study was designed to test our hypothesis that the HDAC inhibitors can increase the presence of SSTR2 on the surface of pulmonary carcinoid cells to potentially improve SSTR2-based imaging and therapies. We performed in vitro studies and small animal PET/CT with [^{68}Ga]DOTATATE to characterize alterations in SSTR2 expression after treatment HDAC-inhibiting compounds.

2. Results

2.1. Transcriptional and Translational Induction of SSTR2

In vitro studies showed the upregulation of SSTR2 at the protein and mRNA level following treatment with HDAC inhibiting compounds. We measured the basal protein expression level of SSTR2 in human fibroblast cells (917 and WI38 cells), aggressive thyroid cancer cell lines (TPC, FTC236, and Hth7), and in various NET cell lines (medullary thyroid cancer: TT and MZ cells, pancreatic NE cancer: BON-1, and pulmonary carcinoid: H727) (Figure 1). The pulmonary carcinoid cell line H727 had the lowest basal expression of SSTR2 among all NET cells (Figure 1A, Figure S1). Relative to the loading control, the ratio of SSTR2 protein expression in H727 was 0.26, compared to 0.79 in TT, 2.21 in MZ-CRC-1, 0.54 in BON-1, 1.09 in Hth7, 0.82 in FTC236, 0.25 in WI-38 and 0.09 in 917. To compare the basal SSTR2 expression between to widely available pulmonary carcinoid cell lines, we performed a western blot and determined that the average protein expression in UMC-11 was about 68-fold higher than in H727 (Figure 1B, Figure S2). This result suggests that the UMC-11 cell line could represent a patient with a high level of SSTR2 expression and H727 could represent a patient with a minimal level of SSTR2 expression.

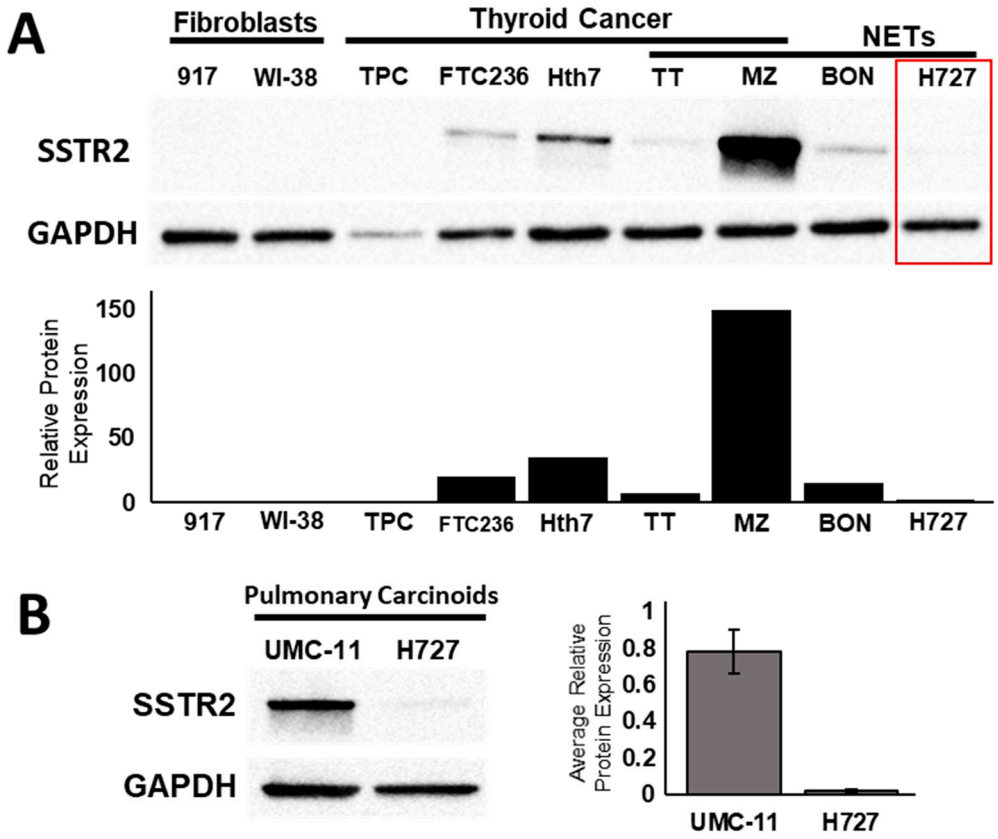

Figure 1. Basal levels of SSTR2 protein expression. (**A**) Basal expression level of SSTR2 in human fibroblast cell lines (917 and WI38), aggressive thyroid cancer cell lines (TPC, FTC236, and Hth7) and in neuroendocrine cancer cell lines (medullary thyroid cancer: TT and MZ; pancreatic NE cancer: BON; pulmonary carcinoid: H727). H727 cell line has the lowest basal expression of SSTR2 among all NET cells (Supplementary Figure S1). (**B**) A comparison of basal SSTR2 expression at the protein level between two pulmonary carcinoid cell lines: UMC-11 and H727 (Supplementary Figure S2). Error bars show standard deviation.

Upon treatment with increasing doses of five separate HDAC inhibitors, there were consistent increases in the expression of SSTR2 messenger RNA (mRNA) in the pulmonary carcinoid cell line H727 (Figure 2). An independent one-way ANOVA revealed a significant effect of treating H727 cells with HDAC inhibiting compounds $F(10) = 14.240$, $p < 0.001$. After administration of FK228, there was a significant increase in relative fold SSTR2 mRNA expression after a 6 nM dose (mean ± SEM, 4.01 ± 0.28, $p = 0.002$), but not a significant increase after a 2 nM dose (mean ± SEM, 1.72 ± 0.45, $p = 0.971$) when compared to a control treatment using DMSO. A similar trend was apparent after treatment with SAHA. There were increases in relative fold SSTR2 mRNA expression, where the increase was determined to be significant after a 3 μM dose of SAHA (mean ± SEM, 3.45 ± 0.46, $p = 0.014$), but not significant after a 1 μM dose of SAHA (mean ± SEM, 1.51 ± 0.44, $p = 0.998$). H727 cells treated with either 1 mM VPA (mean ± SEM, 3.80 ± 0.37, $p = 0.012$) or 4 mM VPA (mean ± SEM, 5.79 ± 0.34, $p < 0.001$) both had a significantly higher relative fold expression of SSTR2 mRNA compared to the DMSO treatment. Moreover, treatment with 2 nM TDP-A (mean ± SEM, 5.31 ± 0.45, $p < 0.001$), 6 nM TDP-A (mean ± SEM, 4.03 ± 0.57, $p = 0.002$), or 3 μM of AB3 (mean ± SEM, 3.43 ± 0.42, $p = 0.037$) showed a significantly higher relative fold inductions of SSTR2 at the mRNA level. A dose of 1 μM AB3 (mean ± SEM, 2.10 ± 0.02, $p = 0.822$) also showed a trend toward increased SSTR2 expression, but this increase was not found to be significant. All relative fold expression values were compared to a DMSO control treatment (mean ± SEM, 1.01 ± 0.12) and normalized to GADPH expression. In summary, transcription of the SSTR2 gene can be significantly increased with a 6 nM dose of FK228, a

3 μM dose of SAHA, both a 1mM and 4mM dose of VPA, both a 2 nM and a 6 nM dose of TDP-A and a 3 μM dose of AB3.

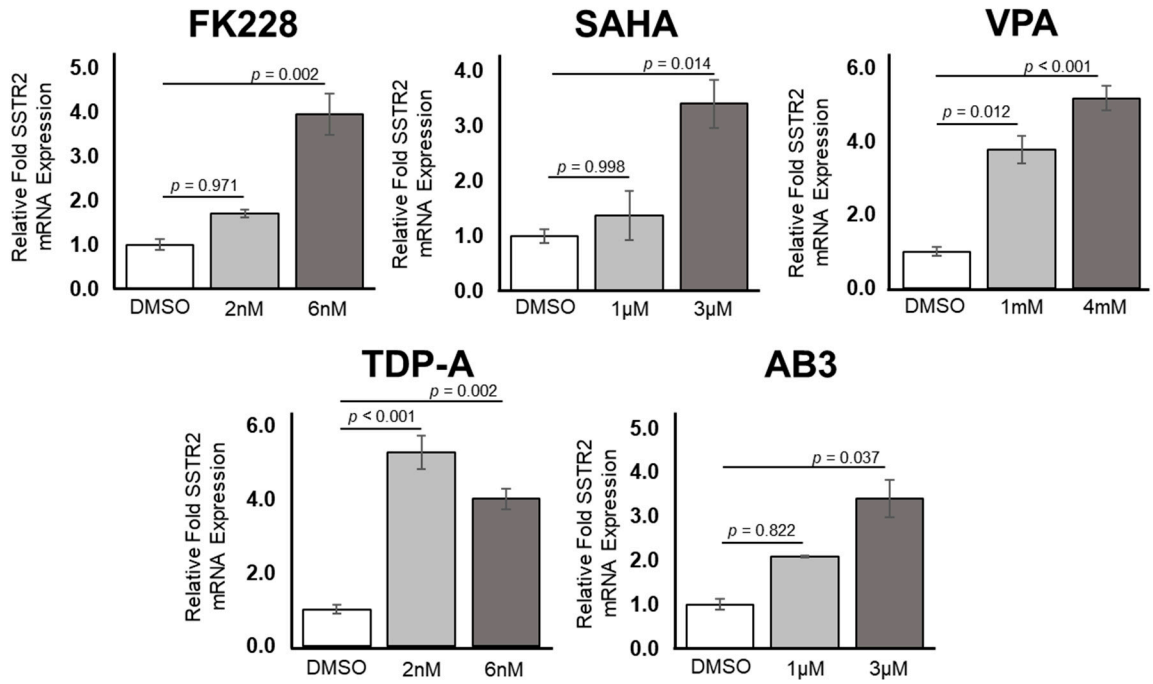

Figure 2. Upregulation of SSTR2 at the transcriptional level in H727, a pulmonary carcinoid cell line. Using two concentrations of five different histone deacetylase (HDAC) inhibitors, there is an increase in SSTR2 mRNA expression. There was a statistically significant increase after treatment with 6 nM romidepsin (FK228), 3 μM suberoylanilide hydroxamic acid (SAHA), 1 mM and 4 mM valproic acid (VPA), 2 nM and 6 nM thailandepsin A (TDP-A) and 3 μM AB3.

To further investigate the ability of HDAC inhibitors to induce SSTR2 expression in pulmonary carcinoids in vitro, we assessed changes in the amount of SSTR2 protein after treatment (Figure 3, Figure S3). In agreement with the transcription level results, western blotting revealed increases in SSTR2 protein expression after treatment with increasing doses of five different HDAC inhibitors in the H727 cell line (Figure 3A, Figure S3A). Administration of 6 nM FK228 induced the highest relative fold expression of SSTR2 when compared to GAPDH expression. Each concentration of HDAC inhibitor-induced SSTR2 expression by at least 2.5-fold in the H727 cell line. However, there was a minimal increase of 1.8-fold in SSTR2 protein expression in the other pulmonary carcinoid cell line UMC-11, which had high basal expression (Figure 3A, Figure S3B). As a comparison to other NET cell lines, the effect of HDAC inhibitor treatment on SSTR2 protein incidence was also determined in medullary thyroid cancer cell lines: TT and MZ (Figure 3A, Figure S3C,D). Interestingly, a similar trend to the pulmonary carcinoid cell lines was observed. The TT cell line, with medium SSTR2 basal protein expression, showed increases in SSTR2 expression after treatment up to 3-fold, but the MZ cell line, with high basal SSTR2 expression, had only a maximum of 1.2-fold increase in the amount of detectable SSTR2 protein expression (Figure 3A, Figure S3D). To test to cell membrane presence of the observed SSTR2 overexpression, H727 cell surface proteins were isolated and probed for SSTR2 via western blot (Figure 3C, Figure S4). As shown in Figure 3C, treatment with 2 nM TDP-A, 6 nM TDP-A, 1 mM VPA, and 4 mM VPA all showed detectable increases in cell surface SSTR2 expression by at least 50%.

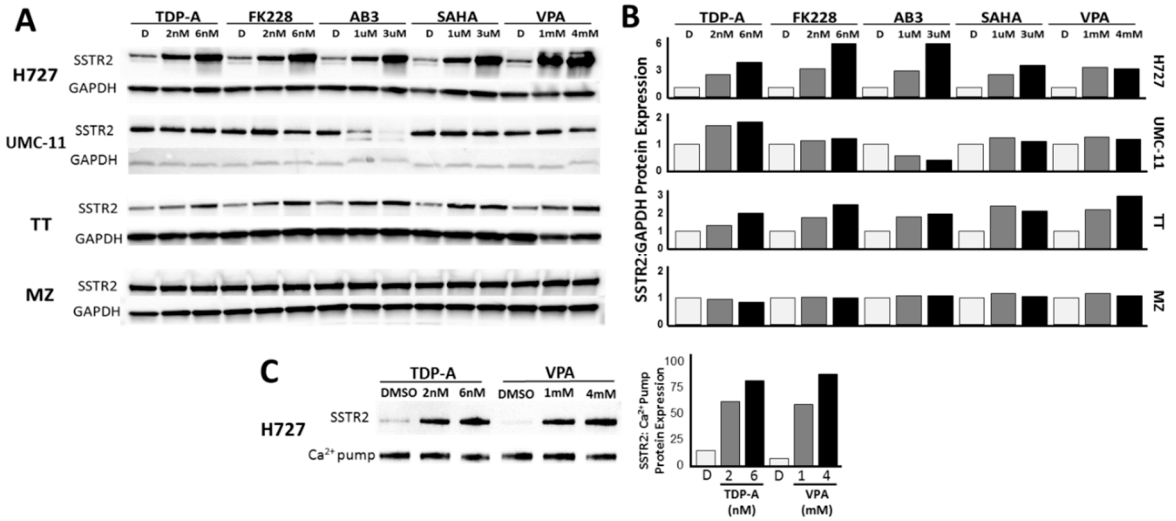

Figure 3. Increase in SSTR2 protein expression. (**A**) Upregulation of SSTR2 expression in NET cell lines by HDAC inhibitor treatment. The pulmonary carcinoid cell line, H727, showed the highest fold induction of SSTR2 (Supplementary Figure S3). (**B**) Ratio of SSTR2 protein expression relative to GADPH protein expression in NET cell lines after incubation with HDAC inhibitors (**C**) Upregulation of SSTR2 expression in the cell surface proteins of pulmonary carcinoid cell line H727 after TDP-A and VPA administration (Supplementary Figure S4).

2.2. Detection of Functional SSTR2 Expression in Pulmonary Carcinoids

Fluorescence-activated cell sorting (FACS) of the pulmonary carcinoid cell line H727 in comparison to the papillary thyroid cancer cell line (TPC) confirmed the functional overexpression of SSTR2 expression after HDAC inhibitor treatment (Figure 4). There was a statistically significant difference between the H727 cells treated with DMSO as a control and a 6 nM dose of TDP-A as determined by one-way ANOVA $F(2,6) = 9.959$, $p = 0.012$. A Bonferroni post hoc test revealed that the H727 cells treated with 6 nM TDP-A (mean ± SEM, 43.53 ± 3.96, $p = 0.013$) resulted in a significantly higher percentage of cells expressing SSTR2 on the cell surface compared to the control (DMSO) treatment (mean ± SEM, 31.27 ± 2.51). There was no significant difference between the control (DMSO) treatment and the 2 nM TDP-A treatment (mean ± SEM, 37.6 ± 3.47). Interestingly, the UMC-11 cell line showed lower overall expression of cell surface SSTR2 compared to H727, but still had a significant increase in the percentage of cells with detectable SSTR2 expression $F(2) = 10.904$, $p = 0.010$. Specifically, UMC-11 cells treated with either 2 nM TDP-A (mean ± SEM, 8.16 ± 0.86) or 6 nM TDP-A (mean ± SEM, 12.1 ± 0.85) both had a significantly greater amount of cells expressing SSTR2 compared to cells treated with DMSO as a control. In the non-neuroendocrine cancer cell line (TPC), there was not a significant difference in cells treated with either control (DMSO) or 2 nM TDP-A, $t(4) = 0.546$, $p = 0.614$ as determined by a one-way ANOVA. The 6 nM dose of TDP-A was highly cytotoxic to TPC cells and therefore no viable cells were available for analysis.

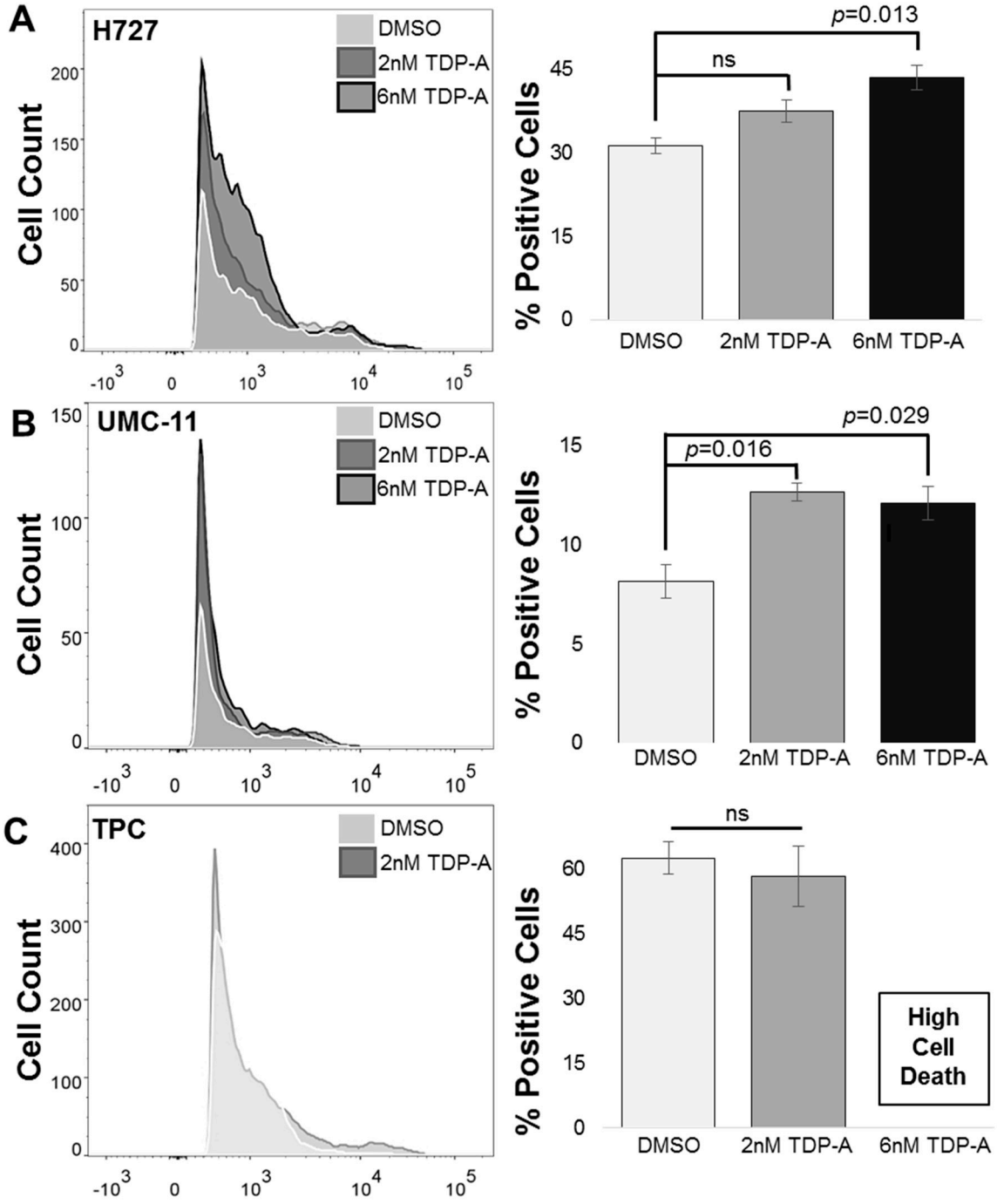

Figure 4. Increase in surface SSTR2 incidence. (**A**) The pulmonary carcinoid cell line H727 showed a significant increase in the percentage of cells expressing SSTR2 after being administered 6 nM of TDP-A (**B**) UMC-11, another pulmonary carcinoid cell line, showed significant increases in the percentage of SSTR2-positive cells after receiving either 2 nM or 6 nM of TDP-A (**C**) A papillary thyroid carcinoma cell line, TPC, did not show any change in SSTR2 expression after TDP-A administration. ns: not significant.

2.3. Cell Uptake of [^{68}Ga]DOTATATE PET/CT In Vitro

A 48 h treatment with TDP-A had a significant effect on the uptake of [^{68}Ga]DOTATATE in H727 cells, as determined by a one-way ANOVA, $F(5) = 116.267$, $p < 0.001$ (Figure 5A). H727 cells treated with 2 nM TDP-A (mean ± SEM, 14.33 ± 0.74) had a significantly higher percentage of [^{68}Ga]DOTATATE uptake than cells left untreated (mean ± SEM, 2.13 ± 0.14, $p < 0.001$) or treated with DMSO as a control (mean ± SEM, 2.04 ± 0.24, $p < 0.001$). Likewise, H727 cells treated with 6 nM TDP-A (mean ± SEM,

18.91 ± 1.43, $p < 0.001$) had a significantly higher percentage of [^{68}Ga]DOTATATE uptake than cells left untreated (mean ± SEM, 2.13 ± 0.14, $p < 0.001$) or treated with DMSO as a control (mean ± SEM, 2.04 ± 0.24, $p < 0.001$). Furthermore, the uptake was significantly higher in cells treated with 6 nM TDP-A than 2 nM TDP-A. Moreover, the percentage of [^{68}Ga]DOTATATE uptake was measured when unlabeled octreotide peptide was added to block SSTR2 to test for non-specific binding in the population of cells that received either 2 nM or 6 nM TDP-A. In this experiment, the percentage of [^{68}Ga]DOTATATE uptake was significantly reduced in cells treated with 2 nM TDP-A + block (mean ± SEM, 2.31 ± 0.17, $p < 0.001$) and cells treated with 6 nM TDP-A + block (mean ± SEM, 3.03 ± 0.35, $p < 0.001$) in comparison to the cells treated with the corresponding dose of TDP-A that not did receive the unlabeled octreotide peptide. The increase in the uptake of [^{68}Ga]DOTATATE in cells treated with TDP-A was completely reduced when the unlabeled octreotide peptide was present. Therefore, this result indicates that the detected increase in [^{68}Ga]DOTATATE uptake likely resulted from a higher density of SSTR2 on the cell surfaces. Additionally, a western blot was performed to verify that the expression of SSTR2 can be increased in H727 cells after a 24 h treatment with TDP-A (Figure 5B, Figure S5). The results show that after 24 h, SSTR2 expression increased nearly 3-fold after treatment with 2 nM TDP-A and approximately 12.5-fold after treatment with 6 nM TDP-A. This data supports the conclusion that the observed increase in the uptake of [^{68}Ga]DOTATATE in H727 cells results from a greater incidence of SSTR2.

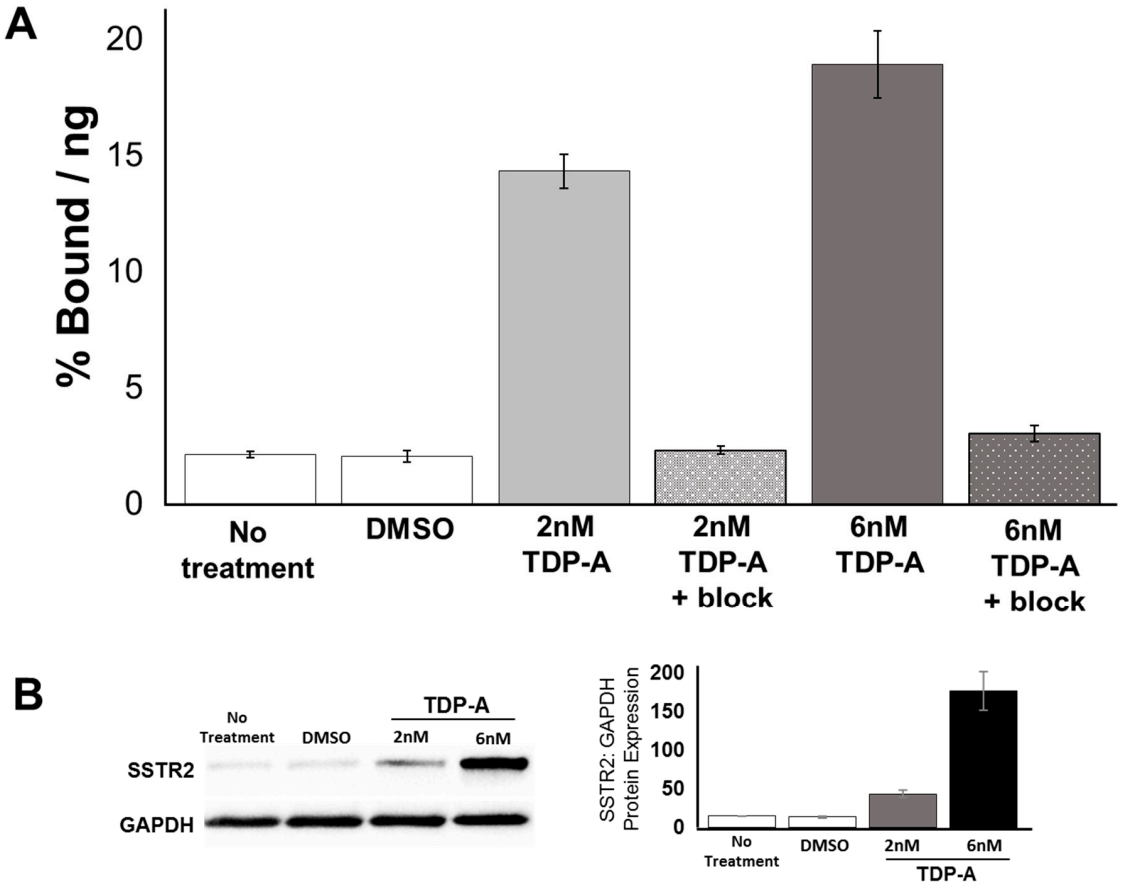

Figure 5. [^{68}Ga]DOTATATE uptake in H727 cells treated with the HDAC inhibitor TDP-A. (**A**) The in vitro uptake of [^{68}Ga]DOTATATE was significantly greater in H727 cells treated with either 2 nM or 6 nM of TDP-A for 48 h in comparison to non-treated cells and cells treated with DMSO as a control. Additionally, an unlabeled octreotide peptide was added to block the SSTR2 and showed no non-specific binding. (**B**) Western blot results with protein quantification data verifying an increase in SSTR2 expression after 24 h of treatment with both 2 nM and 6 nM TDP-A (Supplementary Figure S5).

2.4. [^{68}Ga]DOTATATE PET/CT Small Animal Imaging

Mice bearing pulmonary carcinoid xenografts (H727) demonstrated improved [^{68}Ga]DOTATATE binding after HDAC inhibitor administration when imaged using PET/CT (Figure 6). Mice given the vehicle control treatment showed a minimal increase in [^{68}Ga]DOTATATE binding (Figure 6A,B). However, mice treated with TDP-A displayed an evident increase in [^{68}Ga]DOTATATE binding (Figure 6C,D). The mice that received HDAC inhibitor administration had an average increase in the standard uptake value (SUV) of 2.31 ± 0.73 (mean ± SEM) at 30 min post-[^{68}Ga]DOTATATE injection and 1.84 ± 0.52 (mean ± SEM) at 90 min post-[^{68}Ga]DOTATATE injection. On the other hand, the vehicle-treated group had average SUV change of only 0.96 ± 0.10 (mean ± SEM) at 30 min post-[^{68}Ga]DOTATATE injection and 1.14 ± 0.25 (mean ± SEM) at 90 min post-[^{68}Ga]DOTATATE injection, indicating improved detection of pulmonary carcinoid subcutaneous xenografts. There was no statistical difference between the absolute uptake values likely due to the disparity in the individual mouse tumor uptake and tumor sizes.

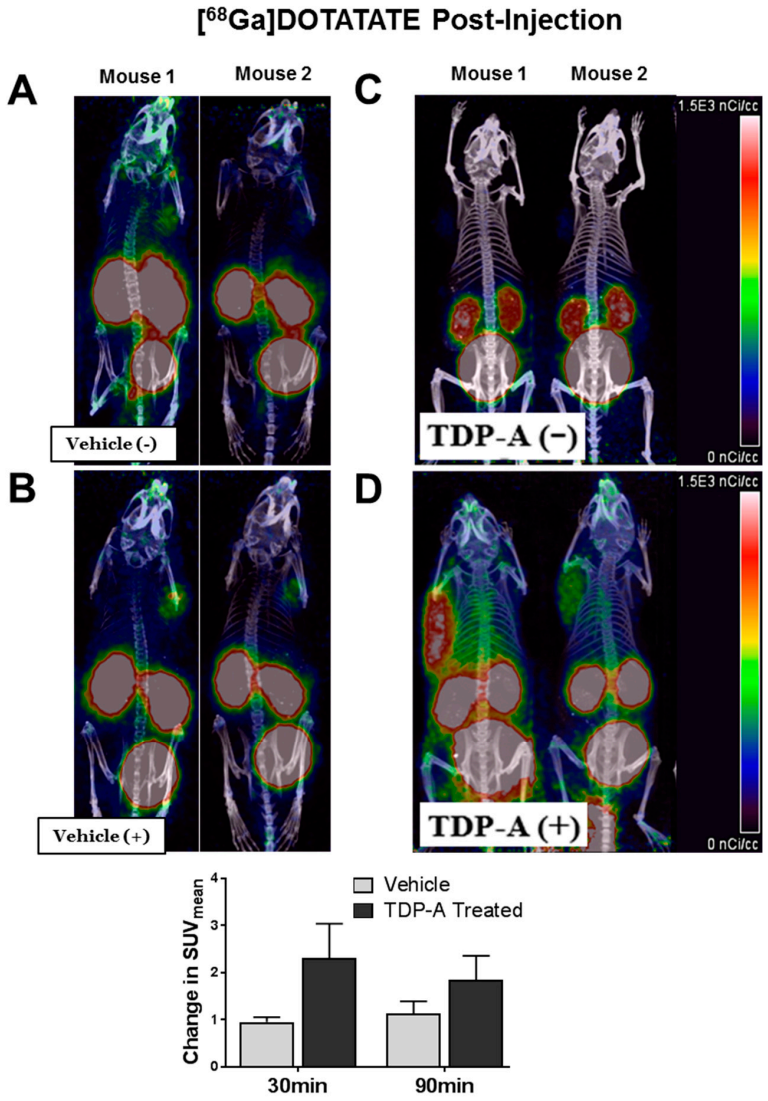

Figure 6. Mice bearing pulmonary NET xenografts and pretreated with TDP-A (+) demonstrated improved [^{68}Ga]DOTATATE binding. (**A**) Two mice were imaged 30 min after [^{68}Ga]DOTATATE administration before control treatment (Vehicle (−)) and then imaged again (**B**) 21.5 h after control treatment (Vehicle (+)). (**C**) Four mice were imaged 30 min after [^{68}Ga]DOTATATE administration before TDP-A(−) treatment and then imaged again (**D**) 21.5 h after TDP-A(+) treatment.

3. Discussion

In this study, we have illustrated that treating pulmonary carcinoids with five different HDAC inhibitors can result in the overexpression of the targetable surface receptor SSTR2. Pulmonary carcinoids reportedly have variable SSTR2 expression, with a SSTR2A subtype frequency of 72% [13,23], making these tumors particularly difficult to image and treat using common NET-specific techniques such as PET/CT with radiolabeled somatostatin analogs that specifically bind to SSTR2. Consequently, these patients would greatly benefit from a technique that could help identify and track previously undetectable primary and metastatic pulmonary carcinoids. In turn, such advancement would not only create a more comprehensive picture of the disease in a patient, but also establish a protocol for more precise imaging and targeted therapies [24].

Our approach to improve pulmonary carcinoid detection was centralized around the methodology that standard and widely accepted techniques for NET imaging and treatment could be improved to increase overall efficacy. In this study, we used HDAC inhibitors to drive an increase in SSTR2 incidence and density. Traditionally, the HDAC protein family plays a key role in the regulation of the cell cycle, cell differentiation, apoptosis, migration and invasion, and angiogenesis by increasing histone acetylation; while HDAC inhibitors can nonselectively inhibit all or multiple members in the family to produce an anti-cancer effect in various cancers including NETs [18–22]. This study suggests that HDAC inhibitors may have an additional theranostic property in pulmonary carcinoids by increasing SSTR2 expression. As previously reported, there is evidence that the interaction of somatostatin and its' analogs with somatostatin receptors has an antiproliferative action and can induce apoptosis, in addition to inhibiting tumorigenic hormone and growth factor secretion [8,9]. Furthermore, there is evidence that patients with low tumor SSTR expression have poor prognoses [15,25,26]. Therefore, one would expect that an increase in SSTR2 could improve patient outcome from a molecular level. However, one study challenges this idea through their finding that SSTR expression was not associated with overall or event-free survival in a study consisting of 102 patients with lung carcinoids [27].

Herein, we tested three FDA approved and two non-FDA approved HDAC inhibitory compounds. Our in vitro studies showed that TDP-A, a naturally derived but non-FDA approved compound was capable of increasing the expression of SSTR2 at the protein and mRNA level. Using small animal PET/CT imaging with [^{68}Ga]DOTATATE, the administration of TDP-A increased tumor uptake and tumor-to-background ratio and thereby converted almost undetectable H727 xenografts into detectable tumors. To the author's knowledge, there is no data available regarding the clinical dosing of TDP-A as it not FDA approved. For the in vivo study, a single dose of TDP-A was administered at the maximum tolerated dose (MTD) of 12.5 mg/kg, as previously tested in mice. The same study shows a therapeutic effect of TDP-A when mice received five intravenous injections every 4 days of the MTD [28]. However, the study described herein does not aim for a therapeutic effect, but instead a non-toxic dose to increase SSTR2 expression.

Moreover, a higher incidence of SSTR2 would localize radiolabeled analog binding while increasing uptake to ameliorate nuclear medicine approaches to NET imaging and therapy. This method is particularly advantageous to patients with pulmonary carcinoids because these tumors often have variable SSTR2 expression [23,29], in which we observed both in vitro and in vivo.

These results could be translatable to a clinical setting because four HDAC inhibitors are currently FDA approved [30] and radiolabeled somatostatin analog-based NET imaging is standardized and FDA-approved for pulmonary carcinoids. The administration of a HDAC inhibiting drug could increase SSTR2 incidence to allow for the detection of hidden primary and metastatic nodules with minimal SSTR2 expression, benefiting patients who have failed or are ineligible for current technologies.

Our approach could be improved as it was limited by the use of only two pulmonary carcinoid lines and five HDAC inhibitors. Universally, there is a limited amount of neuroendocrine cancer models, especially pulmonary carcinoids, available for study. It would be advantageous to screen more HDAC inhibitory compounds to expand the availability of drugs for patient administration.

Overall, the use of this methodology for the molecular upregulation of SSTR2 expression could improve target binding for precise imaging of pulmonary carcinoids, which previously have been difficult to image and treat. This technique could be translated to the clinic to benefit patients with marginal or diminished SSTR2 expression with other types of NETs.

4. Materials and Methods

All studies described were reviewed and approved by the Institutional Biosafety Committee at the University of Alabama at Birmingham under the project number 16-203 and the IACUC animal protocol approval code 20244.

4.1. Cell Culture

This study used human fibroblast cells (917 and WI38 cells), aggressive thyroid cancer cell lines (TPC, FTC236 and Hth7), and NET cell lines (medullary thyroid cancer: TT and MZ-CRC-1 cells, pancreatic NE cancer: BON-1, and pulmonary carcinoid: H727 and UMC-11). Cell lines were maintained as previously described (BON-1 [28], MZ-CRC-1 and TT [15], H727 [31], TPC, FTC236, and Hth7 [32]). The pulmonary carcinoid cell line UMC-11 were grown in RPMI 1640 containing glutamine (Invitrogen Life Technologies, Carlsbad, CA, USA) and supplemented with 10% fetal bovine serum, 100 IU/mL penicillin, and 100 µg/mL streptomycin. The lung fibroblast cell line WI-38 was grown in MEM medium (Invitrogen Life Technologies, Carlsbad, CA, USA) containing Earl salts, glutamine, and phenol red, in addition to 10% fetal bovine serum, 1% non-essential amino acids, and 1% sodium pyruvate. 917, a foreskin fibroblast cell line, was grown in MEM medium (Invitrogen Life Technologies, Carlsbad, CA, USA) with 10% fetal bovine serum, 1% non-essential amino acids, sodium bicarbonate, 0.05 M tricine, and 100 IU/mL penicillin, and 100 µg/mL streptomycin. All cells were grown at 37 °C in a humidified atmosphere containing 5% CO2. Cells were treated for either 24 or 48 h with either DMSO as a control or the following concentrations of HDAC inhibitors: 2 nM or 6 nM TDP-A, 2 nM or 6 nM FK228, 1 µM or 3 µM AB3, 1 µM or 3 µM SAHA and 1mM or 4 mM VPA.

4.2. Real Time Quantitative PCR

Total RNA was isolated from the treated cells 24 h after treatment with the HDAC inhibitor or DMSO using a RNeasy Plus Mini kit (Qiagen, Hilden, Germany). RNA concentrations were determined using the NanoDrop 1000 spectrophotometer (Thermo Scientific, Waltham, MA, USA). Complementary DNA was synthesized from 2µg of total RNA using iScript cDNA Synthesis Kit (Bio-Rad, Hercules, CA, USA). The real-time quantitative PCR was performed in triplicate on CFX Connect Real-Time PCR Detection System (Bio-Rad). The PCR primer sequences for: SSTR forward primer: 5'GAG AAG AAG GTC ACC CGA ATG G 3', SSTR reverse primer: 5' TTG TCC TGC TTA CTG TCA CTC CGC 3', GAPDH forward primer: 5' ACC TGC CAA ATA TGA TGA C 3', GAPDH reverse primer: 5' ACC TGG TGC TCA GTG TAG 3'. Target gene expression was normalized to GAPDH and the ΔΔCt method was used to calculate relative gene expression. Error bars show the Standard Error of the Mean (SEM).

4.3. Western Blot Analysis

Basal SSTR2 expression was determined in the cell lines: 917, WI38, TPC, FTC236, Hth7, TT, MZ-CRC-1, BON-1, H727 and UMC-11. Cells were treated with DMSO as a control or with different concentrations of the HDAC inhibitory drugs: 2 nM or 6 nM TDP-a, 2 nM or 6 nM FK228, 1 µM or 3 µM AB3, 1 µM or 3 µM SAHA and 1 mM or 4 mM VPA. After 48 h, cell lysates and cell surface proteins were prepared. The cell surface proteins were isolated using the Pierce Cell Surface Protein Isolation Kit (Thermo Scientific). Lysate protein concentrations were quantified by BCA Protein Assay Kit (Thermo Scientific) and cell surface proteins were quantified by Pierce 660 nm Protein Assay (Thermo Scientific). The protein samples were denatured and then resolved by a 4–15% Criterion TGX gradient gel (Bio-Rad) electrophoresis, transferred onto nitrocellulose membranes (Bio-Rad), blocked in milk (1× PBS, 5% dry skim milk and 0.05% Tween-20) for 1 h at 4 °C, and incubated with anti-SSTR2

primary antibody (SSTR2 antibody (A-8): sc-365502, Santa Cruz, Dallas, TX, USA) with 1:500 dilution overnight at 4 °C. The membrane was then incubated with the secondary antibody (anti-mouse HRP linked antibody 1:1000, Cell Signaling Danvers, MA, USA) for 2 h at room temperature. The protein bands were detected by Luminata Forte Western HRP Substrate (Millipore, Burlington, MA, USA). Expression levels of GAPDH was used as a loading control for lysates and the expression levels of the calcium pump pan-PMCA ATPase (ab2825, Abcam, Cambridge, UK) was used as a loading control for membrane fractions. Protein expression relative to GAPDH as a loading control was quantified using ImageJ software (NIH, Bethesda, MD, USA).

4.4. Flow Cytometry

H727, UMC-11 and TPC cells were treated with either DMSO, 2 nM TDP-A, or 6 nM concentration of TDP-A for 48 h. After treatment, cells were stained for 1 h at 37 °C with an anti-SSTR2 antibody (Cat#MAB4224, Novus Biologicals, Centennial, CO, USA) labeled with Cy5.5 fluorophore (Lumiprobe, Hunt Valley, MD, USA) at a concentration of 1 μg. After staining, cells were resuspended in flow buffer (0.5% BSA in sterile PBS) then run on a flow cytometer (LSRII, BD Biosciences, San Jose, CA, USA) to detect the presence of Cy5.5 signal via Alexa Fluor 700 laser. Each experiment was done in triplicate. Data were analyzed using FlowJo V5.0 (TreeStar, Inc., Ashland, OR, USA).

4.5. In Vitro [^{68}Ga]DOTATATE PET/CT Uptake

An in vitro study was performed to measure changes in [^{68}Ga]DOTATATE uptake between H727 cells left untreated, treated with DMSO as a control, or treated with either 2 nM or 6 nM of the HDAC inhibitor TDP-A. This experiment was performed in two sets of 12-well plates for each condition. Cells were incubated with either DMSO, 2 nM TDP-A, 6 nM TDP-A, or untreated media for 48 h. For measuring radiopeptide uptake, [^{68}Ga]DOTATATE labeled at specific activity of 215 μCi/μg, with a final concentration of 8 μg/mL (5.3 μM, MW = 1502.3 g/mol) was used. The binding study was done in six replicates at 37 °C for 2 h under 5% CO_2 using a peptide chelate concentration of 10 nM. In another set of wells, 40 μM of unlabeled octreotide peptide was added to block SSTR2 to check for non-specific binding. After incubation, the cells were washed three times with ice-cold PBS and lysed with 0.4 M NaOH. The activity associated with the cells was measured using a gamma counter and protein content evaluated using the BCA assay kit. The data is presented as % Bound per ng of protein = activity associated with cells per total activity added per amount of protein in the lysed cells.

4.6. Small Animal [^{68}Ga]-DOTATATE PET/CT Imaging

Immunocompromised male Nu/Nu mice (Jackson Laboratories, Bar Harbor, ME, USA) were subcutaneously injected with H727 cells and xenografts developed to a palpable size in three weeks. Two groups of mice were imaged before (basal images) and after injection of vehicle or TDP-A. Small animal PET images were acquired on a Sophie GNEXT scanner following tail vein injection of 4.3–5.2 MBq (115–140 μCi) of [^{68}Ga]DOTATATE. Static scans were collected at 30 min and 90 min post-injection. A dose of 12.5 mg/kg TDP-A was administered to mice receiving TDP-A treatment while non-treated mice received equal volume of TDP-A dissolution vehicle (10% ethanol, 60% PEG, 30% PBS) after basal small animal PET images were acquired. Then, mice were imaged again 24 h after vehicle or TDP-A injection. PET and CT images were acquired on a Sofie GNEXT PET/CT scanner. The CT images were reconstructed using a Modified Feldkamp Algorithm. The PET images were reconstructed using a 3D-OSEM (Ordered Subset Expectation Maximization) algorithm (24 subsets and 3 iterations), with random, attenuation and decay correction. Regions of interest were drawn and the mean and maximum standard uptake values (SUVs) for tumors were determined using the formula: SUV = [(MBq/mL) × (animal wt. (g))/injected dose (MBq)].

4.7. Statistical Analysis

All statistical analyses were performed using SPSS (IBM Corp. Released 2017. IBM SPSS Statistics for Windows, Version 25.0. Armonk, NY, USA: IBM Corp.). Significance was determined using a one-way ANOVA followed by a Tukey *post hoc* test, unless stated otherwise. Data were normally distributed. All data is expressed as mean ± Standard Error Mean (SEM) unless stated otherwise. Quantitative real-time PCR and flow cytometry experiments were done triplicate. p values < 0.05 were statistically significant.

5. Conclusions

This study describes a potential method of increasing the membranous density of SSTR2 in pulmonary neuroendocrine tumors through the use of HDAC inhibitory compounds. A higher incidence of SSTR2 on the cell membrane could enhance the efficacy of imaging techniques and therapeutics that target SSTR2.

Supplementary Materials: The following are available online at http://www.mdpi.com/2072-6694/11/6/767/s1, Figure S1: Complete western blot image corresponding to Figure 1A showing all bands and molecular weight markers for (A) SSTR2 and (B) GAPDH, which served as a loading control, Figure S2: Complete western blot image corresponding to Figure 1B showing all bands and molecular weight markers for (A) SSTR2 and (B) GAPDH, which served as a loading control, Figure S3: Complete western blot image corresponding to Figure 3A showing all bands and molecular weight markers for SSTR2 (top image) and GAPDH, which served as a loading control (bottom image) for the cell lines: (A) H727 (B) UMC-11 (C) TT (D) MZ, Figure S4: Complete western blot image corresponding to Figure 3C showing all bands and molecular weight markers for (A) SSTR2 and after the membrane was stripped and probed for (B) the calcium ion pump, which served as a loading control, Figure S5: Complete western blot image corresponding to Figure 5B showing all bands and molecular weight markers for (A) SSTR2 and (B) GAPDH, which served as a loading control.

Author Contributions: Conceptualization, R.J.-S., S.E.L., H.C. and X.M.L.; Formal Analysis, R.E.G., A.W.C. and J.W.; Investigation, R.E.G., A.W.C., E.Y.C., and J.W.; Data Curation, R.E.G. and A.W.C.; Writing-Original Draft Preparation, R.E.G.; Writing-Review & Editing, R.E.G., T.A., D.M.C.M., A.W.C., J.W., X.M.L., H.C., S.E.L. and R.J.-S.

Funding: Research reported in this publication was supported by the National Center for Advancing Translational Research of the National Institutes of Health under award number UL1TR001417. The content is solely the responsibility of the authors and does not necessarily represent the official views of the National Institutes of Health. The animal imaging studies were supported through P30CA013148, the UAB Comprehensive Cancer Center's Preclinical Imaging Shared Facility.

Acknowledgments: The authors would like to thank Wayne Howse, Angela Carter, Zeelu Patel, and the UAB Flow Cytometry Core.

Conflicts of Interest: The authors declare no conflict of interest.

References

1. Travis, W.D. Lung tumours with neuroendocrine differentiation. *Eur. J. Cancer* **2009**, *45*, 251–266. [CrossRef]
2. Chen, L.C.; Travis, W.D.; Krug, L.M. Pulmonary neuroendocrine tumors: What (little) do we know? *J. Natl. Compr. Cancer Netw.* **2006**, *4*, 623–630. [CrossRef]
3. Lim, E. Surigical management of bronchopulmonary and thymic neuroendocrine tumours. Gastroenteropancreatic and thoracic neuroendocrine tumors. *BioScienifica* **2011**, 185–189, in print.
4. Caplin, M.E.; Pavel, M.; Ruszniewski, P. Lanreotide in metastatic enteropancreatic neuroendocrine tumors. *N. Engl. J. Med.* **2014**, *371*, 224–233. [CrossRef] [PubMed]
5. Otte, A.; Herrmann, R.; Heppeler, A.; Behe, M.; Jermann, E.; Powell, P.; Maecke, H.R.; Muller, J.; Powell, P. Yttrium-90 DOTATOC: First clinical results. *Eur. J. Nucl. Med.* **1999**, *26*, 1439–1447. [CrossRef] [PubMed]
6. Marincek, N.; Radojewski, P.; Dumont, R.A.; Brunner, P.; Müller-Brand, J.; Maecke, H.R.; Briel, M.; Walter, M.A. Somatostatin receptor-targeted radiopeptide therapy with 90Y-DOTATOC and 177Lu-DOTATOC in progressive meningioma: Long-term results of a phase II clinical trial. *J. Nucl. Med.* **2015**, *56*, 171–176. [CrossRef]
7. Oberg, K. Molecular imaging radiotherapy: Theranostics for personalized patient management of neuroendocrine tumors (NETs). *Theranostics* **2012**, *2*, 448–458. [CrossRef]

8. Karaca, B.; Degirmenci, M.; Ozveren, A.; Atmaca, H.; Bozkurt, E.; Karabulut, B.; Sanli, U.A.; Uslu, R. Docetaxel in combination with octreotide shows synergistic apoptotic effect by increasing SSTR2 and SSTR5 expression levels in prostate and breast cancer cell lines. *Cancer Chemother. Pharmacol.* **2015**, *75*, 1273–1280. [CrossRef]
9. He, Y.; Yuan, X.; Lei, P. The antiproliferative effects of somatostatin receptor subtype 2 in breast cancer cells. *Acta Pharamacol. Sin.* **2009**, *30*, 1053–1059. [CrossRef]
10. Pauwels, E.; Cleeren, F.; Bormans, G.; Deroose, C.M. Somatostatin receptor PET ligands—The next generation for clinical practice. *Am. J. Nucl. Med. Mol. Imaging* **2018**, *8*, 311–331.
11. Reubi, J.C.; Schar, J.C.; Waser, B.; Wenger, S.; Heppeler, A.; Schmitt, J.S.; Macke, H.R. Affinity profiles for human somatostatin receptor subtypes SST1-SST5 of somatostatin radiotracers selected for scintigraphic and radiotherapeutic use. *Eur. J. Nucl. Med.* **2000**, *27*, 273–282. [CrossRef]
12. Wild, D.; Macke, H.R.; Waser, B.; Reubi, J.C.; Ginj, M.; Rasch, H.; Muller-Brand, J.; Hofmann, M. ^{68}Ga-DOTANOC: A first compound for PET imaging with high affinity for somatostatin receptor subtypes 2 and 5. *Eur. J. Nucl. Med. Mol. Imaging* **2005**, *32*, 724. [CrossRef]
13. Righi, L.; Volante, M.; Tavaglione, V.; Billè, A.; Daniele, L.; Angusti, T.; Inzani, F.; Pelosi, G.; Rindi, G.; Papotti, M. Somatostatin receptor tissue distribution in lung neuroendocrine tumours: A clinicopathologic and immunohistochemical study of 218 'clinically aggressive' cases. *Ann. Oncol.* **2010**, *21*, 548–555. [CrossRef] [PubMed]
14. Taelman, V.F.; Radojewski, P.; Marincek, N.; Ben-Shlomo, A.; Grotzky, A.; Olariu, C.; Perren, A.; Stettler, C.; Krause, T.; Meier, L.P.; et al. Upregulation of Key Molecules for Targeted Imaging and Therapy. *J. Nucl. Med.* **2016**, *57*, 1805–1810. [CrossRef]
15. Jaskula-Sztul, R.; Eide, J.; Tesfazghi, S.; Dammalapati, A.; Harrison, A.D.; Yu, M.N.; Scheinebeck, C.; Winston-McPherson, G.; Kupcho, K.R.; Robers, M.B.; et al. Tumor suppressor role of Notch3 in Medullary Thyroid Carcinoma revealed by genetic and pharmacological induction. *Mol. Cancer Ther.* **2015**, *14*, 499–512. [CrossRef] [PubMed]
16. Daniels, C.E.; Lowe, V.J.; Aubry, M.C.; Allen, M.S.; Jett, J.R. The Utility of Fluorodeoxyglucose Positron Emission Tomography in the Evaluation of Carcinoid Tumors Presenting as Pulmonary Nodules. *Chest* **2006**, *131*, 255–260. [CrossRef] [PubMed]
17. Wang, C.; Henkes, L.M.; Doughty, L.B.; He, M.; Wang, D.; Meyer-Almes, F.J.; Cheng, Y.Q. Thailandepsins: Bacterial products with potent histone deacetylase inhibitory activities and broad-spectrum antiproliferative activities. *J. Nat. Prod.* **2011**, *74*, 2031–2038. [CrossRef] [PubMed]
18. Wang, C.; Cheng, Y.Q. Thailandepsin A. *Acta Crystallogr. Sect. E Struct. Rep. Online* **2011**, *67*, o2948–o2949. [CrossRef]
19. Xiao, K.; Li, Y.P.; Wang, C.; Ahmad, S.; Vu, M.; Kuma, K.; Cheng, Y.Q.; Lam, K.S. Disulfide cross-linked micelles of novel HDAC inhibitor thailandepsin A for the treatment of breast cancer. *Biomaterials* **2015**, *67*, 183–193. [CrossRef]
20. Weinlander, E.; Somnay, Y.; Harrison, A.D.; Wang, C.; Cheng, Y.Q.; Jaskula-Sztul, R.; Yu, X.M.; Chen, H. The novel histone deacetylase inhibitor thailandepsin A inhibits anaplastic thyroid cancer growth. *J. Surg. Res.* **2014**, *190*, 191–197. [CrossRef]
21. Wilson, A.J.; Cheng, Y.Q.; Khabele, D. Thailandepsins are new small molecule class I HDAC inhibitors with potent cytotoxic activity in ovarian cancer cells: A preclinical study of epigenetic ovarian cancer therapy. *J. Ovarian Res.* **2012**, *5*, 12. [CrossRef]
22. Jang, S.; Janssen, A.; Aburjania, Z.; Robers, M.B.; Harrison, A.; Dammalapati, A.; Cheng, Y.Q.; Chen, H.; Jaskula-Sztul, R. Histone deacetylase inhibitor thailandepsin-A activates Notch signaling and suppresses neuroendocrine cancer cell growth in vivo. *Oncotarget* **2017**, *8*, 70828–70840. [CrossRef] [PubMed]
23. Kanakis, G.; Grimelius, L.; Spathis, A.; Tringidou, R.; Rassidakis, G.Z.; Öberg, K.; Kaltsas, G.; Tsolakis, A.V. Expression of Somatostatin Receptors 1-5 and Dopamine Receptor 2 in Lung Carcinoids: Implications for a Therapeutic Role. *Neuroendocrinology* **2015**, *101*, 211–222. [CrossRef]
24. Reubi, J.C.; Waser, B. Triple-Peptide Receptor Targeting In Vitro Allows Detection of All Tested Gut and Bronchial NETs. *J. Nucl. Med.* **2015**, *56*, 613–615. [CrossRef] [PubMed]
25. Abel, F.; Ejeskar, K.; Kogner, P.; Martinsson, T. Gain of chromosome arm 17q is associated with unfavourable prognosis in neuroblastoma, but does not involve mutations in the somatostatin receptor 2 (SSTR2) gene at 17q24. *Br. J. Cancer* **1999**, *81*, 1402–1409. [CrossRef] [PubMed]

26. Daskalakis, K.; Kaltsas, G.; Öberg, K.; Tsolakis, A.V. Lung Carcinoids: Long-Term Surgical Results and the Lack of Prognostic Value of Somatostatin Receptors and Other Novel Immunohistochemical Markers. *Neuroendocrinology* **2018**, *107*, 355–365. [CrossRef] [PubMed]
27. Sestini, R.; Orlando, C.; Peri, A.; Tricarico, C.; Pazzagli, M.; Serio, M.; Pagani, A.; Bussolati, G.; Granchi, S.; Maggi, M. Quantitation of somatostatin receptor type 2 gene expression in neuroblastoma cell lines and primary tumors using competitive reverse transcription-polymerase chain reaction. *Clin. Cancer Res.* **1996**, *2*, 1757–1765. [PubMed]
28. Jaskula-Sztul, R.; Xu, W.; Chen, G.; Harrison, A.; Dammalapati, A.; Nair, R.; Cheng, Y.; Gong, S.; Chen, H. Thailandepsin A-loaded and octreotide-functionalized unimolecular micelles for targeted neuroendocrine cancer therapy. *Biomaterials* **2016**, *91*, 1–10. [CrossRef]
29. Tirosh, A.; Kebebew, E. The utility of ^{68}Ga-DOTATATE positron-emission tomography/computed tomography in the diagnosis, management, follow-up and prognosis of neuroendocrine tumors. *Future Oncol.* **2018**, *14*, 111–122. [CrossRef]
30. Yoon, S.; Eom, G.H. HDAC and HDAC inhibitor: From cancer to cardiovascular diseases. *Chonnam. Med. J.* **2016**, *52*, 1–11. [CrossRef] [PubMed]
31. Somnay, Y.R.; Dull, B.Z.; Eide, J.; Jaskula-Sztul, R.; Chen, H. Chrysin suppresses the achaete-scute complex-like1 and alters the neuroendocrine phenotype of carcinoids. *Cancer Gene. Ther.* **2015**, *22*, 496–505. [CrossRef] [PubMed]
32. Somnay, Y.R.; Yu, X.M.; Lloyd, R.; Leverson, G.; Aburjania, Z.; Jang, S.; Jaskula-Sztul, R.; Chen, H. Notch3 Expression Correlates with Thyroid Cancer Differentiation, Induces Apoptosis, and Predicts Disease Prognosis. *Cancer* **2017**, *123*, 769–782. [CrossRef] [PubMed]

Published in final edited form as:

Adv Funct Mater. 2017 February 23; 27(8): . doi:10.1002/adfm.201604671.

Neuroendocrine Tumor-Targeted Upconversion Nanoparticle-Based Micelles for Simultaneous NIR-Controlled Combination Chemotherapy and Photodynamic Therapy, and Fluorescence Imaging

Guojun Chen,
Department of Materials Science and Engineering, University of Wisconsin–Madison, Madison, WI 53715, USA. Wisconsin Institute for Discovery, University of Wisconsin–Madison, Madison, WI 53715, USA

Prof. Renata Jaskula-Sztul,
Department of Surgery, University of Alabama at Birmingham, Birmingham, AL 35233, USA

Corinne R. Esquibel,
Laboratory for Optical and Computational Instrumentation, University of Wisconsin–Madison, Madison, WI 53706, USA

Irene Lou,
Department of Surgery, University of Wisconsin–Madison, Madison, WI 53705, USA

Qifeng Zheng,
Department of Materials Science and Engineering, University of Wisconsin–Madison, Madison, WI 53715, USA. Wisconsin Institute for Discovery, University of Wisconsin–Madison, Madison, WI 53715, USA

Ajitha Dammalapati,
Department of Surgery, University of Wisconsin–Madison, Madison, WI 53705, USA

April Harrison,
Department of Surgery, University of Wisconsin–Madison, Madison, WI 53705, USA

Prof. Kevin W. Eliceiri,
Wisconsin Institute for Discovery, University of Wisconsin–Madison, Madison, WI 53715, USA. Department of Biomedical Engineering University of Wisconsin–Madison, Madison, WI 53706, USA. Laboratory for Optical and Computational Instrumentation, University of Wisconsin–Madison, Madison, WI 53706, USA

Prof. Weiping Tang,
School of Pharmacy, University of Wisconsin–Madison, WI 53705, USA

Prof. Herbert Chen, and
Department of Surgery, University of Alabama at Birmingham, Birmingham, AL 35233, USA

Correspondence to: Herbert Chen; Shaoqin Gong.

Supporting Information

Supporting Information is available from the Wiley Online Library or from the author.

Prof. Shaoqin Gong
Department of Materials Science and Engineering, University of Wisconsin–Madison, Madison, WI 53715, USA. Wisconsin Institute for Discovery, University of Wisconsin–Madison, Madison, WI 53715, USA. Department of Biomedical Engineering University of Wisconsin–Madison Madison, WI 53706, USA

Abstract

Although neuroendocrine tumors (NETs) are slow growing, they are frequently metastatic at the time of discovery and no longer amenable to curative surgery, emphasizing the need for the development of other treatments. In this study, multifunctional upconversion nanoparticle (UCNP)-based theranostic micelles are developed for NET-targeted and near-infrared (NIR)-controlled combination chemotherapy and photodynamic therapy (PDT), and bioimaging. The theranostic micelle is formed by individual UCNP functionalized with light-sensitive amphiphilic block copolymers poly(4,5-dimethoxy-2-nitrobenzyl methacrylate)-polyethylene glycol (PNBMA-PEG) and Rose Bengal (RB) photosensitizers. A hydrophobic anticancer drug, AB3, is loaded into the micelles. The NIR-activated UCNPs emit multiple luminescence bands, including UV, 540 nm, and 650 nm. The UV peaks overlap with the absorption peak of photocleavable hydrophobic PNBMA segments, triggering a rapid drug release due to the NIR-induced hydrophobic-to-hydrophilic transition of the micelle core and thus enabling NIR-controlled chemotherapy. RB molecules are activated via luminescence resonance energy transfer to generate $^1O_2$ for NIR-induced PDT. Meanwhile, the 650 nm emission allows for efficient fluorescence imaging. KE108, a true pansomatostatin nonapeptide, as an NET-targeting ligand, drastically increases the tumoral uptake of the micelles. Intravenously injected AB3-loaded UCNP-based micelles conjugated with RB and KE108—enabling NET-targeted combination chemotherapy and PDT—induce the best antitumor efficacy.

1. Introduction

Neuroendocrine tumors (NETs), such as medullary thyroid cancers, carcinoids, islet cell tumors, and small cell lung cancers, frequently metastasize to the liver.[1] Unfortunately, patients with isolated NE liver metastases have poor survival outcomes.[1c,2] Furthermore, patients with NETs often have debilitating symptoms, such as uncontrollable diarrhea, skin rashes, flushing, and heart failure due to excessive hormone secretions,[3] thus leading to a poor quality of life. While surgical resection can be potentially curative, many patients are not candidates for operative intervention due to widespread metastases. Moreover, other forms of therapy, including chemoembolization, radioembolization, radiofrequency ablation, and cryoablation, have had limited efficacies.[3a,4] Therefore, besides surgery, there are no curative treatments for NETs and their hepatic metastases. However, even surgical resection is often followed by disease recurrence, thereby emphasizing the need for the development of other forms of therapy.

Nanotheranostics, the integration of diagnostic and therapeutic capabilities into one nanoplatform, may enable simultaneous imaging and therapy, thereby making personalized medicine possible. Nanotheranostics are of great interest for targeted cancer theranostics for the following reasons. (1) Nanoparticles (NPs) with high surface-to-volume ratios can offer

high loading capacities for multiple payloads, including anticancer agents (e.g., drugs, peptides, genes, etc.), imaging probes (e.g., dyes, radioisotopes, etc.), and tumor-targeting ligands (e.g., small molecules, peptides, antibodies, aptamers, etc.).[5] (2) NPs can effectively deliver these payloads to tumor lesions due to their passive (via the enhanced permeability and retention (EPR) effect) and active (via cell-specific ligand conjugation) tumor-targeting abilities.[6] (3) NPs can deliver multiple agents simultaneously, thus enabling combination therapies, such as chemotherapy and photodynamic therapy (PDT), which can significantly enhance their therapeutic indexes.[7]

Photodynamic therapy (PDT) is clinically approved and known as a minimally invasive medical technology for neo-plastic disease treatment.[8] PDT was the first drug–device combination approved by the U.S. Food and Drug Administration (FDA) two decades ago.[8] Typically, it involves three key components: photosensitizer, light, and tissue oxygen.[8,9] Upon excitation of the photosensitizer under lights with proper wavelengths, the photosensitizer is able to transfer the absorbed photon energy to the oxygen molecules in the surroundings, thereby generating cytotoxic singlet oxygen ($^1O_2$) to kill cancer cells. PDT can provide high specificity for the treatment of particular lesions through the control of light exposure to the photosensitizer, thereby minimizing any potential detrimental side effects on normal tissues.[9,10] However, one major limitation with current PDT is its relatively low tissue penetration depth since most photosensitizers are excited by visible or even UV light, thus limiting its applications.[11] Near-infrared (NIR) light in the range of 700–1100 nm, known as the optical tissue penetration window, can penetrate deeper into biological tissues than UV or visible light and thus is ideal for phototherapies including PDT and optical imaging.[11]

Lanthanide ion (Ln^{3+}, such as Er^{3+}, Tm^{3+}, Yb^{3+})-doped upconversion nanoparticles (UCNPs) have attracted much attention in recent years for biomedical applications due to their unique ability of converting NIR light to higher-energy photons (e.g., UV and visible light).[11b,c,12] Therefore, photosensitizers attached to lanthanide-doped UCNPs can be activated by NIR light via resonance energy transfer to effectively generate cytotoxic $^1O_2$.[13] Photosensitizers can be loaded onto the UCNPs either via physical adsorption or chemical conjugation. Physical adsorption is less desirable due to the high possibility of desorption and/or leakage of the photosensitizers from the UNCPs, resulting in low/limited efficacies.[11c,12a,b,14] Conjugating photosensitizers onto UCNPs via covalent bonds can effectively overcome this limitation and thus is more desirable for UCNP-based PDT.[12b,14b,15] In contrast to “free” photosensitizers employed by traditional PDT that are subject to fast clearance and lack tumor-targeting abilities, conjugating photosensitizers onto UCNPs can also effectively increase the accumulation of photosensitizers in the target tumor tissues/cells due to the unique tumor-targeting abilities of the nanoparticles.

It has been demonstrated recently that UCNP-based combination chemotherapy and PDT can lead to much better therapeutic outcomes than chemotherapy or PDT alone.[16] However, these previous studies either did not carry out any in vivo studies, only investigated the anticancer efficacy of intratumorally injected nanoparticles, or used a relatively high laser power density (e.g., 2.5 W cm^{-2}).[16] In this study, we developed a unique NET-targeting UCNP-based micelle capable of NIR-controlled combination

chemotherapy and PDT, as well as fluorescence imaging (Scheme 1A) and studied their in vivo tumor targeting behavior and anticancer efficacy in NET-bearing mice through intravenous injection. The laser power density used for this study was 500 mW cm^{-2}, which is well below the conservative limit of 980 nm laser intensity (726 mW cm^{-2}) for biological studies and clinical applications.[17] The following four factors were taken into consideration for the design of this multifunctional UCNP-based nanoplatform. (1) UCNPs can offer high-quality imaging due to their low background autofluorescence.[12b,18] (2) Covalent conjugation of photosensitizers onto the UCNPs can enable a more efficient NIR-activated PDT. (3) NIR-controlled fast drug release at tumor sites can potentially enhance the therapeutic efficacy of chemotherapy. (4) KE108 peptide, a true pansomatostatin synthetic nonapeptide, can potentially serve as an effective tumor targeting ligand for medullary thyroid cancers, a common type of NETs.

More specifically, the $NaYF_4$:Yb/Tm/Er UCNPs emitted light in the UV, visible, and far-red regions. The far-red emission (650 nm) of the UCNPs was employed for the UCNP-based theranostic micelle imaging in vitro and in vivo. Rose Bengal (RB) photosensitizer molecules were covalently conjugated onto the UCNP core. Since the UCNP's luminescence band around 540 nm overlapped with the absorption peak of RB, RB molecules were activated via resonance energy transfer by the NIR-activated UCNPs to effectively generate $^1O_2$ for PDT. As shown in Scheme 1B, the hydrophobic core of the UCNP-based theranostic micelle was formed by a photosensitive poly(4,5-dimethoxy-2-nitrobenzyl methacrylate) (PNBMA) polymer that can undergo a hydrophobic-to-hydrophilic transition under the UV light emitted by NIR-activated UCNPs due to photo induced polymer side-group cleavage. The NIR-triggered hydrophobic-to-hydrophilic transition of the micelle core subsequently caused a rapid release of the encapsulated hydrophobic drug (e.g., AB3, a histone deacetylase (HDAC) inhibitor whose chemical structure is shown in Figure S1, Supporting Information), thus leading to superior anticancer efficacy.[19] Finally, the UCNP-based theranostic micelles were also conjugated with KE108 peptide, an NET-targeting ligand, which can specifically and efficiently target all five subtypes of somatostatin receptors (SSTRs) overexpressed by NET cells. We have recently demonstrated that KE108 possesses superior tumor targeting abilities in carcinoid xenograft animal models over other commonly used somatostatin analogs, such as octreotide.[20] Our studies have demonstrated that NIR-controlled combination chemotherapy and PDT enabled by these unique UCNP-based theranostic micelles administered intravenously were very effective in suppressing the tumor growth of medullary thyroid cancer. We have also shown that these UCNP-based theranostic micelles can effectively serve as imaging probes specifically targeting the medullary thyroid tumors (Scheme 1C).

2. Results and Discussion

2.1. Synthesis and Characterization of UCNP-Based Theranostic Micelles

The $NaYF^4$:Yb^{3+}/Er^{3+}/Tm^{3+} UCNP core was first prepared using a thermal decomposition method in oleylamine.[12b] The hydrophilic amino-functionalized UCNPs (NH_2-UCNPs) were synthesized via a ligand-exchange approach using 2-aminoethyl dihydrogenphosphate (AEP) as a surface coating agent to replace the original oleylamine ligand. The crystal

structure of the $NaYF_4$:Yb^{3+}/Er^{3+}/Tm^{3+} UCNPs and the presence of elements including Na, F, Y, Yb, Er, and Tm in these UCNPs was characterized by X-ray diffraction (XRD) (Figure S2A, Supporting Information) and energy-dispersive X-ray (EDX) spectroscopy (Figure S2B, Supporting Information), respectively. The Fourier transform infrared (FTIR) absorption spectra shown in Figure 1A confirmed the successful coating of AEP on the surface of the UCNPs. The two new absorption bands around 1115 and 1014 cm^{-1} were attributed to the O=P stretching vibration mode and P–O–C vibration mode, respectively. Meanwhile, the long alkyl chain ($-(CH_2)-$)–, $n > 4$) vibration mode located at 736 cm^{-1} attributed to oleylamine disappeared after ligand exchange. The average size of the NH_2-UCNPs determined by transmission electron microscopy (TEM) was around 14 nm in diameter (Figure 1B). The photosensitizer RB and the alkyne functional groups (dibenzocyclooctyne acid, DBCO) were conjugated onto the UCNPs via an amidation reaction to form RB/alkyne-UCNPs. The photosensitive amphiphilic block copolymers polyethylene glycol (PEG)-PNBMA-N_3 and KE108-PEG-PNBMA-N_3 were prepared by atom transfer radical polymerization (ATRP) (detailed characterization can be found in the Supporting Information, Figure S3 and Table S1, Supporting Information) and then conjugated onto the RB/alkyne-UCNPs via catalyst-free click chemistry,[21] as shown in Figure 2.

Figure 3A (black line) shows the luminescence emissions of the NH_2-UCNP upon 980 nm excitation, including UV light (340–370 nm), 460, 540, and 650 nm. The red line in Figure 3B represents the UV–vis absorption spectrum of the resulting UCNP-RB/PNBMA-PEG nanoparticles. The strong absorption peaks at the UV region are attributed to the hydrophobic PNBMA blocks, which can form a hydrophobic micelle core wherein hydrophobic drugs can be encapsulated. As reported previously, when excited by UV light, the hydrophobic PNBMA segments can undergo a hydrophobic-to-hydrophilic transition, resulting from the cleavage of the *o*-nitrobenzyl groups on the PNBMA chain, as indicated in Scheme 1B. Hence, upon NIR activation, the UCNP would emit UV light, which would subsequently trigger a hydrophobic-to-hydrophilic transition of the micelle core formed by the PNBMA, thereby inducing a rapid drug release as described in detail later. Changes in the chemical structure of the PNBMA polymer segments after 980 nm laser illumination (10 min; 0.5 W cm^{-2}) were confirmed by ^1H NMR as shown in Figure S4 (Supporting Information). The peaks ascribed to *o*-nitrobenzyl groups were significantly decreased after 980 nm laser irradiation for 10 min. The absorbance of the RB photosensitizers also overlapped with the 540 nm luminescence emission of the UCNPs under 980 nm irradiation, thereby enabling NIR-controlled PDT via luminescence resonance energy transfer as discussed later. RB is a photosensitizer with a proven record for producing singlet oxygen with high yields.[22] In this study, ≈100 RB molecules were conjugated per UCNP in order to effectively generate singlet oxygen.[12b] Furthermore, the far-red luminescence emission at 650 nm of the NIR-activated UCNPs was conveniently used for fluorescence imaging in vitro and in vivo.

The individual UCNP functionalized with amphiphilic block copolymer PNBMA-PEG and RB (i.e., UCNP-RB/PNBMA-PEG) can form a stable micelle in an aqueous solution due to its globular structure as well as a large number of amphiphilic arms with a proper hydrophobic-to-hydrophilic ratio.[23] The morphologies of the UCNP-based theranostic

micelles were studied by dynamic light scattering (DLS) and TEM. As shown in Figure 3B, the average hydrodynamic diameter of the UCNP-based micelles was 39 nm (PDI = 0.11). The TEM image of the UCNP-based micelles (Figure 3C) showed a spherical morphology with an average diameter of around 29 nm. The size range of the UCNP-based theranostic micelles is suitable for targeted cancer theranostics.[24] AB3 was loaded into the hydrophobic core of the micelles by a dialysis method[23c] and the AB3 loading level was 16.7 wt%.

2.2. NIR-Controlled In Vitro Drug Release

Light-controlled drug release has been reported previously.[25] However, in most cases, high-energy UV or at least visible light, offering a limited tissue penetration depth, is required. NIR light is preferred since it provides a greater tissue penetration depth and is less detrimental to healthy cells.[7a] In this study, taking advantage of the UV luminescence emission of NIR (980 nm)-activated UCNPs, the photosensitive hydrophobic PNBMA segments underwent a hydrophobic-to-hydrophilic transition, thereby causing a faster release of the hydrophobic drug AB3 (an HDAC inhibitor), which was originally encapsulated into the hydrophobic PNBMA core of the micelles mainly through hydrophobic interactions. As shown in Figure 4A, without the 980 nm laser, only a small portion of the drug (<14 wt%) was released after 16 h. However, after 10 min irradiation with a 980 nm laser (0.5 W cm^{-2}), the rate of drug release increased drastically, and nearly 75 wt% drug was released after 16 h. It has been demonstrated that the faster release of chemoagents in target tumors leads to better chemotherapies,[19] which is consistent with our findings (presented in the *In Vivo Anticancer Study* section). Hence, this NIR-controlled drug release behavior makes this UCNP-based theranostic micelle a very promising drug delivery nanoplatform.

2.3. NIR-Triggered $^1O_2$ Generation

Generation of cytotoxic $^1O_2$ is critical in photodynamic cancer cell killing. The efficiency of $^1O_2$ generation by RB-conjugated UCNP-based micelles under 980 nm laser irradiation was studied using a standard protocol by monitoring the absorption intensity of 1,3-diphenylisobenzofuran (DPBF).[26] DPBF is a commonly used agent to detect $^1O_2$. It can react with singlet oxygen irreversibly and thus causes a decrease in the intensity of DPBF absorption at 417 nm. In this study, three systems were tested, namely, free RB and UCNP-based micelles with or without RB conjugation. As shown in Figure 4B, there was no DPBF consumption in those three systems without NIR irradiation, thus indicating that no $^1O_2$ was generated. Similarly, for free RB and UCNP-based micelles without RB conjugation, no sign of $^1O_2$ generation was observed under 980 nm laser irradiation. However, for the RB-conjugated UCNP-based micelles, DPBF was clearly consumed upon 980 nm laser irradiation, hence demonstrating the generation of $^1O_2$. Moreover, the amount of $^1O_2$ generated increased with the NIR irradiation time since more DPBF was depleted. Taken together, cytotoxic $^1O_2$ can be effectively generated by RB-conjugated UCNPs under NIR light irradiation, thereby enabling NIR-induced PDT.

2.4. Cellular Uptake Study Using Multiphoton Fluorescence Microscopy Based on the 650 nm Luminescence Emission of NIR-Activated UCNPs

The far-red 650 nm luminescence emission of UCNPs under 980 nm excitation was utilized for micelle detection. NET cells often overexpress SSTRs.[20,27] KE108 peptide, a somatostatin analog that can bind efficiently to all five subtypes of SSTRs, was conjugated to the digital end of the PEG blocks as an NET-targeting ligand. TT cells (human medullary thyroid cancer cell line, a type of NET cells; the SSTR expression levels are shown in Figure S5, Supporting Information) were treated with either pure medium (i.e., control), UCNP-based micelles (i.e., nontargeted), KE108-conjugated UCNP-based micelles (i.e., targeted), or KE108-conjugated UCNP-based micelles together with free KE108 peptide (i.e., the blocking assay). As shown in Figure 5A, the 650 nm emission (red color) of UCNP under 980 nm excitation was detected using a multiphoton microscope. Furthermore, a much higher red intensity was observed clearly in cells treated with targeted micelles compared to those treated with nontargeted micelles, demonstrating that the KE108 peptide can effectively enhance the cellular uptake of micelles through a receptor-mediated endocytosis process. On the contrary, in the blocking experiment, when the SSTRs on the TT cells were saturated by free KE108 peptides, the level of cellular uptake of targeted micelles was comparable to that of the nontargeted micelles. The targeting ability of KE108 peptide was further confirmed by flow cytometry analyses (Figure S6, Supporting Information) based on the fluorescence of RB. Taken together, these results confirmed the capability of UCNP-based micelles for bioimaging, as well as the excellent SSTR-targeting ability of the KE108 peptide.

2.5. In Vitro Combination Chemotherapy and PDT Using AB3-Loaded and RB-Conjugated UCNP-Based Micelles

Encouraged by the capabilities of the NIR-triggered fast drug release and the efficient generation of cytotoxic $^1O_2$ by the UCNP-based micelles, we tested the efficacy of combination chemotherapy and PDT on TT cells in vitro. The cells were divided into twelve treatment groups (abbreviations for all treatment groups were summarized in Table 1) with or without 980 nm laser illumination: free RB, AB3, AB3+RB, blank UCNP-based nontargeted micelles (NT), blank UCNP-based targeted micelles (T), RB-conjugated UCNP-based nontargeted micelles (NT-RB), RB-conjugated UCNP-based targeted micelles (T-RB), AB3-loaded UCNP-based nontargeted micelles (NT-AB3), AB3-loaded UCNP-based targeted micelles (T-AB3), AB3-loaded and RB-conjugated UCNP-based nontargeted micelles (NT-RB-AB3), and AB3-loaded and RB-conjugated UCNP-based targeted micelles (T-RB-AB3). As shown in Figure 5B, free RB and blank UCNP-based micelles did not cause any cell deaths with or without laser treatment. Without laser illumination, neither NT-RB nor T-RB showed any PDT effect and no $^1O_2$ was produced. However, under 980 nm laser illumination (0.5 W cm^{-2} for 10 min), about 18% and 26% cell death was observed for cells treated with NT-RB and T-RB for 48 h, respectively, thus demonstrating the effectiveness of PDT. The increased cytotoxicity of T-RB over NT-RB was attributed to the enhanced cellular uptake of the targeted micelles via receptor-mediated endocytosis, as discussed earlier. The viability of cells treated with pure AB3 with or without laser treatment was 56% and 54%, respectively, suggesting that 980 nm laser irradiation for 10 min did not notably affect the cell viability of pure AB3. Treatment with AB3-loaded UCNP-based

micelles (without any RB conjugation), without 980 nm laser irradiation, resulted in a 20% (NT-AB3) and 42% (T-AB3) cancer cell death, whereas under 980 nm laser irradiation, the percentage of cell death increased to 32% (NT-AB3) and 53% (T-AB3), respectively. The higher cytotoxicity observed in the laser groups was ascribed to the NIR-triggered fast AB3 drug release.[19] Meanwhile, the increased cytotoxicity in targeted groups over nontargeted groups was attributed to the enhanced cellular uptake of micelles through SSTR-mediated endocytosis. More importantly, 86% cell death was observed for cells treated with T-RB-AB3 (last bar) under 980 nm laser irradiation due to a combination of chemotherapy and PDT, which provided a dramatically better therapeutic index than chemotherapy alone (T-AB3, 53% cell death) or PDT alone (T-RB, 31% cell death). Similarly, the T-RB-AB3-Laser treatment (86% cell death) induced higher cytotoxicity over the NT-RB-AB3-Laser (59% cell death) because the KE108 targeting ligand significantly enhanced the cellular uptake of the micelles.

2.6. Tumor Accumulation of UCNP-Based Micelles

As aforementioned, UCNPs emitting the far-red 650 nm luminescence under 980 nm light excitation served as an excellent imaging probe in vivo.[28] Herein, the in vivo tumor accumulation of the UCNP-based micelles was investigated in TT-tumor-bearing mice. The mice were intravenously injected with saline (control), nontargeted micelles (i.e., UNCP-based micelles without KE108 conjugation), and targeted micelles (i.e., KE108-conjugated UCNP-based micelles). Five hours postinjection, the mice were analyzed using a multiphoton microscope (Ex/Em: 980/650 nm). As shown in Figure 6, no far-red signal was detected in the control group. However, red luminescence (650 nm) was clearly visible in both the nontargeted group and targeted group upon 980 nm excitation. Moreover, a much stronger micelle signal was observed in the mice treated with targeted micelles, demonstrating the excellent in vivo targeting ability of the KE108 peptide. In contrast to nontargeted micelles that only exhibit passive tumor-targeting ability via the enhanced permeation and retention (EPR) effect, KE108-conjugated (i.e., targeted) micelles possessed both passive and active NET targeting abilities, thereby leading to a significantly higher micelle tumor accumulation. Ex vivo imaging of the excised tumors (Figure S7, Supporting Information; based on the RB fluorescence) further confirmed the greater tumor uptake of the targeted micelles compared to the nontargeted ones.

The NET targeting and in vivo imaging capabilities of the UCNP-based theranostic micelles were also studied in a TT-liver-metastases mouse model. The intrasplenic injections of human TT cells were described in detail in the Experimental Section. Six weeks post-intrasplenic injection, mice were intravenously injected with targeted micelles. We have shown that the KE108-conjugated UCNP-based micelles targeted the liver metastases nodules very effectively, and emissions at 650 nm from the NIR-activated UCNP-based micelles were detected mostly within the tumor metastases (Figure S8, Supporting Information). This study has demonstrated that nanoparticle with KE108 as the active targeting ligand can effectively target NET-liver-metastases, which warrants further studies in the future.

2.7. In Vivo Anticancer Efficacy of the Combination Chemotherapy and PDT

To assess the therapeutic efficacy of UCNP-based micelles, a subcutaneous TT-tumor xenograft mouse model was used. When mice developed palpable tumors, they were intravenously injected with one of the following ten agents: saline (control), pure AB3, RB-conjugated targeted micelles with or without laser (i.e., T-RB-Laser or T-RB), AB3-loaded targeted micelles with or without laser (i.e., T-AB3-Laser or T-AB3), AB3-loaded nontargeted micelles with or without laser (i.e., NT-RB-AB3-Laser or NT-RB-AB3), and AB3-loaded targeted micelles with or without laser (i.e., T-RB-AB3-Laser or T-RB-AB3) at Day 0 and Day 7, at an equivalent AB3 dosage of 30 mg kg^{-1} BW, which is below the maximum tolerated dose (MTD, 50 mg kg^{-1} BW). All laser treatments were conducted by applying a continuous wave fiber-coupled 980 nm laser (0.5 W cm^{-2}, 15 min, 1 min interval after each 5 min of irradiation) at tumor sites 4 h postinjection. Changes in relative tumor volume are shown in Figure 7A. T-AB3 (final tumor volume: 778.8 ± 57.9 mm^3) exhibited a better anticancer efficacy than pure AB3 (final tumor volume: 1160.2 ± 89.2 mm^3; $p < 0.01$), thus demonstrating the benefit of using targeted drug nanocarriers. Moreover, T-AB3-Laser (final tumor volume: 625.8 ± 40.7 mm^3; NIR-controlled chemotherapy) showed a better outcome than T-AB3 without laser (final tumor volume: 778.8 ± 57.9 mm^3; $p < 0.05$), resulting from the faster drug release triggered by the NIR light.[19] Meanwhile, T-RB (final tumor volume: 1463.2 ± 140.6 mm^3) did not exhibit any therapeutic effect without the 980 nm illumination, as compared to the control group (final tumor volume: 1557.2 ± 163.6 mm^3). In contrast to this experiment, tumor exposure to NIR light (T-RB-Laser) resulted in a significant anticancer effect (final tumor volume: 872.6 ± 63.0 mm^3; NIR-controlled PDT; $p < 0.01$) due to NIR-activated PDT. Furthermore, T-RB-AB3-Laser (final tumor volume: 171.3 ± 13.7 mm^3), which enabled combination chemotherapy and PDT, produced a much better anticancer efficacy than either chemotherapy alone (T-AB3-Laser; final tumor volume: 625.8 ± 40.7 mm^3; $p < 0.001$) or PDT alone (T-RB-Laser; final tumor volume: 872.6 ± 63.0 mm^3; $p < 0.001$). Moreover, the T-RB-AB3-Laser showed much better anticancer efficacy than the NT-RB-AB3-Laser (final tumor volume: 594.0 ± 45.8 mm^3; $p < 0.001$), demonstrating the advantages of NET-targeted drug delivery using KE108 as the targeting ligand. Key findings from the in vivo anticancer studies are summarized in Figure 7B. Taken together, AB3-loaded NIR-activated UCNP-based micelles conjugated with RB and KE108 (i.e., T-RB-AB3-Laser), which enabled NET-targeted combination chemotherapy and PDT, induced the best antitumor efficacy and did not cause any significant changes in body weight (Figure 7C) or survival. In addition, pathological assessment of hematoxylin and eosin (H&E)-stained sections of different organs (liver, brain, heart, and leg muscles) of mice treated with T-RB-AB3-Laser did not show any signs of acute or chronic inflammation, or apoptotic or necrotic regions (Figure 7D), thus suggesting that the UCNP-based theranostic micelles are safe for organs other than cancerous tissues.

3. Conclusions

An NET-targeted UCNP-based theranostic micelle was developed for simultaneous combination chemotherapy and PDT, as well as bioimaging, under NIR light illumination. The UCNP-based micelles exhibited excellent imaging capabilities both in vitro and in vivo.

The KE108 targeting ligand was capable of significantly enhancing the cellular and tumoral uptake of the micelles. Moreover, the NIR light effectively triggered fast drug release at the tumor sites, thereby achieving superior chemotherapy efficacy, and effectively generated cytotoxic $^1O_2$ for PDT. In vivo studies demonstrated that AB3-loaded UCNP-based micelles conjugated with both RB and KE108, capable of targeted combination chemotherapy and PDT, induced a dramatically better antitumor efficacy compared to chemotherapy or PDT alone, without any apparent systemic toxicity. Thus, this unique UCNP-based theranostic micelle could be a promising nanoplatform for targeted NET theranostics.

4. Experimental Section

Materials—CF_3CO_2Na, $Y(CF_3CO_2)_3$, $Yb(CF_3CO_2)_3$, $Tm(CF_3CO_2)_3$, and $Er(CF_3CO_2)_3$ were purchased from Rare Earth Products, Inc. (Beverly, MA, USA). AEP, RB, and DBCO were obtained from Sigma-Aldrich (St. Louis, MO, USA). Methoxy-PEG-OH (OCH_3-PEG-OH, M_n = 5 kDa) and OH-PEG-*N*-hydroxysuccinimide (HO-PEG-NHS, M_n = 5 kDa) were purchased from JenKem Technology (Allen, TX, USA). KE108 was purchased from Bachem Americas, Inc. (Torrance, CA, USA). All other agents were purchased from Fisher Scientific (Fitchburg, WI, USA) and used as received unless otherwise stated.

Synthesis of Amino-Functionalized $NaYF_4$:Yb^{3+}/Er^{3+}/Tm^{3+} UCNPs (NH_2-UCNPs)—The $NaYF_4$:Yb^{3+}/Er^{3+}/Tm^{3+} UCNP core was prepared using a thermal decomposition method.[12b] First, a three-neck round-bottom flask containing a magnetic stir bar was charged with CF_3CO_2Na (2 mmol), $Y(CF_3CO_2)_3$ (0.78 mmol), $Yb(CF_3CO_2)_3$ (0.2 mmol), $Tm(CF_3CO_2)_3$ (0.02 mmol), $Er(CF_3CO_2)_3$ (0.002 mmol), and oleylamine (12 mL). The solution was magnetically stirred and heated slowly to 120 °C under vacuum for 1 h to form the lanthanide oleate complexes, and to remove any residual acetic acid, water, and oxygen. The temperature was then increased to 320 °C as quickly as possible and this temperature was maintained for 1 h under an argon atmosphere. The mixture was then allowed to cool down to 80 °C. The UCNPs were precipitated by the addition of ethanol and isolated via centrifugation at 2000 rpm. The resulting pellets were dispersed in chloroform and precipitated with excess anhydrous ethanol. The UCNPs were isolated via centrifugation at 2000 rpm and then dispersed in chloroform for subsequent experiments.

In order to obtain NH_2-UCNPs, a ligand exchange method was adopted to transform the hydrophobic $NaYF_4$:Yb^{3+}/Er^{3+}/Tm^{3+} UCNPs into hydrophilic ones. Briefly, AEP (200 mg) was dissolved in a mixture of deionized (DI) water and ethanol (3:2, v/v, 10 mL). The UCNPs (20 mg) in chloroform (5 mL) were then added dropwise to the AEP solution and stirred vigorously using a magnetic stirring bar over 48 h at room temperature. After ligand exchange, the NH_2-UCNPs were collected via centrifugation at 2000 rpm and redispersed in 5 mL of water.

Synthesis of Rose Bengal Hexanoic Acid (RB-Acid)—The photosensitizer, RB, was reacted with 6-bromohexanoic acid in acetone/water (7:3, v/v) at 75 °C for 24 h. Thereafter, acetone was removed under vacuum. After three repetitions of liquid–liquid extraction in water and ethyl acetate, the RB-acid aqueous solution was collected and dried under lyophilization.

Synthesis of RB and Alkyne-Functionalized UCNPs—2 mg of NH_2-UCNPs, DBCO (3.14 mg), and RB-acid (6.3 mg) were dissolved in dimethyl sulfoxide (DMSO) and stirred vigorously over 48 h at room temperature. The impurities were then removed by dialysis against DI water for 48 h using a cellulose membrane (molecular weight cut-off, 8 kDa). The RB/alkyne-UNPCs were obtained after lyophilization. The alkyne-UCNPs (without RB conjugation) were prepared following a similar method.

Synthesis of 4,5-Dimethoxy-2-nitrobenzyl methacrylate (NBMA)—4,5-Dimethoxyl-2-nitrobenzyl alcohol (596 mg) and triethylamine (TEA, 1.97 mg) were dissolved in dichloromethane (10 mL). Methacryloyl chloride (0.4 mL, purified by distillation under vacuum before use) in 4 mL dichloromethane was added slowly to the above solution over 30 min through an addition funnel. After 3 h of reaction in an ice bath, the whole system was kept at room temperature overnight. After the removal of the solvent by a rotary evaporator, the crude product was dissolved in chloroform and purified by washing with HCl (1 M) and KCl (1 M) in sequence. Anhydrous $MgSO_4$ was used as a drying agent to absorb residual water. After filtration using a Büchner funnel, the solution was concentrated into a solid using a rotary evaporator and dried under vacuum overnight.

Synthesis of PEG-Br Macroinitiator—OCH_3-PEG-OH (50 mg) and TEA (2.25 mg) were dissolved in dry dichloromethane (10 mL) and stirred in an ice bath. 2-Bromoisobutyryl bromide (2.76 mg) in dichloromethane (5 mL) was added dropwise into this solution over 1 h. Next, the solution was stirred at room temperature overnight and then precipitated in cold ethyl ether. The crude product was purified by dissolving it in hot 2-propanol (70 °C) and precipitating it in cold 2-propanol. The polymer was then dried under vacuum. KE108-PEG-Br macroinitiator was synthesized following a similar method using KE108-PEG-OH instead. KE108-PEG-OH was synthesized by reacting KE108-NH_2 with NHS-PEG-OH at room temperature for 24 h.

Synthesis of PEG-PNBMA by ATRP—OCH_3-PEG-Br (0.009 mmol), NBMA (0.9 mmol), Cu(I)Br (0.018 mmol), and *N*,*N*,*N*′,*N*″,*N*″-pentamethyldiethylenetriamine (0.036 mmol) were dissolved in 1 mL DMSO. The mixture was degassed three times using a freeze–pump–thaw procedure, sealed under vacuum, and stirred in an oil bath (90 °C) for 13 h. The solution was then precipitated into methanol. The crude product was collected by filtration using a Büchner funnel and was purified by dissolving it in tetrahydrofuran (THF, 2 mL) and passing it through a neutral Al_2O_3 column with THF as an eluent solvent to remove any excess catalyst. The yellow filtrate was concentrated under a reduced pressure and reprecipitated twice into cold diethyl ether. The polymer was collected by centrifugation and dried under vacuum overnight. KE108-PEG-PNBMA was prepared following a similar method using KE108-PEG-Br as the macroinitiator.

Synthesis of PEG-PNBMA-N_3—PNBMA-PEG (20 mg) and NaN_3 (0.32 mg) were dissolved in DMSO (1.2 mL) and stirred for 48 h at 80 °C. The impurities were removed by dialysis against DI water for 48 h using a cellulose membrane (molecular weight cut-off, 8 kDa). The polymer was then dried under lyophilization.

Synthesis of UCNP-RB/PNBMA-PEG-OCH_3 (Abbreviated as UCNP-RB/PNBMA-PEG, Used to Prepare Nontargeted UCNP-Based Theranostic Micelles)— OCH_3-PEG-PNBMA-N_3 (10 mg) and UCNP-RB/alkyne (1 mg) were dissolved in DMSO (2 mL) and stirred for 48 h at room temperature. The impurities were removed by dialysis against DI water using a cellulose membrane (molecular weight cut-off, 15 kDa) for 48 h. The polymer was obtained under lyophilization. The UCNP-PNBMA-PEG-OCH_3 was prepared following a similar method using alkyne-UCNPs instead.

Synthesis of UCNP-RB/PNBMA-PEG-OCH_3/KE108 (Abbreviated as UCNP-RB/PNBMA-PEG-KE108, Used to Prepare Targeted UCNP-Based Theranostic Micelles)— OCH_3-PEG-PNBMA-N_3 (8.5 mg), KE108-PEG-PNBMA-N_3 (1.5 mg), and UCNP-RB/alkyne (1 mg) were dissolved in 2 mL DMSO and stirred for 48 h at room temperature. The impurities were removed by dialysis against DI water using a cellulose membrane (molecular weight cut-off, 15 kDa) for 48 h. The polymer was obtained under lyophilization. The UCNP-PNBMA-PEG-OCH_3/KE108 was prepared following a similar method using alkyne-UCNPs instead.

Synthesis of AB3-Loaded UCNP-RB/PNBMA-PEG-KE108 Theranostic Micelles (AB3-Loaded Theranostic Micelles)— To prepare AB3-loaded targeted theranostic micelles, AB3 (1.5 mg) and UCNP-RB/PNBMA-PEG-OCH_3/KE108 (5 mg) (i.e., T-RB-AB3) or UCNP-PNBMA-PEG-OCH_3/KE108 (5 mg) (i.e., T-AB3) were dissolved in 1 mL of dimethylformamide (DMF). DI water (3 mL) was added dropwise into the above solution. After another 2 h of stirring, the solution was dialyzed against DI water for 48 h. The final product was obtained by lyophilization. The AB3-loaded nontargeted theranostic micelles were prepared following a similar method using UCNP-RB/PNBMA-PEG-OCH_3 (i.e., NT-RB-AB3) or UCNP-PNBMA-PEG-OCH_3 (i.e., NT-AB3) instead.

Characterization— ^{1}H NMR spectra were recorded on a Varian Mercury Plus 300 spectrometer using DMSO-d_6, D_2O, or $CDCl_3$ as a solvent at 25 °C. FTIR spectra were recorded on a Bruker Tensor 27 FT-IR spectrometer. Molecular weights (M_n and M_w) and polydispersity indices (PDI; M_n/M_w) of the polymers were determined by gel permeation chromatography (GPC) equipped with triple detectors (i.e., a refractive index detector, a light scattering detector, and a viscometer detector) (Viscotek, USA) using DMF with 0.1 mmol of LiBr as a mobile phase. The luminescence spectrum of the UCNPs was acquired on a Nanolog FL3-2iHR spectrofluorometer (HORIBA Jobin Yvon, Inc., USA). The elemental analyses of the UCNPs were carried out using a scanning electron microscope (SEM, LEO GEMINI 1530, Zeiss, USA) equipped with EDX spectroscopy. The XRD pattern of the UCNPs was collected on a D8 Discover diffractometer (Bruker, USA). The morphologies of the UCNPs or UCNP-based micelles were determined by TEM (FEI Tecnai G2 F30 TWIN 300 kV, E.A. Fischione Instruments, Inc., USA) and DLS (ZetaSizer Nano ZS90, Malvern Instrument, USA). The AB3 and RB loading level (weight percentage) were measured by a Cary 500 UV-vis–NIR spectrophotometer based on a standard calibration curve for AB3 and RB at 297 and 560 nm, respectively.

NIR-Triggered PNBMA Hydrophobic-to-Hydrophilic Transition—^{1}H NMR analyses were performed to study the NIR-triggered hydrophobic-to-hydrophilic transition behavior of the PNBMA hydrophobic segments. In order to study the changes in the chemical structure of the PNBMA segments in the UCNP-PNBMA-PEG nanoparticles induced by NIR irradiation, 5 mg of UCNP-PNBMA-PEG was dispersed in 10 mL DI water and the resulting micelle solution then irradiated with a 980 nm laser (0.5 W cm^{-2}) for 10 min. The NIR-irradiated UCNP-PNBMA-PEG in the aqueous solution was collected by freeze-drying. To purify the NIR-irradiated UCNP-PNBMA-PEG, the resulting freeze-dried powder was first dissolved in DMSO and then precipitated in cold diethyl ether, which was subsequently dried under vacuum. ^{1}H NMR spectra of the UCNP-PNBMA-PEG polymer before and after 10 min 980 nm laser illumination (0.5 W cm^{-2}) were collected in DMSO-d_6.

NIR-Light Triggered $^1O_2$ Generation—DPBF is a commonly used agent to detect $^1O_2$.[26] As is typical, 20 μL of a DPBF/ethanol solution (10 mmol L^{-1}) was added to 2 mL of a solution containing either free RB or UCNP-based micelles with or without RB conjugation. The solution was kept in the dark and irradiated with a 980 nm laser (0.5 W cm^{-2}) for 16 min, and the absorption intensity of DPBF at 417 nm was recorded every 2 min. As the negative control groups, DPBF absorption in those three systems was also measured without 980 nm laser irradiation.

NIR-Light Triggered In Vitro Drug Release Profile—Drug release studies were performed in PBS solution at 37 °C. A 5 mL solution of AB3-loaded UCNP-based micelles was placed in a dialysis membrane (molecular weight cut-off 8 kDa), which was placed in 10 mL of release media. After 1 h incubation, the samples were irradiated with the 980 nm laser at an output power of 0.5 W cm^{-2} over a period of 10 min. At certain time points, 3 mL of media were collected and replaced by an equal amount of fresh media. The drug release behavior was monitored for 16 h. The amount of AB3 released was quantified by a UV–vis spectrophotometer at 297 nm. For the control group, the sample was kept in the dark without 980 nm irradiation throughout the experiment and the release media were collected at the same time points.

Cellular Uptake Study—The 650 nm luminescence band of the NIR (980 nm)-activated UCNPs was conveniently used for fluorescence imaging to study the effect of the KE108 peptide on the cellular uptake of the micelles in vitro using a multiphoton microscope with excitation and emission wavelengths of 980 and 650 nm, respectively. TT cells (human medullary thyroid cancer cell line; 1.4 × 10^4 cells cm^{-2}) were seeded in the eight-slide chamber and incubated overnight. Cells were then treated with KE108-conjugated UCNP-based micelles (i.e., targeted micelles) and nontargeted UCNP-based micelles (i.e., without KE108 conjugation) at a micelle concentration of 166 μg mL^{-1}. The blocking experiment with the coincubation of free KE108 (2 × 10^{-6} M) and targeted micelles was also performed. Cells treated with pure media were used as the control. After 2 h incubation, cells were washed with DPBS and fixed by 4% PFA. Thereafter, DAPI (2 μg mL^{-1}) was used to stain the cell nuclei. The sample was then subjected to multiphoton imaging with a Zeiss 20×/1.0 NA objective (see below).

Multiphoton Imaging—All multiphoton microscopy in this study was performed on an upright Ultima IV microscope (Bruker Nano Surfaces, Middleton, WI). An Insight DeepSee ultrafast Ti:Sapphire laser (Spectra Physics, Palo Alto, CA), tuned to 980 nm and directed through a Pockel's cell (ConOptics, Danbury, CT), was used for sample excitation. Fluorescence emission was split using a 445 nm dichroic and subsequently filtered through either a 620/60 BP filter (Chroma) for UCNP-based micelle emission (650 nm) or a 445/40 BP filter (Chroma) for DAPI emission. Fluorescence was then detected via multialkali photomultiplier tubes (Hamamatsu, Hamamatsu, Japan). Data were acquired using PrairieView software (Bruker Nano Surfaces, Middleton, WI).

In Vitro Cytotoxicity Evaluation—The in vitro cytotoxicity of UCNP-based micelles against TT cells was analyzed by MTT assay. Cells (8×10^4 cells cm^{-2}) were seeded into a 96-well plate and incubated overnight. The media were replaced with fresh media, or fresh media containing free AB3, free RB, a combination of free AB3 and RB, blank UCNP-based micelles (both targeted and nontargeted), AB3-loaded UCNP-based micelles (both targeted and nontargeted), RB-conjugated UCNP-based micelles (both targeted and nontargeted), or AB3-loaded and RB-conjugated UCNP-based micelles (both targeted and nontargeted) at an equivalent AB3 concentration of 2×10^{-6} M. After 3 h incubation, cells were irradiated by the 980 nm laser at a power density of 0.5 W cm^{-2} for 10 min. The cells were then incubated at 37 °C for another 45 h before applying the MTT reagent. The same panels were carried out for 48 h without laser treatment. Thereafter, a standard MTT protocol was carried out and cell viabilities (percentage of the pure media group without 980 nm laser illumination) were calculated.

In Vivo Tumoral Uptake of the Micelles—The 650 nm luminescence band of the NIR (980 nm)-activated UCNPs was utilized for in vivo fluorescence imaging. Male athymic nude mice (four week old) were purchased from Charles River (Wilmington, Maryland, USA).

A subcutaneous TT-tumor xenograft mouse model was established by the subcutaneous injection of 200 μL of Hanks balanced salt solution (Mediatech, Inc., Manassas, VA, USA) containing 1×10^7 of TT cells into the left flank. 10 d after inoculation, tumors of 5–6 mm in diameter were observed and TT-tumor-bearing mice were randomly divided into three groups (5 mice/group). The mice were intravenously injected with 200 μL of either saline (control), nontargeted micelles, or targeted micelles at a micelle concentration of 18.7 mg mL^{-1}. 5 h postinjection, the mice were scanned using a multiphoton microscope and an Olympus 4×/0.1 NA objective (see above). Excitation and emission wavelengths were 980 nm and 650 nm, respectively.

The tumor targeting ability of the micelles was also assessed in a NET liver metastases xenograft mouse model. In order to create NET liver metastases, each animal was anesthetized and placed on its right side. A small incision was then made in the left flank. The spleen was located and was further exposed and isolated with the aid of a tip applicator. About 5×10^6 TT cells (200 μL) were injected into the distal part of the spleen using a 25 G needle. 2 min postinjection, namely, after the TT cells entered into circulation, the splenic vessels were tied off and the spleen removed in order to decrease the ultimate tumor burden.

The skin and fascia were reapproximated with a vicryl suture. The mouse was then recovered from anesthesia, and the tumors were allowed to propagate. After confirmation of tumor progression by microCT scans (six weeks after cell injection), mice with liver metastases were treated with targeted UCNP-based micelles (18.7 mg mL^{-1}) via intravenous injection. The livers with tumor metastases were collected 7 h postinjection and images were taken using a fluorescence microscope with 980 nm excitation. Emission from the theranostic micelles at 650 nm was then detected in the liver.

In Vivo Anticancer Study—The same subcutaneous TT-tumor xenograft mouse model was used for the in vivo anticancer study. Mice were intravenously treated with ten groups (six mice per group) including: (1) saline (control); (2) free AB3; (3) AB3-loaded targeted micelles (T-AB3); (4) AB3-loaded targeted micelles with 980 nm laser illumination (T-AB3-Laser); (5) RB-conjugated targeted micelles (T-RB); (6) RB-conjugated targeted micelles with 980 nm laser illumination (T-RB-Laser); (7) AB3-loaded RB-conjugated nontargeted micelles (NT-RB-AB3); (8) AB3-loaded RB-conjugated nontargeted micelles with 980 nm laser illumination (NT-RB-AB3-Laser); (9) AB3-loaded RB-conjugated targeted micelles (T-RB-AB3); and (10) AB3-loaded RB-conjugated targeted micelles with 980 nm laser illumination (T-RB-AB3-Laser). The dosage of AB3 was 30 mg kg^{-1} BW. The dosage of AB3-loaded UCNP-based micelles (AB3 loading level was 16.7 wt%) in groups (7), (8), (9), and (10) was 180 mg kg^{-1} BW, corresponding to 30 mg kg^{-1} BW of AB3. The dosage of RB-conjugated UCNP-based micelles (without AB3 encapsulation) in groups (5) and (6) was 150 mg kg^{-1} BW. Each treatment group received two intravenous injections 7 d apart. For all treatment groups involving 980 nm laser treatment, a continuous wave fiber-coupled 980 nm laser (0.5 W cm^{-2}, 15 min, 1 min interval after every 5 min of irradiation) was applied at the tumor sites 4 h postinjection. Tumor volumes were measured with a caliper and then calculated using the formula: tumor volume = (length × $width^2$)/2. The weights of the mice were monitored during the experiment. At the end of the experiment, mice were sacrificed and a pathological examination of the lungs, heart, liver, and spleen was performed to confirm that there was no evidence of metastases or tumor growth outside of the inoculation sites. All major organs of the mice treated with T-AB3-RB-Laser, including the liver, brain, heart, and leg muscles, were collected, and H&E-stained sections were prepared for pathological assessment. All experimental procedures were carried out in compliance with our animal care protocol, which was approved by the Animal Care and Use Committee at the University of Wisconsin–Madison.

Supplementary Material

Refer to Web version on PubMed Central for supplementary material.

Acknowledgments

G.C. and R.J.-S. contributed equally to this work. This project was financially supported by grants from the NIH (K25CA166178 and R21CA196653 to S. Gong, and R01 CA121115 to H. Chen), the Aly Wolff Memorial Foundation (S. Gong and H. Chen), the American Cancer Society (MEN2 Thyroid Cancer Professorship 120319-RPM-11-080-01–TBG to H. Chen and Research Scholar Award RSGM TBE-121413 to H. Chen). The authors would also like to express their appreciation to Prof. Weibo Cai at the University of Wisconsin–Madison for providing the NIR-laser instrument for our studies, and Dr. Feng Chen for the helpful discussion related to the synthesis and characterization of UCNPs.

References

1. a) Adler JT, Meyer-Rochow GY, Chen H, Benn DE, Robinson BG, Sippel RS, Sidhu SB. Oncologist. 2008; 13:779. [PubMed: 18617683] b) Pinchot SN, Pitt SC, Sippel RS, Kunnimalaiyaan M, Chen H. Curr Opin Invest Drugs. 2008; 9:576.c) Chen H, Hardacre JM, Uzar A, Cameron JL, Choti MA. J Am Coll Surg. 1998; 187:88. [PubMed: 9660030] d) Chen H, Pruitt A, Nicol TL, Gorgulu S, Choti MA. J Gastrointest Surg. 1998; 2:151. [PubMed: 9834411] e) Chen H. J Surg Oncol. 2008; 97:203. [PubMed: 18264978]
2. Norton JA. Best Pract Res, Clin Gastroenterol. 2005; 19:577. [PubMed: 16183528]
3. a) Brown KT, Koh BY, Brody LA, Getrajdman GI, Susman J, Fong Y, Blumgart LH. J Vasc Interv Radiol. 1999; 10:397. [PubMed: 10229465] b) Miller CA, Ellison EC. Surg Oncol Clin North Am. 1998; 7:863.
4. a) Isozaki T, Kiba T, Numata K, Saito S, Shimamura T, Kitamura T, Morita K, Tanaka K, Sekihara H. Int Med. 1999; 38:17.b) Eriksson B, Kloppel G, Krenning E, Ahlman H, Plockinger U, Wiedenmann B, Arnold R, Auernhammer C, Korner M, Rindi G, Wildi S. Neuroendocrinology. 2008; 87:8. [PubMed: 18097129] c) Lal A, Chen H. Curr Opin Oncol. 2006; 18:9. [PubMed: 16357558] d) Lehnert T. Transplantation. 1998; 66:1307. [PubMed: 9846513] e) Zhang R, Straus FH, DeGroot LJ. Endocrinology. 1999; 140:2152. [PubMed: 10218966] f) Boudreaux JP, Putty B, Frey DJ, Woltering E, Anthony L, Daly I, Ramcharan T, Lopera J, Castaneda W. Ann Surg. 2005; 241:839. [PubMed: 15912033] g) Nguyen C, Faraggi M, Giraudet AL, de Labriolle-Vaylet C, Aparicio T, Rouzet F, Mignon M, Askienazy S, Sobhani I. J Nucl Med. 2004; 45:1660. [PubMed: 15471830] h) Fiorentini G, Rossi S, Bonechi F, Vaira M, De Simone M, Dentico P, Bernardeschi P, Cantore M, Guadagni S. J Chemother. 2004; 16:293. [PubMed: 15330328] i) Zuetenhorst JM, Olmos RAV, Muller M, Hoefnagel CA, Taal BG. Endocr-Relat Cancer. 2004; 11:553. [PubMed: 15369454]
5. a) Xu W, Siddiqui IA, Nihal M, Pilla S, Rosenthal K, Mukhtar H, Gong S. Biomaterials. 2013; 34:5244. [PubMed: 23582862] b) Yang X, Grailer JJ, Pilla S, Steeber DA, Gong S. Bioconjugate Chem. 2010; 21:496.c) Guo J, Hong H, Chen G, Shi S, Nayak TR, Theuer CP, Barnhart TE, Cai W, Gong S. ACS Appl Mater Interfaces. 2014; 6:21769. [PubMed: 24628452] d) Peer D, Karp JM, Hong S, Farokhzad OC, Margalit R, Langer R. Nat Nanotechnol. 2007; 2:751. [PubMed: 18654426] e) Win KY, Feng SS. Biomaterials. 2005; 26:2713. [PubMed: 15585275] f) Shi X, Chen G, Guo LW, Si Y, Zhu M, Pilla S, Liu B, Gong S, Kent KC. PloS One. 2014; 9:e89227. [PubMed: 24586612]
6. a) Greish K. Methods Mol Biol. 2010; 624:25. [PubMed: 20217587] b) Reuveni T, Motiei M, Romman Z, Popovtzer A, Popovtzer R. Int J Nanomed. 2011; 6:e64.c) Ma J, Huang P, He M, Pan L, Zhou Z, Feng L, Gao G, Cui D. J Phys Chem B. 2012; 116:14062. [PubMed: 23134318] d) Bartlett DW, Su H, Hildebrandt IJ, Weber WA, Davis ME. Proc Natl Acad Sci USA. 2007; 104:15549. [PubMed: 17875985] e) Xiao Y, Hong H, Javadi A, Engle JW, Xu W, Yang Y, Zhang Y, Barnhart TE, Cai W, Gong S. Biomaterials. 2012; 33:3071. [PubMed: 22281424]
7. a) Fan W, Shen B, Bu W, Chen F, He Q, Zhao K, Zhang S, Zhou L, Peng W, Xiao Q, Ni D, Liu J, Shi J. Biomaterials. 2014; 35:8992. [PubMed: 25103233] b) Wang T, Zhang L, Su Z, Wang C, Liao Y, Fu Q. ACS Appl Mater Interfaces. 2011; 3:2479. [PubMed: 21604817] c) Kimura M, Miyajima K, Kojika M, Kono T, Kato H. Int J Mol Sci. 2015; 16:25466. [PubMed: 26512656] d) Colasanti A, Kisslinger A, Quarto M, Riccio P. Acta Biochim Pol. 2005; 51:1039.e) Ma M, Chen H, Chen Y, Wang X, Chen F, Cui X, Shi J. Biomaterials. 2012; 33:989. [PubMed: 22027594] f) Shiah JG, Sun Y, Kopečková P, Peterson C, Straight R, Kopeček J. J Controlled Release. 2001; 74:249.g) Khdair A, Chen D, Patil Y, Ma L, Dou QP, Shekhar MP, Panyam J. J Controlled Release. 2010; 141:137.
8. Agostinis P, Berg K, Cengel KA, Foster TH, Girotti AW, Gollnick SO, Hahn SM, Hamblin MR, Juzeniene A, Kessel D, Korbelik M, Moan J, Mroz P, Nowis D, Piette J, Wilson BC, Golab J. CA Cancer J Clin. 2011; 61:250. [PubMed: 21617154]
9. a) Dolmans D, Fukumura D, Jain R. Nat Rev Cancer. 2003; 3:380. [PubMed: 12724736] b) Castano AP, Mroz P, Hamblin MR. Nat Rev Cancer. 2006; 6:535. [PubMed: 16794636]
10. Juarranz Á, Jaén P, Sanz-Rodríguez F, Cuevas J, González S. Clin Transl Oncol. 2008; 10:148. [PubMed: 18321817]

11. a) Weissleder R, Ntziachristos V. Nat Med. 2003; 9:123. [PubMed: 12514725] b) Idris NM, Gnanasammandhan MK, Zhang J, Ho PC, Mahendran R, Zhang Y. Nat Med. 2012; 18:1580. [PubMed: 22983397] c) Cui S, Yin D, Chen Y, Di Y, Chen H, Ma Y, Achilefu S, Gu Y. ACS Nano. 2012; 7:676. [PubMed: 23252747]
12. a) Wang C, Tao H, Cheng L, Liu Z. Biomaterials. 2011; 32:6145. [PubMed: 21616529] b) Liu K, Liu X, Zeng Q, Zhang Y, Tu L, Liu T, Kong X, Wang Y, Cao F, Lambrechts S, Aalder M, Zhang H. ACS Nano. 2012; 6:4054. [PubMed: 22463487] c) Zhou L, Li Z, Liu Z, Yin M, Ren J, Qu X. Nanoscale. 2014; 6:1445. [PubMed: 24316678] d) Chen Z, Liu Z, Li Z, Ju E, Gao N, Zhou L, Ren J, Qu X. Biomaterials. 2015; 39:15. [PubMed: 25477167] e) Liu Z, Li Z, Liu J, Gu S, Yuan Q, Ren J, Qu X. Biomaterials. 2012; 33:6748. [PubMed: 22770569]
13. a) Idris NM, Gnanasammandhan MK, Zhang J, Ho PC, Mahendran R, Zhang Y. Nat Med. 2012; 18:1580. [PubMed: 22983397] b) Cheng L, Wang C, Liu Z. Nanoscale. 2013; 5:23. [PubMed: 23135546] c) Tian G, Zhang X, Gu Z, Zhao Y. Adv Mater. 2015; 27:7692. [PubMed: 26505885] d) Wang C, Cheng L, Liu Z. Theranostics. 2013; 3:317. [PubMed: 23650479] e) Wang Y, Liu K, Liu X, Dohnalová KI, Gregorkiewicz T, Kong X, Aalders MC, Buma WJ, Zhang H. J Phys Chem Lett. 2011; 2:2083.f) Ai F, Ju Q, Zhang X, Chen X, Wang F, Zhu G. Sci Rep. 2015; 5:10785. [PubMed: 26035527]
14. a) Shan J, Budijono SJ, Hu G, Yao N, Kang Y, Ju Y, Prud'homme RK. Adv Funct Mater. 2011; 21:2488.b) Huang P, Lin J, Wang S, Zhou Z, Li Z, Wang Z, Zhang C, Yue X, Niu G, Yang M. Biomaterials. 2013; 34:4643. [PubMed: 23523428]
15. Xia L, Kong X, Liu X, Tu L, Zhang Y, Chang Y, Liu K, Shen D, Zhao H, Zhang H. Biomaterials. 2014; 35:4146. [PubMed: 24529625]
16. a) Yin M, Ju E, Chen Z, Li Z, Ren J, Qu X. Chem - Eur J. 2014; 20:14012. [PubMed: 25200923] b) Zhang T, Lin H, Cui L, An N, Tong R, Chen Y, Yang C, Li X, Qu F. RSC Adv. 2016; 6:26479.c) Ai F, Sun T, Xu Z, Wang Z, Kong W, To MW, Wang F, Zhu G. Dalton Trans. 2016; 45:13052. [PubMed: 27430044] d) Yuan Y, Min Y, Hu Q, Xing B, Liu B. Nanoscale. 2014; 6:11259. [PubMed: 25130329] e) Yuan Y, Liu B. ACS Appl Mater Interfaces. 2014; 6:14903. [PubMed: 25075548] f) Yang S, Li N, Liu Z, Sha W, Chen D, Xu Q, Lu J. Nanoscale. 2014; 6:14903. [PubMed: 25362857] g) Fan W, Shen B, Bu W, Chen F, He Q, Zhao K, Zhang S, Zhou L, Peng W, Xiao Q. Biomaterials. 2014; 35:8992. [PubMed: 25103233] h) Yue C, Zhang C, Alfranca G, Yang Y, Jiang X, Yang Y, Pan F, de la Fuente JM, Cui D. Theranostics. 2016; 6:456. [PubMed: 26941840]
17. a) Chen Z, Zhang L, Sun Y, Hu J, Wang D. Adv Funct Mater. 2009; 19:3815.b) Wang Z, Li W, Yu N, Liu Z, Zhang L, Chen Z. RSC Adv. 2016; 6:42763.
18. Cui S, Yin D, Chen Y, Di Y, Chen HM, Achilefu YS, Gu Y. ACS Nano. 2013; 7:676. [PubMed: 23252747]
19. a) Cheng R, Meng F, Deng C, Klok HA, Zhong Z. Biomaterials. 2013; 34:3647. [PubMed: 23415642] b) Chytil P, Etrych T, Konak C, Sirova M, Mrkvan T, Boucek J, Rihova B, Ulbrich K. J Controlled Release. 2008; 127:121.c) Dai J, Lin S, Cheng D, Zou S, Shuai X. Angew Chem, Int Ed Engl. 2011; 50:9404. [PubMed: 21898731]
20. Chen G, Jaskula-Sztul R, Harrison A, Dammalapati A, Xu W, Cheng Y, Chen H, Gong S. Biomaterials. 2016; 97:22. [PubMed: 27156249]
21. Ning X, Guo J, Wolfert MA, Boons GJ. Angew Chem, Int Ed Engl. 2008; 47:2253. [PubMed: 18275058]
22. Redmond RW, Gamlin JN. Photochem Photobiol. 1999; 70:391. [PubMed: 10546544]
23. a) Guo J, Hong H, Chen G, Shi S, Zheng Q, Zhang Y, Theuer CP, Barnhart TE, Cai W, Gong S. Biomaterials. 2013; 34:8323. [PubMed: 23932288] b) Chen G, Wang L, Cordie T, Vokoun C, Eliceiri KW, Gong S. Biomaterials. 2015; 47:41. [PubMed: 25682159] c) Brinkman AM, Chen G, Wang Y, Hedman CJ, Sherer NM, Havighurst TC, Gong S, Xu W. Biomaterials. 2016; 101:20. [PubMed: 27267625]
24. a) Blanco E, Shen H, Ferrari M. Nat Biotechnol. 2015; 33:941. [PubMed: 26348965] b) Cabral H, Matsumoto Y, Mizuno K, Chen Q, Murakami M, Kimura M, Terada Y, Kano M, Miyazono K, Uesaka M. Nat Nanotechnol. 2011; 6:815. [PubMed: 22020122]

25. a) Jiang J, Tong X, Morris D, Zhao Y. Macromolecules. 2006; 39:4633.b) Wang Y, Han P, Xu H, Wang Z, Zhang X, Kabanov AV. Langmuir. 2009; 26:709.c) He J, Tong X, Zhao Y. Macromolecules. 2009; 42:4845.

26. Chen F, Zhang S, Bu W, Chen Y, Xiao Q, Liu J, Xing H, Zhou L, Peng W, Shi J. Chemistry. 2012; 18:7082. [PubMed: 22544381]

27. a) Jaskula-Sztul R, Xu W, Chen G, Harrison A, Dammalapati A, Nair R, Cheng Y, Gong S, Chen H. Biomaterials. 2016; 91:1. [PubMed: 26994874] b) Gabriel M, Decristoforo C, Kendler D, Dobrozemsky G, Heute D, Uprimny C, Kovacs P, von Guggenberg E, Bale R, Virgolini IJ. J Nucl Med. 2007; 48:508. [PubMed: 17401086]

28. a) Wang F, Banerjee D, Liu Y, Chen X, Liu X. Analyst. 2010; 135:1839. [PubMed: 20485777] b) Xiong L, Yang T, Yang Y, Xu C, Li F. Biomaterials. 2010; 31:7078. [PubMed: 20619791]

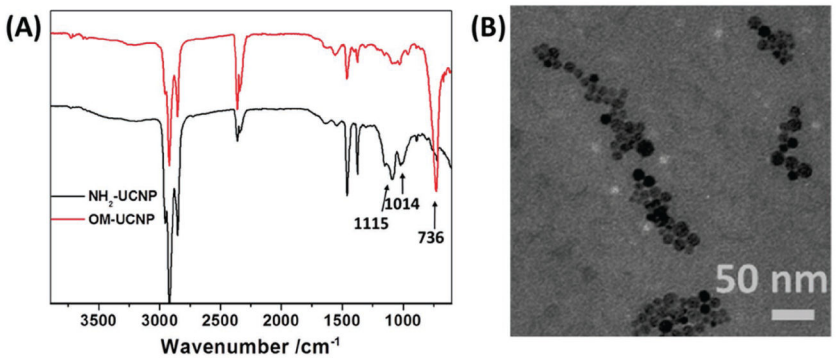

Figure 1.

A) FTIR absorption spectra of the oleylamine-stabilized UCNPs (OM-UCNP) (red curve) and NH_2-UCNPs (black curve). B) TEM image of the NH_2-UCNPs.

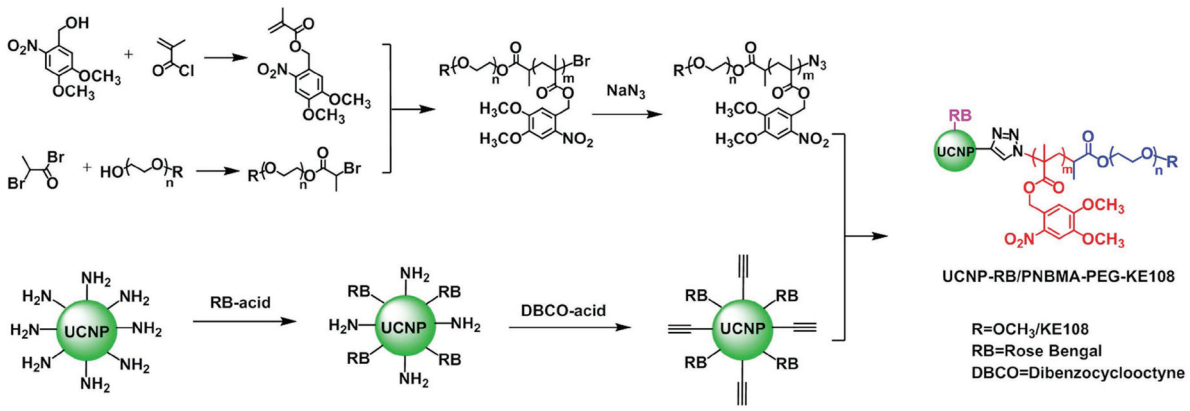

Figure 2.

Synthesis scheme of the multifunctional UCNP-based theranostic micelles (UCNP-RB/PNBMA-PEG-KE108).

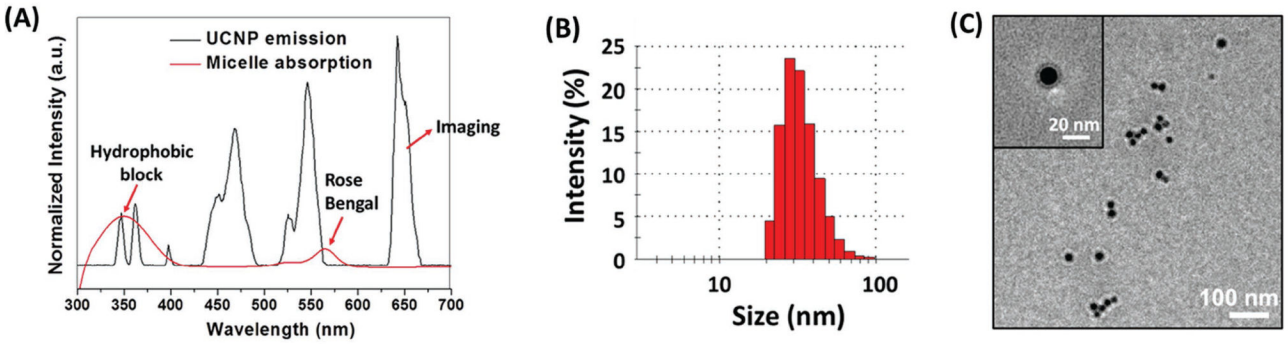

Figure 3.

A) Spectral overlap between the upconversion emission spectrum of the UCNPs (black curve) and the UV–vis absorption spectrum of the UCNP-based theranostic micelles (red curve). B) Dynamic light scattering (DLS) analyses and C) transmission electron microscopy (TEM) image of the UCNP-based theranostic micelles.

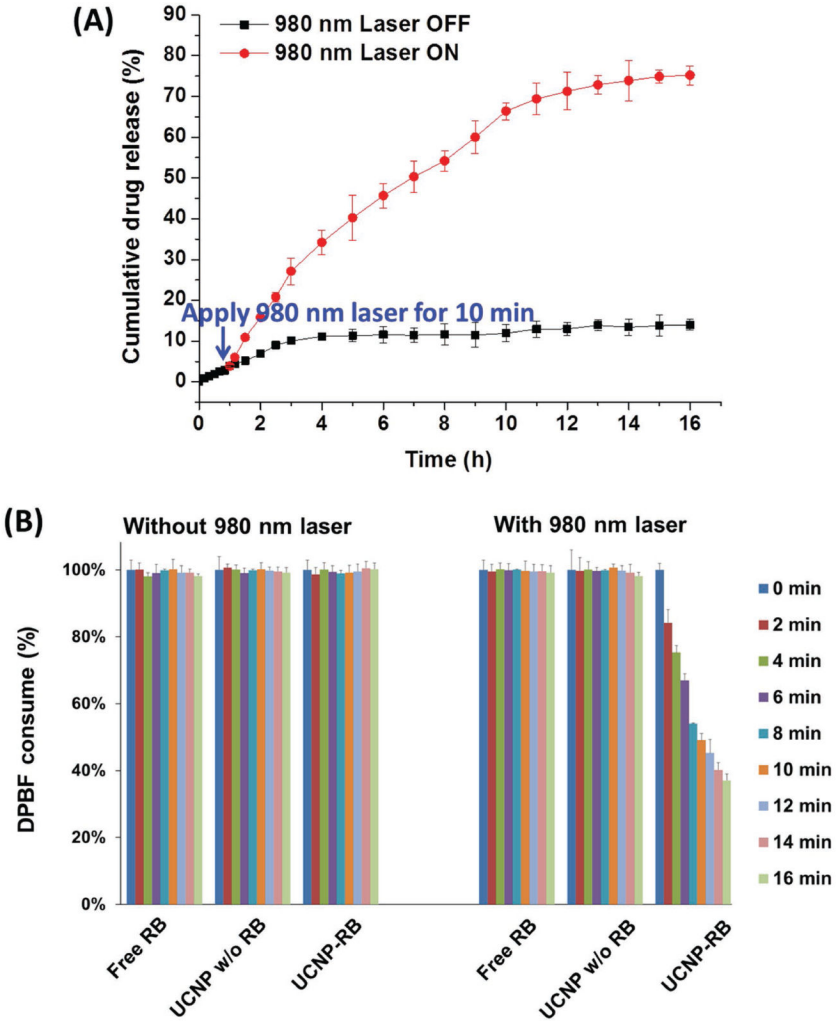

Figure 4.

NIR-triggered A) in vitro drug release profile and B) singlet oxygen ($^1O_2$) generation.

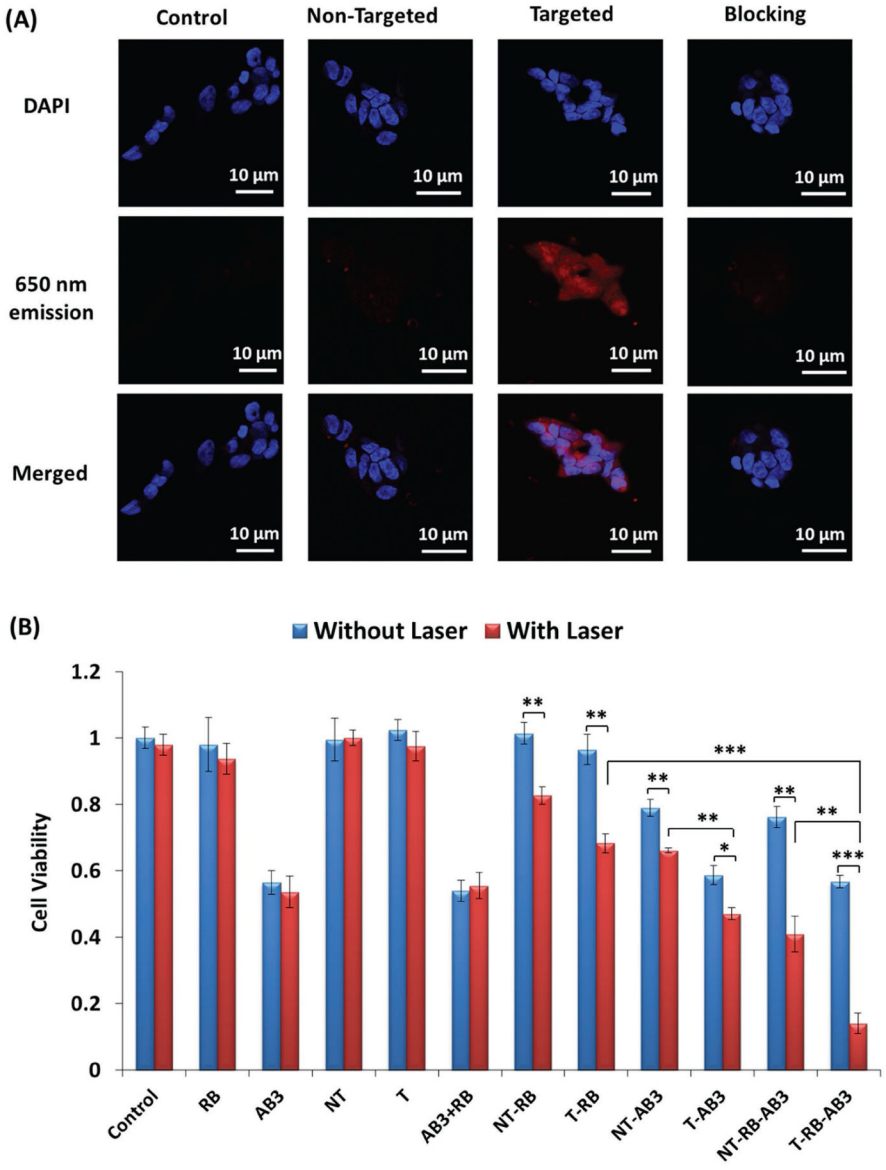

Figure 5.

A) In vitro cellular uptake study of the UCNP-based theranostic micelles in NET (TT) cells. Cells were treated with pure medium (i.e., control), nontargeted (i.e., lacking KE108) micelles, and targeted (i.e., KE108-conjugated) micelles (166 μg mL^{-1}), as well as the combination of free KE108 peptide (2×10^{-6} M) and targeted micelles (i.e., blocking) for 2 h at 37 °C. Images were taken under a multiphoton microscope based on the 650 nm luminescence emission of the NIR-activated UCNPs (Ex/Em: 980/650 nm). B) In vitro evaluation of cell viabilities. Abbreviation for all treatment groups was summarized in Table 1. For all laser-related treatments, the cells were first incubated with micelles for 3 h, followed by irradiation by the 980 nm laser at a power density of 0.5 W cm^{-2} for 10 min. The cells were then incubated at 37 °C for another 45 h. *: $p < 0.05$; **: $p < 0.01$; ***: $p < 0.001$.

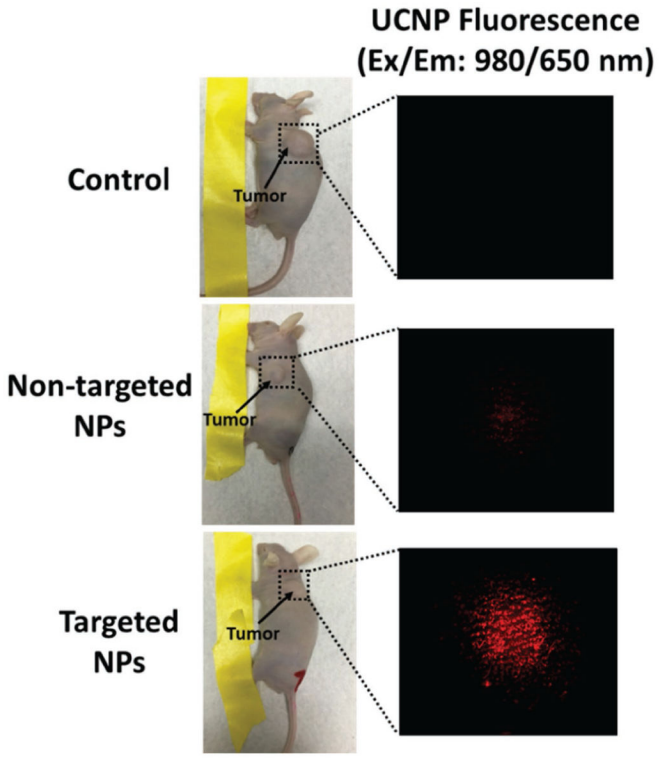

Figure 6.

Tumor accumulation of the UCNP-based theranostic micelles in TT-tumor-bearing mice. The mice were intravenously treated with saline (control), nontargeted micelles (i.e., UNCP-based micelles without KE108 conjugation), and targeted micelles (i.e., KE108-conjugated UCNP-based micelles). The mice were analyzed using a multiphoton microscope (Ex/Em: 980/650 nm) 5 h postinjection.

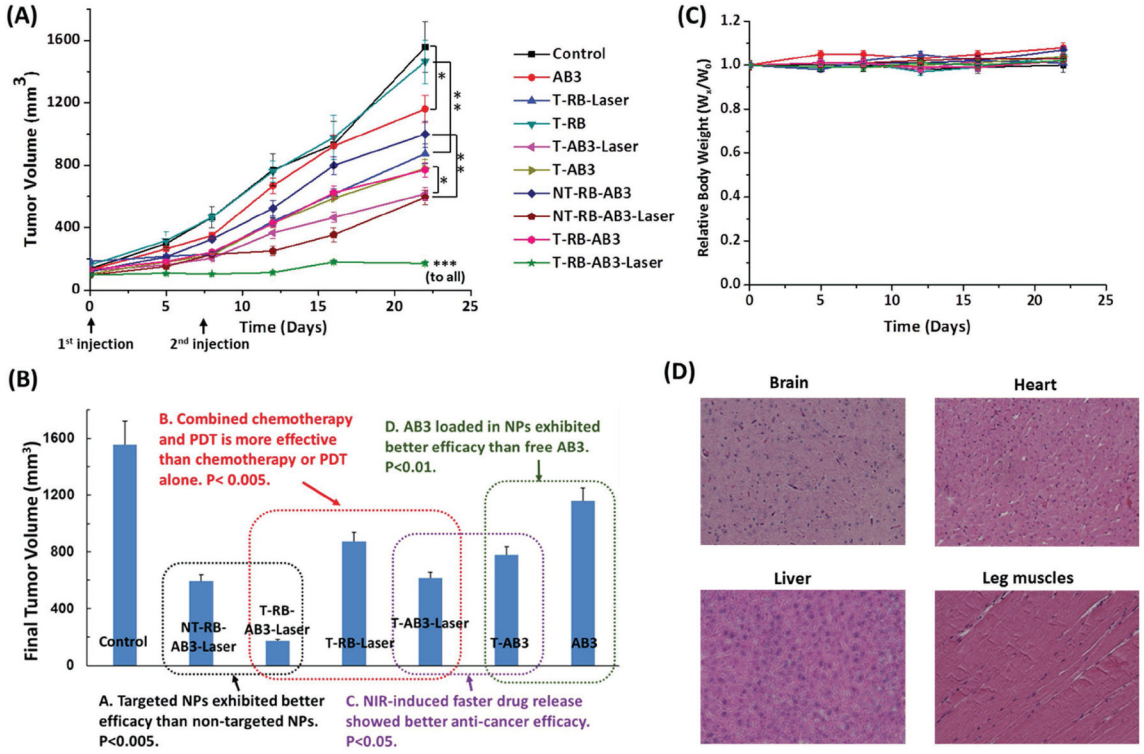

Figure 7.

A) In vivo anticancer efficacy of different formulations of UCNP-based theranostic micelles in NET xenografts. Tumor-bearing mice were treated with ten groups: (1) Saline (control); (2) AB3 (conventional chemotherapy); (3) T-RB (no PDT effect as no laser illumination); (4) T-RB-Laser (targeted NIR-controlled PDT); (5) T-AB3 (targeted chemotherapy); (6) T-AB3-Laser (targeted NIR-controlled chemotherapy); (7) NT-AB3-RB (nontargeted chemotherapy; no PDT effect as no laser illumination); (8) NT-AB3-RB-Laser (nontargeted combination NIR-controlled chemotherapy and PDT); (9) T-AB3-RB (targeted chemotherapy; no PDT effect as no laser illumination); and (10) T-AB3-RB-Laser (targeted combination NIR-controlled chemotherapy and PDT). Each mouse received two intravenous injections (30 mg kg^{-1} BW of AB3) over a 7 d interval. A continuous wave fiber-coupled 980 nm laser (0.5 W cm^{-2}, 15 min, 1 min interval after every 5 min of irradiation) was applied at the tumor sites in the “Laser” groups 4 h postinjection. B) The final tumor volumes and key findings for the anticancer study. C) Change in body weight of animals as a function of time. W_x: body weight at selected time point; W_0: initial body weight. D) Representative H&E-stained sections of the brain, heart, liver, and leg muscles of the mouse treated with T-RB-AB3-Laser micelles. No signs of apoptotic or necrotic areas were observed. All values are presented as a mean SD ($n = 6$). *: $p < 0.05$; **: $p < 0.01$; ***: $p < 0.001$.

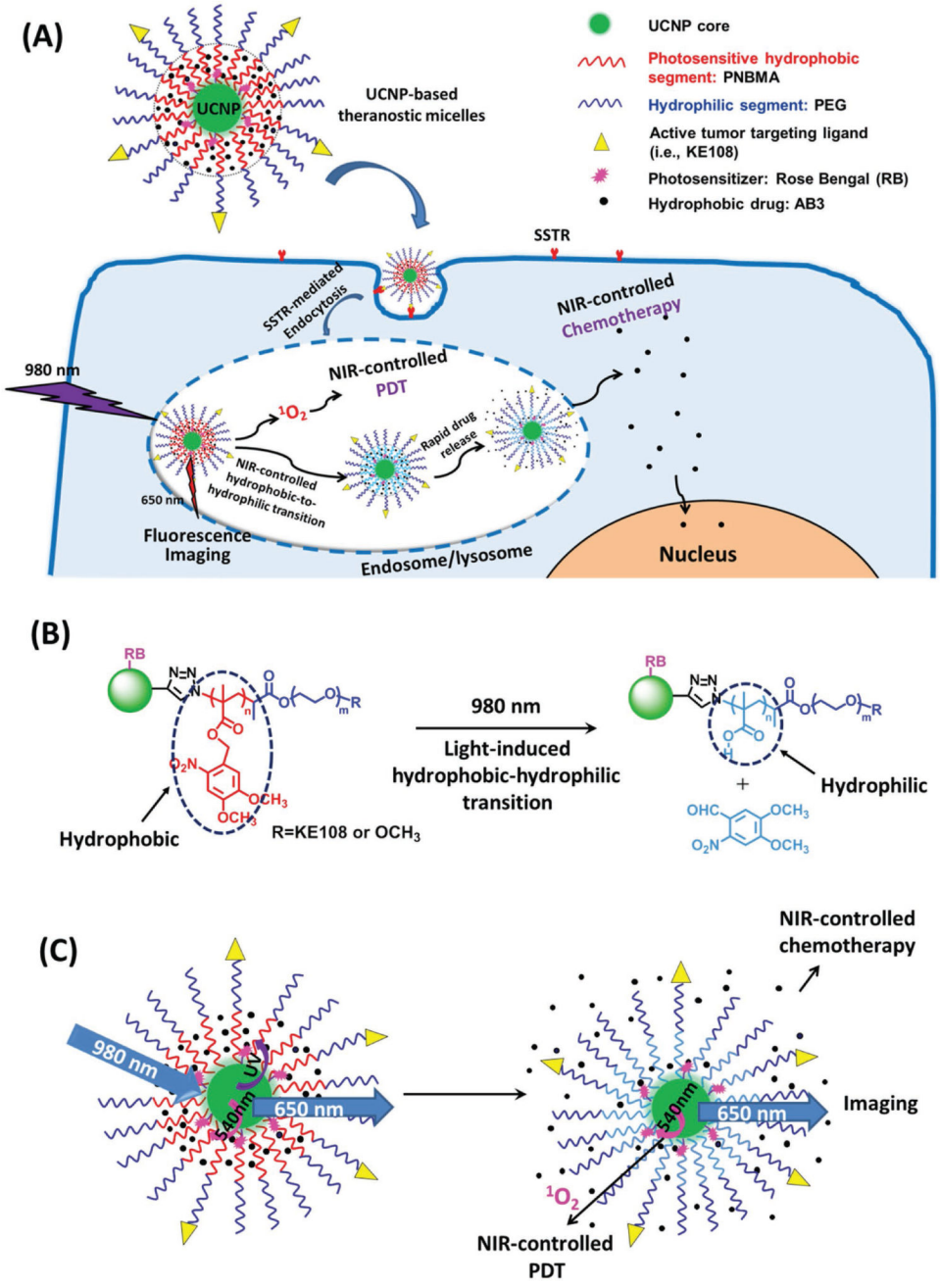

Scheme 1.

A) NET-targeted UCNP-based theranostic micelles for simultaneous NIR-controlled combination chemotherapy and PDT, as well as fluorescence imaging. B) An illustration of the NIR-triggered hydrophobic-to-hydrophilic transition. C) An illustration of NIR-controlled combination chemotherapy and PDT, as well as fluorescence imaging.

Table 1

Abbreviations for all treatment formulations.

Control	PBS (in vitro) or saline (in vivo)
AB3	Free AB3 (an HDAC inhibitor) without any carrier
RB	Free Rose Bengal (photosensitizer) without any carrier
NT	Blank UCNP-based nontargeted micelles
T	Blank UCNP-based targeted micelles
AB3 + RB	The combination of free AB3 and RB
NT-RB	RB-conjugated UCNP-based nontargeted micelles
NT-AB3	AB3-loaded UCNP-based nontargeted micelles
NT-RB-AB3	AB3-loaded and RB-conjugated UCNP-based nontargeted micelles
T-RB	RB-conjugated UCNP-based targeted (i.e., KE108-conjugated) micelles
T-AB3	RB-conjugated UCNP-based targeted NPs
T-RB-AB3	AB3-loaded and RB-conjugated UCNP-based targeted micelles